NAZARBAYEV UNIVERSITY

Organic solar cells for space application

A thesis presented
by
Akhtanova Gulnur

Supervisor: Prof.Viktor Brus

The School of Sciences and Humanities
in partial fulfillment of the requirements
for the degree of
Doctor of Philosophy in Physics
Nazarbayev University
Astana, Kazakhstan
2025

Acknowledgements

Every single person who has helped me on my journey to get my PhD degree deserves my utmost gratitude. This adventure would not have been possible without their support, help, and guidance. I want to thank them all from the bottom of my heart.

Dedicated to my beloved KÖKE

Peer-Reviewed Publicatons

1) ***Gulnur Akhtanova***, Yerassyl Yerlanuly, Hryhorii P. Parkhomenko, Mykhailo V. Solovan, Andrii I. Mostovyi, Aliya K. Nurmukhanbetova, Alexander V. Kireyev, Igor V. Danko, Pavel A. Oreshkin, Timur K. Zholdybayev, Daniyar M. Janseitov, Tlekkabul S. Ramazanov, and Viktor V. Brus,ACS Omega 2024 9 (1), 925-933.
https://pubs.acs.org/doi/full/10.1021/acsomega.3c07053
2) ***Gulnur Akhtanova***, Hryhorii P. Parkhomenko, Joachim Vollbrecht, Andrii I. Mostovyi, Nora Schopp, Viktor Brus,Surface recombination in organic solar cells: Intrinsic vs. doped active layer,Organic Electronics,Volume 137,2025,107183,ISSN 1566-1199,
https://www.sciencedirect.com/science/article/pii/S1566119924001940
3) ***Gulnur Akhtanova***, Hryhorii P. Parkhomenko, Nurzhan Asanov, Andrii I. Mostovyi, Marat Kaikanov, Nora Schopp Viktor V. Brus. Organic Solar Cells for Space Applications: The Crucial Role of Active Layer Thickness. *Submitted*
4) N. Schopp, ***G. Akhtanova***, P. Panoy, A. Arbuz, S. Chae, A. Yi, H. J. Kim, V. Promarak, T.-Q. Nguyen, V. V. Brus, Unraveling Device Physics of Dilute-Donor Narrow-Bandgap Organic Solar Cells with Highly Transparent Active Layers. *Adv. Mater.* 2022, 34, 2203796
https://advanced.onlinelibrary.wiley.com/doi/full/10.1002/adma.202203796
5) H. P. Parkhomenko, A. I. Mostovyi, ***G. Akhtanova***, M. M. Solovan, M. Kaikanov, N. Schopp, V. V. Brus, Self-Healing of Proton-Irradiated Organic Photodiodes and Photovoltaics. *Adv. Energy Mater.* 2023, 13, 2301696.
https://onlinelibrary.wiley.com/doi/full/10.1002/aenm.202301696
6) M. M. Solovan, A. I. Mostovyi, D. Aidarkhanov, H. P. Parkhomenko, ***G. Akhtanova***, N. Schopp, E. A. Asare, D. Nauruzbayev, M. Kaikanov, A. Ng, V. V. Brus, Extreme Radiation Resistance of Self-Powered High-Performance $Cs_{0.04}Rb_{0.04}(FA_{0.65}MA_{0.35})_{0.92}Pb(I_{0.85}Br_{0.14}Cl_{0.01})_3$ Perovskite Photodiodes. *Adv. Optical Mater.* 2023, 11, 2203001
https://onlinelibrary.wiley.com/doi/full/10.1002/adom.202203001
7) Y.Yerlanuly, H.Parkhomenko, R.Zhumadilov, R.Nemkayeva, ***G.Akhtanova***, M.Solovan, A.Mostovyi, S. Orazbayev, A.Utegenov, T. Ramazanov, M.Gabdullin, A. umabekov, V.Brus,Achieving stable photodiode characteristics under ionizing radiation with a self-adaptive nanostructured heterojunction CNWs/CdZnTe,Carbon,Volume 215, 2023,118488,ISSN 0008-6223,
https://www.sciencedirect.com/science/article/pii/S0008622323007339
8) Y.Yerlanuly, R.Zhumadilov, I. Danko, D. Janseitov, R.Nemkayeva, A.Kireyev, A.Arystan, ***Gulnur Akhtanova***, J.Vollbrecht, N.Schopp, A.Nurmukhanbetova, T. Ramazanov, A.Jumabekov, P.Oreshkin, T.Zholdybayev, M. Gabdullin, and V. Brus,*ACS Omega* **2022** *7* (51), 48467-48475
https://pubs.acs.org/doi/full/10.1021/acsomega.2c06735

Scholarship

1) **Yessenov Launch Pad 2024** scholarship

Award

1) **Helmholtz-Zentrum Berlin** :International Quantsol Summer School on Photovoltaics and New Concepts of Quantum Solar Energy Conversion 2024, **Award in Optical Simulation**

ABSTRACT

by Gulnur Akhtanova

Even though organic solar cells' lightweight, flexible, and low cost fabrication are important factors for space applications, their remarkable 20% performance opens the door for them to compete with perovskite and silicon solar cells as potential satellite power source. Considering the harsh environment in space, the next reasonable question is how well organic solar cells will function therein. At this time, no comprehensive study of organic solar cells has been conducted to identify potential areas of device physics and material features that could be compromised when exposed to irradiation. This dissertation comprises three investigations that integrate approaches to elucidate a comprehensive analysis of the device physics of state-of-the-art organic semiconductor devices in harsh space environments. To be specific, this thesis offers an in-depth analysis of the fundamental device physics mechanisms in organic solar cells (OSCs) across different structural configurations under irradiation. It focuses on: i) the impact of photoactive layer thickness on charge generation, extraction, and recombination processes under proton irradiation; ii) the recovery mechanism in post-annealed devices; iii) the radiation resistance of different architectures of OSCs; iv) the extent of degradation in the functional layers of OSCs when exposed to proton irradiation; and v) the impact of the substrate on TiN thin film's properties under electron irradiation. The first study focuses on understanding the device physics characteristics of organic solar cell with PM6:Y6 photoactive layer at different thicknesses are exposed to low energy proton irradiation estimated as equivalent to around 3 years of operation in Low Earth Orbit with further thermal annealing. Even though irradiated thick devices degrade more rapidly than irradiated thin devices, devices with a thickness of 60 and 100 nm preserve 15% and 10% of efficiency, respectively. In addition, the recovery process of the irradiated OSC was studied by employing thermal annealing at varying times. Particularly, following 5 hours of thermal annealing, the irradiated device with an active layer thickness of 100 nm recovered 25% and achieved a PCE of 5.13%. Device physics characteristics of OSCs, such as generation, recombination and extraction are investigated to study the impact of irradiation to each of physical mechanism occurring in OSC. As a result, the generation rate in OSC and the morphology of PM6:Y6 thin films are unaffected by proton irradiation. It was found that the drop in PCE of the irradiated devices is mainly caused by the short-circuit current density (J_{SC}) values decreasing as a result of increased bulk and surface trap densities, as well as ineffective charge extraction. The

thickness of the photoactive layer had a strong correlation with the short-circuit current and charge extraction in both conditions : irradiated and post-annealed devices.In particular, the irradiated OSC with a thin photoactive layer shows higher resilience to proton irradiation and better recovery of thermal annealing compared to thick devices. The next chapter expands upon previous work on organic solar cells (OSCs) in extreme environments, with a focus on the radiation resistance of different OSC structure. Specifically, it is dedicated to investigate the impact of the transport layer on the photovoltaic performance of organic solar cells under proton irradiation. For that purpose, both the conventional and inverted structures used the photoactive PM6:Y6 layer with different transport layers and identical electrodes. Compared to conventional structures with organic transport layers, inverted structures with inorganic transport layers exhibit superior radiation resistance in terms of photovoltaic performance. To gain a thorough understanding of the irradiated OSC's performance, the recombination study identified the trap-assisted recombination as the dominant mechanism in both structures based on the V_{OC} value on the light intensity (V_{OC} vs ln[I]). The photovoltaic performance and recombination analysis showed that the metal-oxide transport layers, ZnO and MoOx, were more resistant to radiation than the organic thin films, PEDOT:PSS and PDINN. The structural and optical characteristics of the transport layers and electrodes enabled the determination of how proton irradiation affects the operation of various OSC structures. Yet, the thin films of ZnO, Ag, and MoOx exhibited the alteration in crystallinity when exposed to proton radiation. Many different kinds of optoelectronic devices are utilized in the field of space technology. It is critical that these devices function well under aggressive ionizing conditions. Titanium nitride (TiN) thin films may enhance the characteristics of optoelectronic devices. Thanks to its broad band gap, excellent thermal, chemical, electrical, optical, and mechanical qualities, and structural integrity, titanium nitride (TiN) has found widespread application in electrical and mechanical engineering. This means that studying how different substrates (such as quartz and sapphire) influence the characteristics of TiN thin films is an influential factor. For that purpose, high energy electron exposure was used to irradiate TiN thin films on different substrates. The structural analysis identified that TiN deposited on sapphire undergone atomic displacements in the material’s lattice revealed in diffraction patterns. However this served as improvements of the electrical features of TiN on both substrates. Chemical composition analysis showed the retaination in metallic features of Ti-N bound in TiN deposited on quartz along with surface roughness.

TABLE OF CONTENT

List of Figures

List of Tables

List of Abbreviations

SC	solar cell
OSC	organic solar cell
PSC	perovskite solar cell
BOL	beginning of life
EOL	end of life
C-OSC	conventional organic solar cell
I-OSC	inverted organic solar cell
MJSC	multi-junction solar cells
BHJ	bulk heterojunction
EQE	external quantum efficiency
ETL	electron transport layer
HTL	hole transport layer
PCE	power conversion efficiency
FF	fill factor
LEO	Low Earth Orbi

Chapter 1 Introduction

1.1 Background and Motivation

Satellite technology is now an integral part of everyday life, impacting everything from weather forecasting and communication (such as internet, phone, and TV) to navigation and scientific research [5–7]. As of June 19, 2024, there are 10,019 operational satellites in space, with the majority, 9254, deployed in LEO at distances ranging from 400 to 1200 km above the Earth [8]. Since 1958, photovoltaic solar panels have been widely used to power satellites and other space technology by converting sunlight into electricity [1]. In the vacuum of space, where there is no atmosphere, solar panels provide an efficient and reliable source of energy, making them the ideal power solution for satellites and spacecraft.

With single crystal Si-based solar cells, Vanguard 1 became the first solar-powered satellite to launch into space, achieving a total power of about 1 Watt with an efficiency of 10% [9]. In fact, the satellite powered by solar cells opens a new path for research of cosmos. For example, the Apollo 11 in 1969 , marked the beginning of a new advanced system of space technology enabling different mission such as research of our solar system, weather forecasting, navigations, communication and broadcasting. The International Space Station is the biggest orbiting laboratory working on the variety research from astrophysics to microbiology in LEO and has been serving for 25 years on orbit. The solar arrays of the International Space Station consist of 262,400 solar cells and span about 2,500 square meters, with the four array sets capable of generating between 84 and 120 kilowatts of power [1].

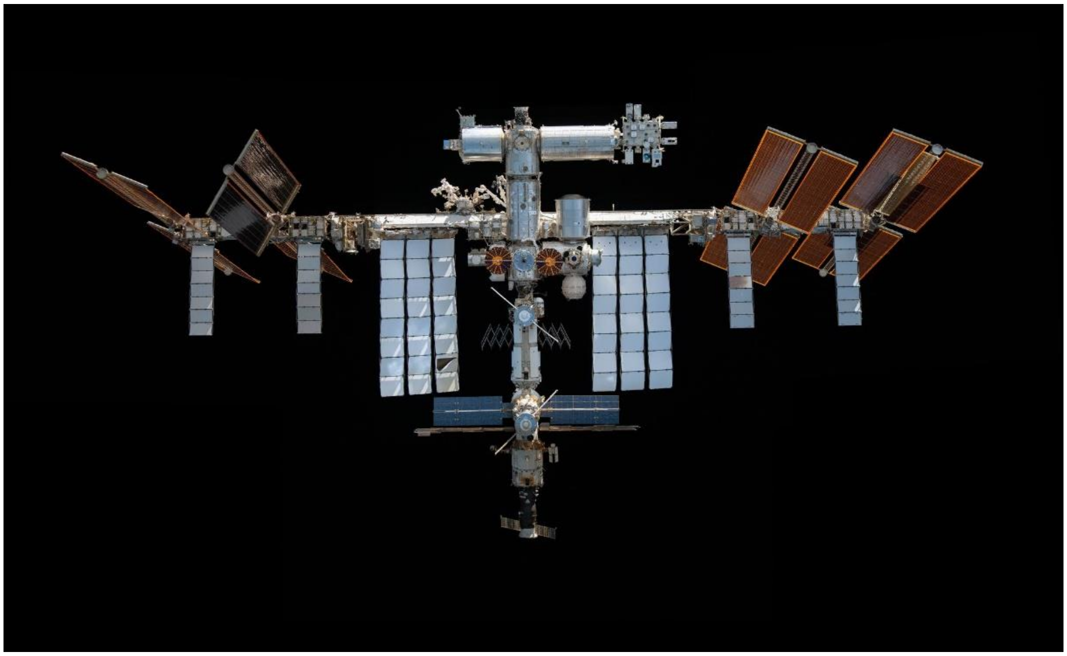

Figure 1.1 International Space Station reproduced from [1].

GaAs-based solar cells on the MIR space station, launched in 1986, produced 180 W/m^2 of power per unit area [10,11]. The fabrication of heterogeneous epitaxy and the use of multi-junction architecture led to the improvement in efficiency of GaAs SC [12–15]. The development of multi-junction solar cells marks a significant advancement in PV technology as a power source for satellites[16,17]. The optimization of the light absorption process led to the use of two or more light harvesters based on III-V semiconductors, which achieved the highest efficiency and radiation resistance among all PV technologies for space [18–20]. Commercially available solar cells for space applications are based on Si or III-V semiconductors such as Ge, GaAs, and InP [21]. Specifically, AZUR SPACE Solar Power GmbH practically fabricated the GaInP/GaInAs/Ge multi-junction solar cells (MJSC) and reported an efficiency of 26.5% at the end of life [18]. Still, Si-based solar cells are widely applied in satellite powering, despite the variety of choices related to the absorber layer, architecture, and different cost production. Nowadays, the highest efficiency solar cells revealed by four-junction with multiple absorber layer in structure AlInGaP/AlInGaAs/InGaAs/Ge which is qualified for space application by European and American standards [22,23].

The first step in the study of radiation resistance of inorganic solar cells is examining the impact of charged particles such as proton and electrons with energies up to several hundreds MeV and energy up to 10 MeV, respectively [24,25]. Literature shows that in GaAs/Ge solar cell is the most degradation caused by proton with energy with 170 keV due to the formation radiation indeed defects within deep energy levels in the space charge region [26]. The mechanism of degradation in solar cells are caused by radiation-induced defects which increase the level of recombination centers causing the recombination of electron-hole pairs before the extraction of charge carriers reducing thereby short-circuit current. Specifically, radiation-induced defects in the deep energy levels of the valence and conduction bands decrease the open circuit voltage.

Despite their high resilience to irradiation, multi-junction solar cells are not appropriate for space operation because of their high-cost fabrication, rigidity and very low specific power. Among inorganic solar cells, Cu(In,Ga)Se2 (CIGS) is appropriate due to its relatively cheap fabrication, lightweight architecture, and a possible fabrication on flexible substrates [27,28]. However, CIGS solar cell possess a relatively low efficiency with 23.4 % , despite the highest radiation resistance. Compared to other semiconductors made using the solution processed method, perovskite solar cells have a high PCE [29–31]. This is because they have high absorption coefficients, a direct bandgap transition, a long diffusion length, a low effective mass, and charge carriers that move around easily. Interestingly, a perovskite material reveals unique features such as a self-healing mechanism [32,33].Compared to inorganic solar cells, PSCs have superior tolerance and robust stability under dose of 10^{16} and 10^{15} particles/cm^2 of electrons (1 MeV) and protons (50 KeV) [27,32,34,35]. A tandem solar cell with a perovskite/CIGS photoactive layer that keeps 85% of its original efficiency under 68 MeV proton radiation is a good candidate for a space photovoltaic. According to article [36], indirect irradiation degrades PSCs by causing the segregation of the halide phase, which results in a loss of photocurrent. Another intriguing result of irradiating PSC with gamma rays is the absence of radiation-induced defects, paving the way for the use of perovskite in detectors [37]. In contrast to gamma irradiation, fast neutrons form radiation-induced shallow traps in the perovskite active layer, thereby decreasing the PCE of PSC[38–40]. The perovskite solar cell uses silicon oxide as an encapsulation layer, which reveals radiation resistance to high fluences of proton irradiation, alpha irradiation, and atomic oxygen, extending a device's lifetime in LEO by 20 times[41].

Currently, satellite internet constellations presents a network of satellite orbiting in Low-Earth Orbit (LEO) for internet service [42]. The lifetime operation of a satellite is usually in the range of 3-4 years with ≈ 90-min day/night the cycle powered by solar arrays [42]. Practically, one of the cheapest solar cells already applied to power Starlink mega constellation satellites are powered by Si- single junction with medium efficiency and low specific power [43]. A high demand of internet is planned to be covered by the network of satellites of the SpaceX Starlink with 42 000 LEO satellites, Amazon's Project Kuiper with 3236 LEO satellites and the UK government's One Web containing 48 000 satellites [44–46].

To power global satellite network, it requires the solar power generation of in the range of gigawatts level [42] is required. Based on analytical estimates, satellite power consumption is projected to grow from 1MW to 1 GW during the next ten years, with power generated by photovoltaic systems in LEO [42]. PV installations based on semiconductors, such as III-V and Si solar panels, are now used by spacecraft and satellites; nevertheless, the high cost of manufacturing and their poor radiation resistance elevate the expense of satellite operation in space. A strong interest in the exploration of outer space led to an expansion of research on solar cells that are effective, low-cost, and mainly lightweight. Currently, the cost of transferring materials to space is around US$4,000 per kilogram, which creates an opportunity to explore lightweight solar cells [42]. Usually, it is widely accepted to judge the photovoltaic arrays by their efficiency. However,in space, the most important figure of merit is so called specific power (W/kg) which help to identify the relationship of the specific power to the photovoltaics' array mass. Commercially available inorganic solar cells have a specific power of 0.7 W g-1 (GaAs), whereas perovskite solar cells, which have lately gained popularity in space application research, have a higher specific power of 29.4 W g-1 [39,47,48].

In terms of the specific power parameter, the ultraflexible OSC have recently achieved remarkable results, with a power conversion efficiency (PCE) of 15.5% and a specific power of 32.07 W g-1, as reported in a recent publication [49]. A comparison investigation revealed that the production cost of PV for internet constellations using perovskite absorbers ranges from $70M to $1.1B, whereas the cost for III-V triple junctions ranges from $10B to $19B [42]. Thus, the solar cell market seeks the alternative innovations in terms of power-cost relationships.

The OPV system outperforms other systems in terms of specific power and cost of manufacturing solar cells due to its lightweight and low-cost solution processing methods. In this consideration, organic solar cells are a potential candidate for space application due to their lightweight and low-cost nature. A wide global research in the new types of solar cells has been increasing the power certificate efficiency of perovskite and organic solar cells nearly reaching 26.7 % and 19.2 % [50,51].

1.2 Space Environment

Learning about the space environment and how it affects spacecraft is the biggest challenge in operating PV in space. According to the NASA Marshall Space Flight Center, there are several components of space environment that must be taken into account for the operation of solar arrays in space [52,53].

The list of natural space environment:

1) *Solar wind or plasma.* The flow of charged particles out of solar corona can affect the solar arrays and spacecraft's by causing the consequence of surface charging, power loss, electrostatic discharge, and the short-circuit in electronics [54–57]. The special cover material serving as shielding can protect the space technology.
2) *Radiation.* The Van Allen radiation belt, which primarily consists of charged protons and electrons, neutrons, ultraviolet rays and x-rays, is the environment in LEO , where a satellite network and the International Space Station (ISS) are orbiting. The interaction of protons with matter in space causes the most noticeable degradation in semiconductors due to ionization and lattice displacement; the energy of protons ranges from 30 keV to 10 MeV [58]. Indirect irradiations such as neutrons and γ-rays presenting as indirect irradiation cause the deteoriotaion of stability due to scattering or recoiling of nuclei. Therefore, the degradation of solar array is influenced by the particle type, energy, fluence, shielding, and cell design, including layer thickness and the number of junctions [59].To provide accurate solar cell performance measurements, the AM0 solar spectrum, with a total radiation of 136.7 mW cm^{-2}, should be used, as sunlight in space has a higher concentration of ultraviolet rays and lacks the effect of atmospheric scattering and absorption.
3) *Thermal cycles.* Space technology must withstand the temperature cycles ranging from -100 °C to 100°C every 45 min. This effect is raised due to the lack of atmosphere for heat transmission and dissipation[60]. To be specific, space technology under thermal cycling

undergo to thermal-induced stress leading to defects and de-lamination owing to differences in the thermal expansion coefficients of multilayer devices [61].

4) *High Vacuum.* The atmospheric pressure steadily drops with the increasing of the distance from the Earth. LEO is considered as a high vacuum environment, with atmospheric pressure ranging from 10^{-5} to 10^{-6} Pa. The influence of ultra-high vacuum on materials used in space technology can be seen in adhesion and cold welding, as well as in processes such as evaporation, sublimation, and decomposition. Furthermore, atomic oxygen may damage space technology via the breaking of chemical bonds, surface oxidation, and material erosion [60].

1.3 Organic Photovoltaics

Organic photovoltaics (OPVs) rely on carbon-based materials as the photoactive layer that convert light into electrical energy; it is a type of thin-film photovoltaic technology that is relatively cheap. The advantages of OPVs are their molecular level tunability, low weight, thin profile, and solution processability [62]. Organic solar cells have the potential to be a green-solvent-processable candidates in renewable energy technology, and they also exhibit a semitransparent property, as illustrated in **Figures 1.2 a and b** [2,3]. Materials often comprise many elements; organic semiconductors predominantly consist of carbon and hydrogen atoms, along with heteroatoms such as sulfur, oxygen, and nitrogen. Organic semiconductors have semiconducting characteristics due to a particular electronic structure. The simple molecule with a double bond, ethane, explains the semiconducting properties. The ethane is composed of hybridized C-atoms, each of which forms two o-bounds with H-atoms and one with a neighboring C-atom. The C-atom has four valence electrons. Because of this, one electron stayed free in the pz orbital overlapping, which created the coupled, delocalized systems of electrons that make the material semiconducting. Conjugation is characterized by a system of overlapping p-orbitals containing delocalized electrons in a molecule. This conjugation generally stabilizes systems, resulting in a lowering of the bandgap (Eg), and enables carrier transit of delocalized electrons in the π-bonds, so imparting semiconducting properties to conjugated organic molecules and polymers. The highest occupied molecular orbital (HOMO) and lowest unoccupied molecular orbital (LUMO) will be formed by the full π-bonds and empty π*-bonds, respectively[63]. The energy distinction between the HOMO and LUMO determines the bandgap of the semiconductor, usually portrayed as the valence band (EV) and conduction band (EC) in conventional semiconductors [64].

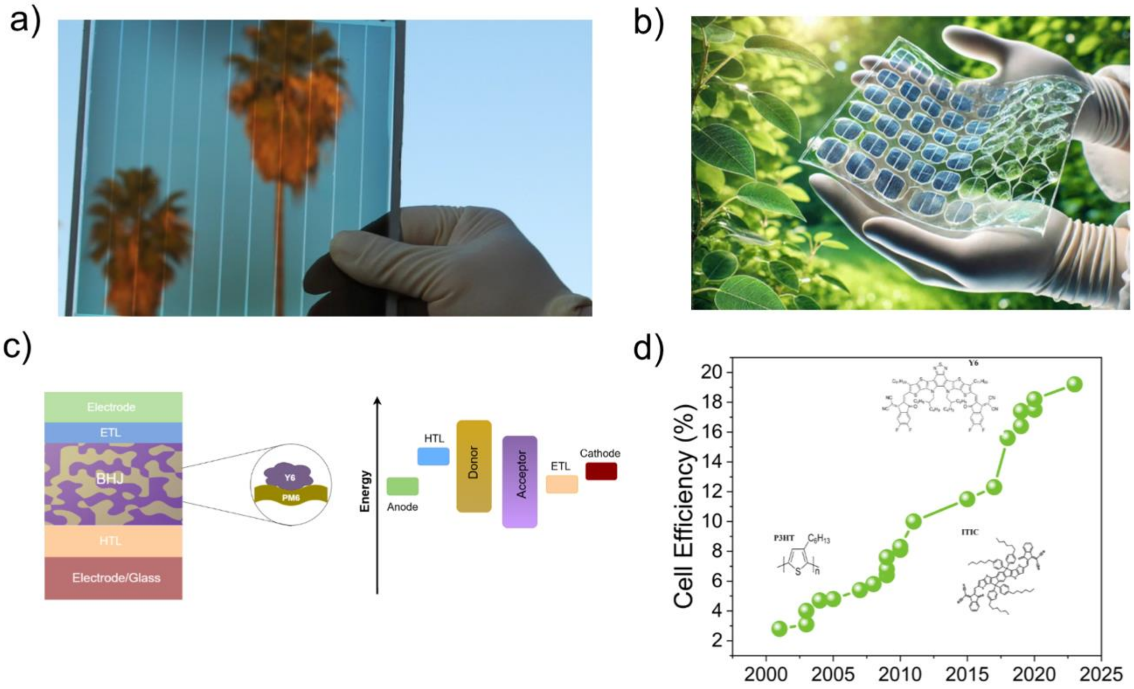

Figure 1.2 a) Photo of the real OSC with semitransparent properties, reproduced from [2] b) Green-solvent processable OPV, reproduced from [3] c) structure of OSC and energy diagram d) performance of solar cell vs discovered years.

Due to their mobility and electron affinity, fullerene type acceptors were widely used in organic solar cells, achieving a PCE of 13% (as shown in **Figure 1.2 d**). On the other hand, using Y6 and PM6, which are non fullerene acceptors, as acceptor has enhanced OSC performance, leading to a high PCE of 15.7%, a V_{OC} of 0.825 V, a J_{SC} of 25.2 mA/cm^2, and a fill factor of 74%[65]. With a photoactive material thickness in the range of 100 nm and optical band gap characteristics that are simple to modify, organic semiconductors are able to absorb photons from the ultraviolet to the near-infrared spectrum, compared to inorganic semiconductors [66].

For this study, we used PM6 as a donor and Y6 as the acceptor. Y6, in particular, utilizes the advantages of a benzothiadiazole (BT) core to optimize its absorption and electron affinity, as well as a ladder-type electron-deficient-core based central fused ring (dithienothiophen[3.2-b]-

pyrrolobenzothiadiazole) [65]. **Figure 1.3** shows the chemical structure of the PM6 donor and the Y6 acceptor.

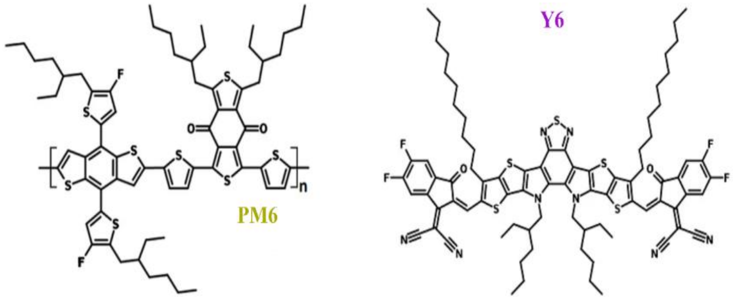

Figure 1.3 Chemical Structure of PM6 and Y6.

In a basic solar cell device, incoming photons from sunlight are converted into electrical current. The device operation of OSC can be explained in four essential steps: (i) Absorption of the incoming photon and production of excitons (ii) Diffusion of excitons (iii) Dissociation of excitons because of to the high electron affinity of acceptors and (iv) Collection of charges at electrodes. **Figure 1.2c** shows the working mechanism of OSC. The fundamental characteristic of semiconductor materials is the energy band gap, also known as the HOMO-LUMO gap, which determines the material's interaction with light and its conductivity. When a photon with higher energy than the energy band gap illuminates an organic solar cell, it excites an electron from the HOMO level to the LUMO level. Next, electron-hole pairs are created, calling it exciton as shown in **Figure 1.4 a and c**. Due to low dielectric constants of $\varepsilon \approx 2$-3, those electron-hole pairs are bound by Coulombic forces (typically 0.3–0.5 eV) owing to a large exciton binding energy [67,68]. The interfacial energy alignment between D and A, along with the charge transfer states, drives the generation of free charge carriers at the interface. **Figure 1.4 b** presents how electrons and holes separation into free charge carriers at the interfaces[69]. Exciton dissociation generates electrons and holes, which then travel to the electrodes via the donor and acceptor as displayed in **Figure 1.4 c and d**. Free carrier charge transfer takes on a timeline of nanoseconds [62].

The bulk heterojunction layer is created by a blend of p-type donors (D) and n-type acceptors (A) , providing a potential solution to overcome large exciton-binding excitons. The blend consist of a complex network of interpenetrating donor and acceptor phases that encompasses large interfacial areas within the donor- and acceptor-rich domains. Size, purity, degree of mixing, molecular packing, and crystallinity characterize the domains created by the blend of donor and acceptor organic materials [70]. Improved stability, solubility, crystallinity, and reduced energy loss have allowed organic solar cells to attain a high efficiency of about 20% since the creation of the Y6 acceptor and the mix of PM6 as donor and Y6 acceptor.

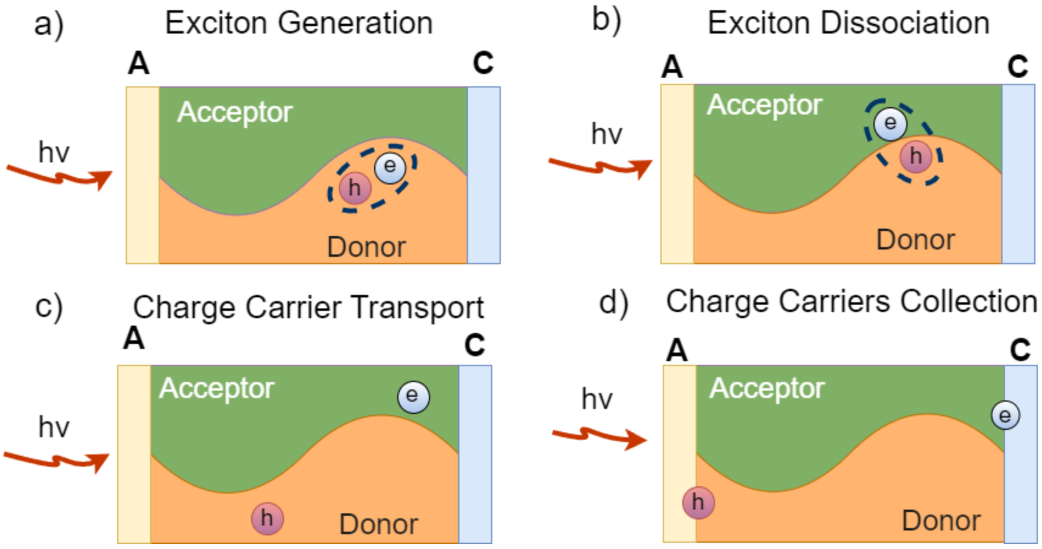

Figure 1.4 Four steps of physical processes in organic solar cells.

In general, the device structure of organic solar cells consists of a photoactive layer sandwiched between two electrodes: cathode and anode. By connecting the cathode and anode with a metallic wire, the electrons in the two electrodes undergo redistribution until equilibrium is achieved. The redistribution of charges generates a built-in potential difference between the two electrodes, producing a built-in field throughout the device. This built-in electric field forces the photo-generated free charge carriers to the appropriate electrodes for extraction, generating photocurrent that flows in the external circuit, measurable by an ampermeter in the outside circuit [71]. Over the years, the development of organic solar cells has improved the charge extraction process by implementing transport layers with suitable work functions, leading to the invention of new device architectures. To achieve this, the work function of the transport layers must align with the energetic levels of the donor and acceptor materials, thereby defining the polarity of the device. Additionally, the transport layer provides good contact with electrodes and charge selectivity prevents charge carriers from reaching the opposite electrode [72]. Specifically, device structure of organic solar cells can be classified as inverted and conventional as shown in **Figure 1.5**. The structure of Glass/ITO/ZnO/D:A/MoOx/Ag as depicted in the **Figure 1.5 a**, achieves the best performance among the different transport layers applied in the inverted device architecture. The conventional device structure achieves the best performance (19.2%) with the Glass/ITO/PEDOT:PSS/D:A/PNDIT-F3N/Ag structure [51]. The transport layer enhances device performance by reducing leakage current, increasing the Voc through the appropriate WF of the transport layers, reducing the interfacial recombination rate, and regulating the morphology of the D:A blend [73–75]. After 300 hours of illumination, the inverted organic solar cell is more stable, keeping 73% of its initial PCE. The standard device, on the other hand, only saves 5% of its initial PCE [76]. However, the conventional organic solar cell achieves better performance compared to the inverted one.

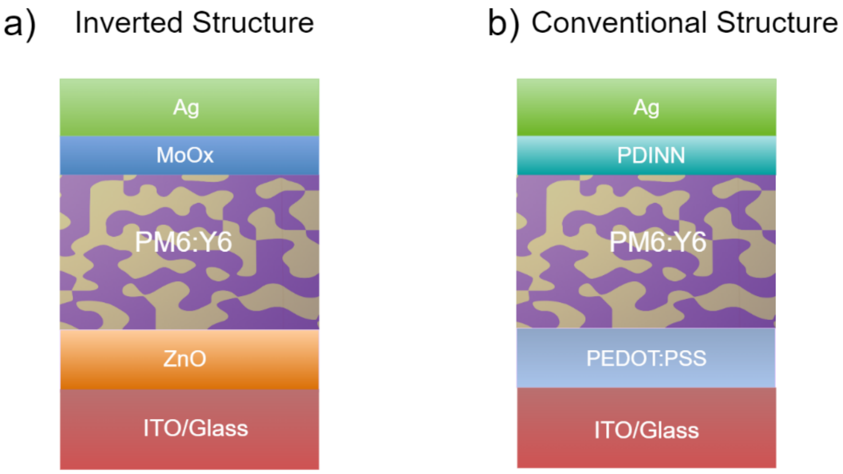

Figure 1.5 a) Inverted structure and b) Conventional structure.

1.3 Synopsis of Chapters

Chapter 2

This chapter provides the readers with an overview of techniques used in this thesis for a variety of research purposes. It explains the fundamental information about the techniques and methods applied for the research. Specifically, the state-of-the-art technologies utilized for material characterization include XPS, TEM, AFM, ellipsometry spectroscopy, UV-Vis spectroscopy, and Hall measurements. Furthermore, the surface recombination subchapter explains how the multi-mechanism recombination model used to analyze the intrinsic and doped properties of the active layer was derived. The slope as a function of surface trap density, which can be calculated from the modeling of the open circuit voltage dependency on light intensity, showed an interesting difference between the intrinsic and doped active layers. For the investigation of device physics mechanisms, the impedance spectroscopy, EQE, and J-V techniques are used in this thesis.

Chapter 3

This chapter unravels the principal impact of proton irradiation and thermal annealing on organic solar cells with diverse thicknesses of the absorber layer, focusing on the mechanisms, such as recombination, generation and extraction. Specifically, we examine the effects of ultra-thin and thick absorber layers with thicknesses of 60 nm, 100 nm, 260 nm, and 400 nm. To understand the influence of proton irradiation and post-annealing on PM6:Y6 thin film, material characterization features such as morphology, roughness, and optical properties were investigated using the state-of – the-art equipments. In order to delve into the influence of the space environment on the performance of solar cells, we tested organic solar cells with different thicknesses of absorber layer, each fabricated with optimized recipe to achieve approximately the same, particularly for PM6:Y6 blend with 260 and 400nm thick absorber layers [77]. The energy loss of protons within the device structure is modeled using the SRIM software package. Recombination dynamics were investigated using the impedance spectroscopy in conjunction with a multi-mechanism recombination model. The generation rate simulation is based on the transfer matrix method with optical parameters of each functional layer. The extraction parameter of organic solar cells is based on mobility and lifetime parameters.

Chapter 4

In this chapter, the focus will be placed on the radiation resistance of the transport layers and electrodes. More specifically, we aim to compare the conventional and inverted structure with the same PM6:Y6 active layer under proton exposure to evaluate the device performance and recombination process.To track change in material features exposed to proton irradiation, the optical and structural properties of the transport layers and electrodes were investigated using the state of the art of instruments.

Chapter 5

The study concentrated on the degradation mechanism of TiN thin films on quartz and sapphire substrates subjected to electron irradiation. We elucidated the structural, chemical composition, electrical, and optical properties before to and after electron irradiation utilizing a variety of advanced material characterisation techniques.

Chapter 2 Material and device characterization tools, experimental setup of accelerator

2.1 Morphological and structural characterization

Structural and morphology features of materials are formed during the deposition process, based on molecular interactions. In the case of nanomaterials, structural and morphological parameters help determine the chemical and physical properties of the material which plays a huge role in device operation. This chapter reviews the state-of-the-art techniques used to characterize the material properties of the functional and absorber layers in the OPV field. The X-ray diffraction technique measures the phase, grain, and crystallinity of inorganic materials, while transmission electron microscopy (TEM) studies the donor-acceptor network morphology. Surface topography and roughness which affect device operation due to the junction between the active layer and transport layers are investigated by Atomic Force Microscopy and Scanning Electron Microscopy.

2.1.1 Transmission Electron Microscopy

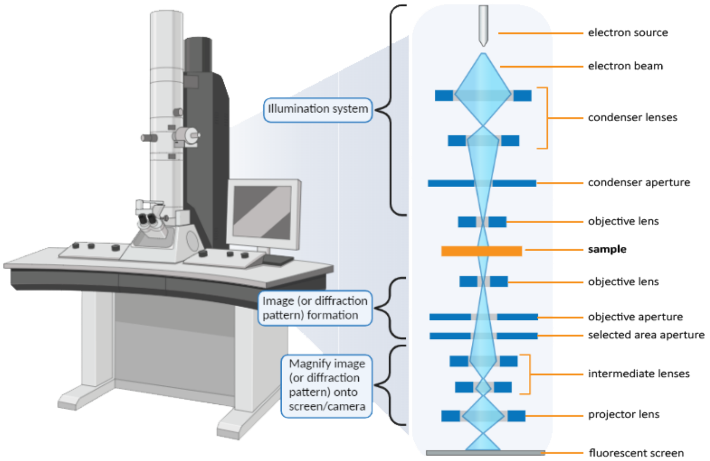

Figure 2.1 Elements of Transmission Electron Microscopy (reproduced from [4]).

The Transmission Electron Microscope (TEM) contains an electron source, condenser and objective lenses, objective aperture, intermediate lenses, projector lens, and a fluorescent screen, as seen in the schematic design in **Figure 2.1**. An accelerated high-energy electron beam is focused by electromagnetic lenses and apertures onto the sample, while minimizing deformation, and detected by a fluorescence CCD camera [78]. Transmission electron microscopy is able to image the morphology of materials at the resolution of 0.2 nm due to the dual nature of electrons. One of the main parameters in microscopy is resolution, which is the smallest distance at which two neighboring points can be distinguished depending on wavelength. In OPV, the active layer, considered as the mixture of donor and acceptor materials, forms grains and their size affects the generation and recombination of charge carriers. Therefore, it is important to consider the morphology of the blend. For example, **Figure 2.2** presents the morphology of PCE10: COTIC-4F with 40 % weight of PCE10 in the blend. TEM was used to identify the morphology of the blend for Chapter 3 of this thesis.

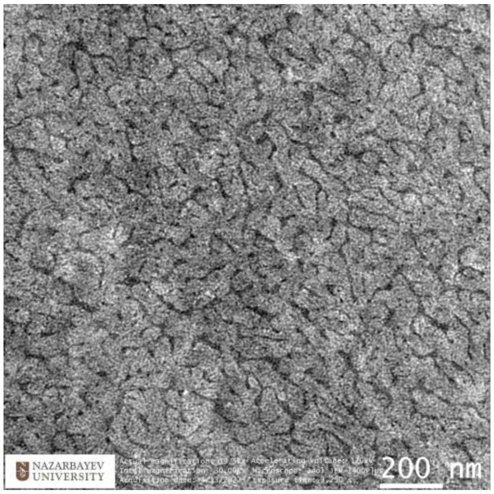

Figure 2.2 . The morphology of the blend consists of donor material as PCE10 and acceptor as COTIC-4F at 30K total magnification.

2.1.2 Atomic Force Microscopy

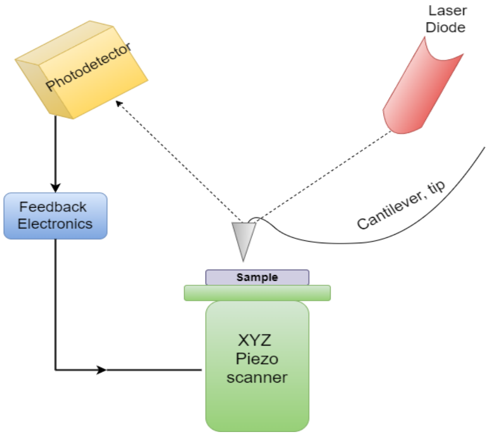

Figure 2.3 Schematic configuration of Atomic Force Microscope.

Atomic Force Microscope (AFM) is a non-destructive tool applied for morphology and topography characterization of the sample surface in nanoscale. Additionally, the AFM system is used to characterize the roughness of the sample at the nanoscale. In AFM, a nanoscale tip is connected to a tiny cantilever that functions as a spring. Upon contact of the tip with the surface, the cantilever undergoes bending, which is monitored using a laser diode and position sensitive photodetector. This deflection signifies the contact force between the tip and the sample [79]. In this manner, the topographical image may be obtained by determining information about the surface height. This mode of Atomic Force Microscopy (AFM) is referred to as contact mode. The AFM system is utilized to measure the surface morphology and roughness of the active layer and transport layers in organic photovoltaic (OPV) devices.

2.1.3 Grazing Incident X-Ray Diffraction

When radiation interacts with material, two effects can occur: scattering and absorption. The interaction of soft X-rays with matter results in elastic scattering while preserving the initial energy of the radiation. Analysing the so-called diffraction spectrum allows us to characterize the crystal structure of the material. The diffraction spectrum presents the intensity of scattered radiation on the x-axis as a function of the scattering angle. The diffraction angle and the intensity of scattered radiation determine the unit cell dimensions and chemical species, as well as their geometrical relation to the lattice points, respectively [78]. In order to describe the relationship between crystal structure and diffraction spectrum, there is Bragg equation bounding those parameters as:

$$n\lambda=2d\sin\theta \tag{2.1}$$

where n is an integer, λ is the wavelength of the radiation, d is the spacing of the crystal lattice planes, and θ is the diffraction angle. Grazing Incidence X-ray Diffraction (GIXRD) facilitates more accurate characterisation of thin films.This approach can also be employed to examine the impact of various surface changes. Additional prevalent applications encompass the detection of unidentified coatings and thin films, as well as examining the impact of certain processing conditions on coatings.Samples having thicknesses from a few nanometers to one micrometer, exhibiting RMS surface roughnesses below 10 nm, are optimal for GIXRD analysis. Samples that are thicker and rougher may also be studied; however, the quality of the data often diminishes as thickness and roughness rise.

An X-ray diffractometer includes an X-ray source, an X-ray generator, a diffractometer assembly, a detector assembly, and systems for collecting information and processing. X-ray diffraction system SmartLab by Rigaku company with Cu 1.54 A wavelength was used for identifying crystal structure of functional layers in OPV. Measurements using GIXRD patterns are used in Chapters 4 and 5.

2.1.4 X-ray Photoelectron Spectroscopy

The surface-sensitive analytical technique known as X-ray photoelectron spectroscopy is a widely used scientific tool for determination of chemical bounds, states, and elements. Characteristic x-rays as photons in a monochromatic beam are used as an incident beam on the material and absorbed by the atoms of the material. Secondary electrons are ejected from the material with a certain kinetic energy due to this interaction. Then, kinetic energy is determined as the difference between the energy of the incident photon and the energy required to displace the secondary electron from the material's atom. The concept of binding energy determines the electron's energy attached to the atom/orbital. As a result, the sum of the binding energy, the kinetic energy of the electron, and the work function of the spectrometer must be equal to the incident photon energy[80]. This process can be described mathematically by the following equation:

$$h\upsilon = BE + KE + \Phi_{spec} \tag{2.2}$$

where $h\upsilon$- is the energy of the x-ray, BE is the binding energy of the electron, KE is the kinetic energy of electron and Φ_{spec} is the spectrometer work function. Electron's binding energy is a material characteristic that is unaffected by the x-ray source used to expel it. The results of measurements is presented in the dependence of intensity on the binding energy of electron. Photoelectron peaks are assigned by the element and orbital from which they were emitted. For instance, "O 1s" refers to electrons ejected from the 1s orbital of an oxygen atom. The results of XPS measurements are presented in Chapter 5.

2.2 Optical Characterization

2.2.1 UV-vis spectrophotometer

The UV-vis spectrophotometer measures the light passed through a matter and the amount of absorbed light at each wavelength by that material, specifically, the ultraviolet and visible light ranges. The quantity of light absorbed is directly proportional to the amount of the absorbing element in the sample. When photons interact with the electron cloud of a chromophore, the electrons in the cloud are excited to higher energy molecular orbitals, creating an excited state. This is the fundamental concept of a UV-vis spectrophotometer [81].The absorbance of the organic semiconductor thin film refers to the ability of molecules or atoms to excite a change in the internal energy by visible, ultraviolet and near-infrared light. Transmission is the portion of light that passes through the thin film. The superposition of the relative amount of absorbed, transmitted and reflected light should be unity as presented in the equation. Based on the equation, transmittance refers to the light that is not absorbed, scattered, or reflected.

$$R+T+A=1 \tag{2.3}$$

Another parameter is reflectance which is the portion of reflected light by the thin film’s boundary. The equation for absorbance is given as the decadic logarithm of the ratio of the measured intensity passing through the thin film to the total incident light:

$$A=-\,log(\frac{I}{I_0}) \tag{2.4}$$

Refractive index and extinction coefficient can be governed by transmittance and reflectance measurements of thin film as depicted in equation. In the case of the refractive index, is assumed that the interference effect is absent and that $n^2 \gg k^2$; thus, approximation of refractive index is presented in the following equation[82]:

$$n=\left|\frac{1+R^2}{1-R^2}\right| \tag{2.5}$$

The extinction coefficient can be obtained using thickness of thin film, reflectance and transmittance ,as presented in the next equation[82]:

$$\alpha=\frac{1}{d}\ln(\frac{(1-R)^2}{2T}+(\frac{(1-R)^4}{4T^4}+R^2))^{0.5} \tag{2.6}$$

$$k=\frac{\alpha\lambda}{4\pi} \tag{2.7}$$

UV-Vis spectrophotometer is a complex system including a source of light, detector, signal processor, optical system, beam splitting system and the integrating sphere. This tool is able to measure the reflection, transmission and absorbance of thin films in the range of 175-3300 nm. The measurement of transmittance and reflectance, the calculated refractive index, and the extinction coefficient are used for the calculation of generation rate in OPV for Chapters 3 and 4, and 5.

2.2.2 Ellipsometry Spectroscopy

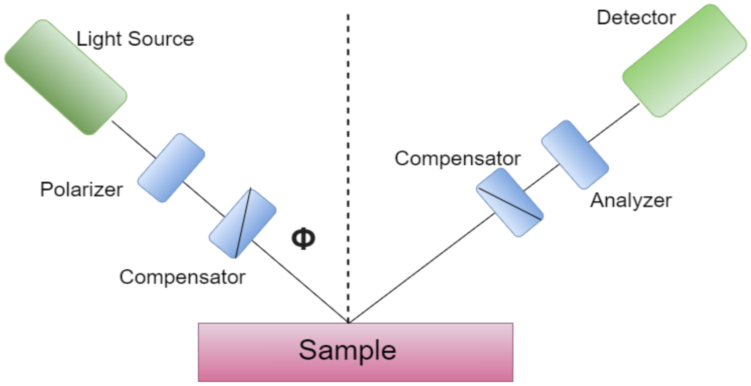

Figure 2.4 Schematic diagram of ellipsometry spectroscopic.

Ellipsometry spectroscopy is a non-destructive technique that measures the optical characteristics of thin film using linearly polarized light. Ellipsometry spectroscopy can be used to determine optical properties such as optical band gap, transmission, refractive index, extinction coefficient, thickness, and dielectric properties in the energy range of 0.5 to 6 eV. Basically, by focusing linearly polarized light on the sample, the detector registers the change in the reflection of the linearly polarized light. The measured characteristics , as raw data, are: Ψ which denotes the ratio of the amplitude of p to s polarized reflected light, and Δ, which indicates the phase difference. In this context, p and s are polarized lights, refferring to the electric field vectors directed parallel and perpendicular to the plane of incidence, respectively. To gain the optical properties of materials, the raw data (Ψ, Δ) has to be fitted to certain optical models with numerical approximations. Before the measurements, the sample should be homogeneous and isotropic [83].

2.3 Electrical Characterization

2.3.1 Van der Pauw Measurements

The Van-der Pauw technique is used to determine the electrical characteristics of thin films such as charge carrier density, resistivity, conductivity, and Hall mobility. The four point probe position method is applied to the sample in order to measure the average resistivity.

Resistivity Measurements

Current is applied through two terminals on the sample, and the voltage drop is measured across the opposite two terminals, as shown in Figure 2.5. The series of eight voltage measurements (for different current flow directions and terminal pairs V1-V8) and the test current (I) are used to calculate the resistivity (ρ) based on the following equation [84]:

$$\rho = \frac{\rho_1+\rho_2}{2} = \frac{\pi d}{ln2}\left(f_1\left[\frac{V_1-V_2+V_3-V_4}{4I}\right] + f_2\left[\frac{V_5-V_6+V_7-V_8}{4I}\right]\right) \qquad (2.8)$$

Where ρ_1 and ρ_2 are volume resistivities, d is the sample thickness, *V1-V8* represents the voltages measured by the voltmeter, I is the current through the sample, f_1, and f_2 are geometrical factors based on sample symmetry ($f_1 = f_2 = 1$ for perfect symmetry)

.

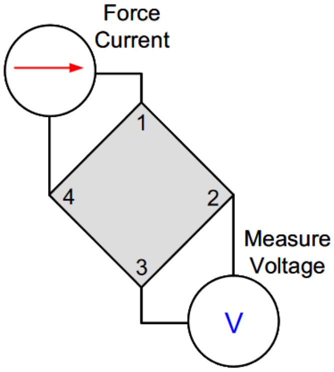

Figure 2.5. Van der Pauw configuration (, reproduced from [84]).

Hall Voltage Measurements

With an applied magnetic field, the Hall voltage is measured using the *I-V* measurement configurations shown in Figure 2.6.

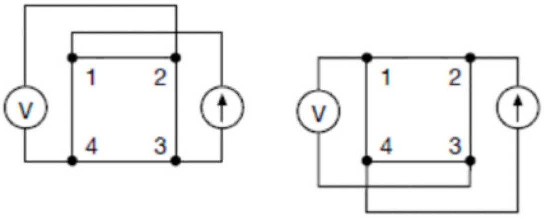

Figure 2.6 Hall voltage measurement configurations (, reproduced from [84]).

With a positive magnetic field (B) applied perpendicular to the sample, a current is passed between terminals 3 and 1 (I31pBp), and the voltage drop (V24pBp) between terminals 2 and 4 is measured. Then, the current is reversed (I31nBp), and the voltage drop (V24nBp) is measured again[84]. This process of reversing the current is used to eliminate offset voltage. Next, a current is applied from terminal 2 to terminal 4 (I24pBp), and the voltage drop (V13pBp) between terminals 1 and 3 is measured. The current is then reversed (I24nBp), and the voltage drop (V13nBp) is measured again. The magnetic field is reversed (Bn), and the measurements for voltage drops V24pBn, V24nBn, V13pBn, and V13nBn are repeated. From these eight Hall voltage measurements, the average Hall coefficient can be determined using the following formula:

$$R_{HC} = \frac{d}{4BI}(V24pBp - V24nBp + V24nBn - V24pBn) \tag{2.9}$$

$$R_{HC} = \frac{d}{4BI}(V13pBp - V13nBp + V13nBn - V13pBn) \tag{2.10}$$

Where R_{HC} and R_{HD} are Hall coefficients, *d* is the sample thickness, *B* is the magnetic flux density, *I* is the current, and *V* represents the voltages[84]**.**

Once R_{HC} and R_{HD} have been calculated, the average hall coefficient (R_{HAVG}) can be determined as follows:

$$R_{HAVG} = \frac{R_{HC}+R_{HD}}{2} \tag{2.11}$$

The carrier density was determined as follows:

$$n = -\frac{1}{qR_{HAVG}} \tag{2.12}$$

2.3.2 Electrical Characterization

In order to characterize the electrical performance of organic solar cells, they are presented as the union of ideal electronic components. **Figure 2.7** illustrates an electrical circuit consisting of a photocurrent source, diode, series resistance, and shunt resistance connected in parallel. The photocurrent source generates free charge carriers under illumination while the diode possesses the saturation current. The generated free charge carriers can be extracted or recombined. The total J-V characteristics of the device under illumination correspond to the sum of the dark current and the photocurrent in equilibrium:

$$J(V) = J_0\left[\exp\left(\frac{qV}{n_{id}kT}\right) - 1\right] - J_{ph}(V) \tag{2.13}$$

where J_0- the dark saturation current density, n_{id}- the ideality factor determining the recombination mechanism in OSC, and J_{ph}- photocurrent density, q—elementary charge, T—absolute temperature, and k_B—Boltzmann constant. It is important to highlight that the OSC device is not an ideal diode; therefore, series resistance and shunt resistance are included to represent the real OSC characteristics. Considering the series resistance, it takes into account the voltage drop in both the electrodes and the connecting cables. A device's shunt resistance gauges the amount of current leakage resulting from either material or energetic disorder. The following equation expresses the corrected Schockley diode equation for OSC [62]:

$$J = J_0 \exp\left[\frac{q/(V_0 - JR_S)}{n_{id}Tk_B} - 1\right] + \frac{V - JR_S}{R_{sh}} - J_{ph} \tag{2.14}$$

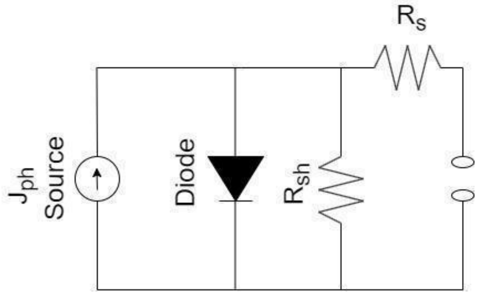

Figure 2.7 Equivalent circuit a of solar cell.

2.3.3 J-V Charcateristics

The J-V charcateristics of OSC are the sum of the diode performance in the dark mode with the light generated current. Under an applied bias, the potential difference generates the dark current in the device in the opposite direction to the photocurrent. **Figure 2.8** shows that the dark current is relatively small under reverse bias and increases under forward bias. The rectifying operation in

PV devices indicates the presence of an asymmetric junction in the device structure, which is responsible for separating charges[62,70]. The illumination causes the J-V curve to shift into the fourth quadrant, providing power extraction from the diode.

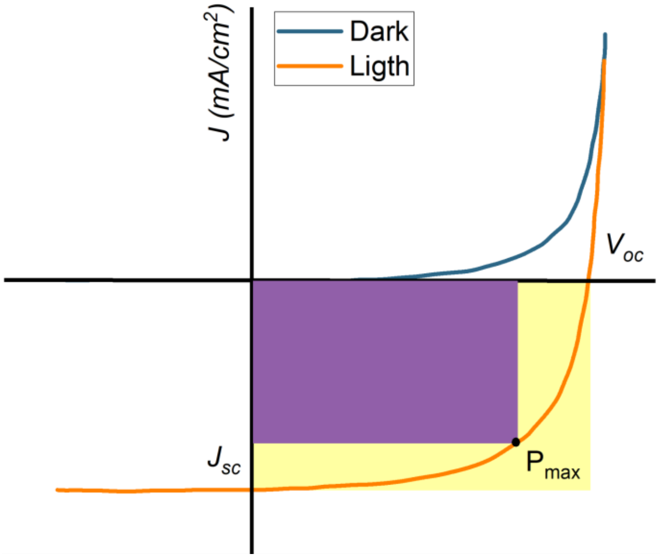

Figure 2.8 J-V characteristics of solar cells under dark and light illumination.

Typically, reverse and forward bias modes present different physical characteristics of solar cells. Reverse bias gathers the current through thermalization and leakage. When reverse bias is applied, electrons and holes flow in the opposite direction from the pn junction [62,70]. Under forward bias, the current -voltage is characterized by an exponential function, and electrons and holes flow toward the pn junction to recombine [62,70].To characterize the operating conditions of solar cells, one can determine the figures of merit from **Figure 2.8**, which include short-circuit current, open circuit voltage, and fill factor. Light-generated carriers are generated and extracted, which results in the short-circuit current under zero applied bias. In an ideal solar cell with minimal resistive loss, the short-circuit current and the light-generated current are equivalent. Consequently, the short-circuit current represents the maximum current that can be extracted from the solar cell.The next parameter is the open circuit voltage which defines the electrical potential of the device. At the voltage condition V_{OC} , the illuminated device has no current flow because of the application of external bias. All photogenerated charge carriers are recombined in solar cell and can not be extracted by electrodes under open circuit voltage conditions. Therefore, the current density of generated charge carrier is equal to the recombinaed current density as presented in equation 2.14:

$$J_{gen} = J_{rec} = qdR \tag{2.15}$$

The equation 2.16 presents the open circuit voltage identified using the saturation photocurrent with the generated photocurrent at open circuit voltage. It should be highlighted that the ideality factor is equal to 1 when bimolecular recombination dominates due to $J_{gen}(\,V_{OC}) \gg J_0$.

$$V_{OC} = \frac{n_{id}kT}{q}\ln(\frac{J_{gen}(\,V_{OC})}{J_0} + 1) \tag{2.16}$$

The fill factor parameter is mostly affected by the probability of photogenerated charge carriers being collected and contributing to the photocurrent density. The Fill Factor parameter determines the field-dependence of the potocurrent density of device. Figure 2.8 illustrates the fill factor as the ratio between the purple and yellow rectangles. The fill factor is always less than 1. The following equation describes the fill factor[62,70]:

$$\mathrm{FF} = \frac{\mathrm{P_{MP}}}{\mathrm{V_{OC}I_{SC}}} \tag{2.17}$$

Power conversion efficiency of OSC, which serves as a comparative parameter, is the main characteristic of solar cells. The ratio of the electrical output power density from the device to the electrical input power density under 1 sun determines the efficiency. The product of applied voltage and corresponding current density enables the calculation of the electrical output power density at each bias. Commonly, the efficiency of solar cells is defined as the multiplication of open-circuit voltage, short-circuit current, and fill factor over the incident power, as presented in the equation[62,70].

$$PCE(\%) = \frac{FF\,V_{OC}I_{SC}}{P_{in}} \tag{2.18}$$

2.3.4 External Quantum Efficiency

The external quantum efficiency is the ratio of the incident photon flux to the electron flux in the external circuit and presents as a function of wavelength. The EQE is the result of light absorption by the blend of donor and acceptor, light absorbance by other functional layers in the device, and reflection at all interfaces. This process presents the complex interference pattern and electric field distribution in the device. To measure the EQE, the monochromatic light illuminates the device at a certain frequency and detects the photo-voltage signal with a lock-in amplifier while sweeping the wavelength [62,70].

$$EQE(\lambda) = \frac{I_{SC}(\lambda)/q}{I(\lambda)/h\nu} \tag{2.19}$$

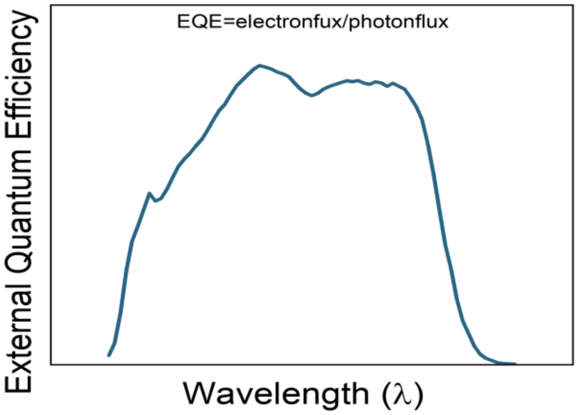

Figure 2.9 External quantum efficiency.

2.3.5 Qualitative recombination

The slope shows the relationship between V_{OC} and light intensity. Based on the relationship $V_{OC} = \partial\ \mathrm{kT/q} \cdot \ \ln(\mathrm{I})$, where k is the Boltzmann constant, T is the temperature, and q is the elementary charge, I data is used to figure out which recombination process is dominant [85]. The one should perform this measurement by measuring the current-voltage (J-V) characteristics and adjusting the intensity of light using a set of neutral density filters. A slope of 1.0 kT/q is detected when the dominant recombination process is bimolecular [62,86]. Interface traps produce a slope lower than 1.0 kT/q, indicating the dominance of surface recombination. On the other hand, a slope greater than

1.0 kT/q indicates the dominance of trap-assisted recombination. In this thesis, the dominant recombination analysis is employed in Chapter 3 and 4 .

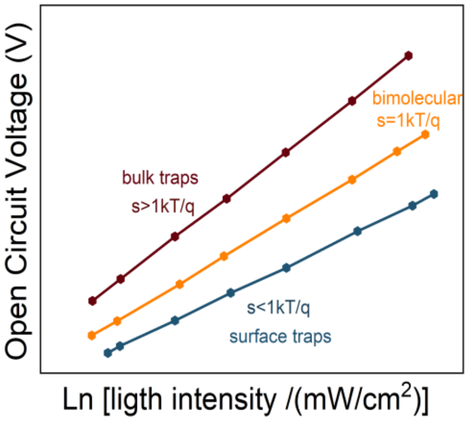

Figure 2.10 V_{OC} vs Light Intensity**.**

2.4 Surface Recombination

2.4.1 Introduction

Reducing non-radiative recombination losses is still necessary to fully overcome the performance limiting factors in organic solar cells. Surface recombination, which is non-geminate recombination, makes this goal very hard to reach. But the discovery of the non-fullerene acceptor has slowed down bulk non-geminate recombination[85,87–89]. The nature of trap-assisted surface recombination is a trap generated by in deep energy levels at the center of the energy band gap [90–92]. Surface recombination is a complicated process that involves certain characteristics of the active layer and transport layers. The doped and intrinsic nature of the active bulk-heterojunction layer is one of the poorly understood processes that define surface trap-assisted recombination losses in OSCs.

This chapter explains how surface recombination happens in both intrinsic and doped active layers, using the extended multi-mechanism recombination model that includes different recombination processes. The theoretical section explains the concept of intrinsic and the derivation of the recombination rate. This work focuses on simulating how $\mathrm{V_{OC}}$ changes at different light illumination for both intrinsic and doped active layers. It aims to identify the dominant type of recombination based on the slope as an important parameter. The second part is dedicated to the application of an analytical model to the experimentally measured recombination current of the devices to determine the characteristic parameters : direct band-to-band recombination (Langevin prefactor), recombination via a trap state within the band-gap (bulk trap cocentration), and recombination acting at an interface or the surface of the active layer (surface trap density).

2.4.2 Theoretical Part

The band gap energy of active layer can be illustrated as the difference between the HOMO (serving as E_v) and LUMO (serving as E_c) energy levels; and the device is formed when active layer is placed between anode (A) and cathode (C) as shown in **Figure 2.11a**. The Fermi level (E_{f0}) is placed in the center of the band gap. The energy-band diagram at equilibrium in the dark is depicted in **Figure 2.12b** when contact has been formed between the active layer and the electrodes. The built-in potential is equal to the difference in the work functions of the anode and cathode.The Fermi level is split into quasi-Fermi levels, E_{Fn} and E_{Fp}, when light illuminates on it. The difference between these levels determines the highest open circuit voltage (V_{OC}) that can be achieved for the structure of the device being studied under the given conditions. The intrinsic active layer implies the uniform electric field forming the linear potential distribution across the active layer. The doped active layer with certain doping contentration exhibit the linear distribution of the electric field within the depletion region adjacent to one of the electrodes forming the quadratic potential distribution (band banding).

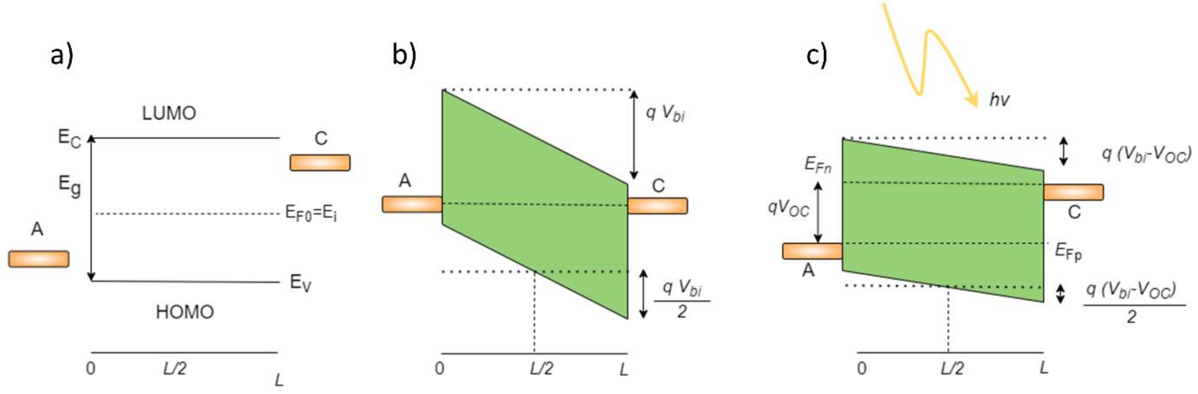

Figure 2.11 (a) Bandgap scheme of the organic semiconductor between anode and cathode in disconnected condition, integrated into an entire structure at conditions (b) dark and (c) light.

The derivation of the recombination rate equation for the doped active layer has been previously derived in the work [93]. Here, the derivation of the recombination rate for doped and intrinsic active layers is presented for better understanding.In order to study the surface recombination dynamics, we investigate the bulk charge carrier concentration (equation 2.20-2.21) and the surface traps between the active layer and electrodes (equation 2.22-2.25). The intrinsic semiconductor is connected to the anode and cathode. The equilibrium concentration of charge carriers is denoted by the concentration of electrons n and holes p at the anode (A) and cathode (C), respectively. The equilibrium charge carrier concentration for the intrinsic active layer, which is made up of the anode and cathode electrodes with various work functions in the dark, is shown by the following equations:

$$n_0 = N_c exp\left(\frac{E_c - E_{Fo}}{kT}\right) \tag{2.20}$$

$$p_0 = N_v exp\left(\frac{E_{Fo} - E_v}{kT}\right) \tag{2.21}$$

$$n_{S0(A)} = N_c exp\left(-\frac{E_c - E_{Fo}}{kT}\right) exp\left(\frac{qV_{bi}}{2kT}\right) \tag{2.22}$$

$$p_{S0(A)} = N_v\ exp\left(-\frac{E_{Fo} - E_v}{kT}\right) exp\left(-\frac{qV_{bi}}{2\ kT}\right) \tag{2.23}$$

$$n_{S0(C)} = N_c exp\left(-\frac{E_c - E_{Fo}}{kT}\right) exp\left(\frac{qV_{bi}}{2kT}\right) \tag{2.24}$$

$$p_{S0(C)} = N_v exp\left(-\frac{E_{Fo} - E_v}{kT}\right) exp\left(-\frac{qV_{bi}}{2\ kT}\right) \tag{2.25}$$

where N_c and N_v are the effective density of states for electrons and holes, and V_{bi} is the built-in voltage, E_{Fo} is the equilibrium Fermi energy.

The intrinsic concentration of charge carriers, n_i, is equal to the product of the equilibrium concentrations of electrons and holes in the bulk, as shown by equation (2.27-2.28).

$$n_o p_o = n_i^2 \tag{2.26}$$

$$n_o = p_o = n_i \tag{2.27}$$

$$n_i^2 = \sqrt{N_c N_v} exp\left(\frac{E_g}{2kT}\right) \tag{2.28}$$

The equilibrium and non-equilibrium concentrations of free charge carriers under illumination in the bulk (Equation 2.29-2.30) and at the active layer interfaces (equation 2.31-2.34) can be characterized by the following equations:

$$n = n_0+\Delta n=N_c exp\left(-\frac{E_c-E_{Fn}}{kT}\right) \tag{2.29}$$

$$p = p_0+\Delta p=N_V exp\left(-\frac{E_{Fp}-E_V}{kT}\right) \tag{2.30}$$

$$n_{S(A)} = n\ exp\left(\frac{q(V_{bi}-V_{OC})}{2\ kT}\right) \tag{2.31}$$

$$p_{S(A)} = p\ exp\left(-\frac{q(V_{bi}-V_{OC})}{2\ kT}\right) \tag{2.32}$$

$$n_{S(C)} = n\ exp\left(\frac{q(V_{bi}-V_{OC})}{2\ kT}\right) \tag{2.33}$$

$$p_{S(C)} = p\ exp\left(-\frac{q(V_{bi}-V_{OC})}{2\ kT}\right) \tag{2.34}$$

where E_{Fp} and E_{Fn} are the quasi-Fermi levels, Δp and Δn are the concentration of non-equilibrium holes and electrons.

The total amount of charge carriers at the anode and cathode when exposed to light are presented in equations (2.35-2.38):

$$n_{S(A)} = N_c exp\left(-\frac{E_c-E_{Fn}}{kT}\right) exp\left(-\frac{q(V_{bi}-V_{OC})}{2\ kT}\right) \tag{2.35}$$

$$p_{S(A)} = N_v exp\left(-\frac{E_{Fp}-E_C}{kT}\right) exp\left(\frac{q(V_{bi}-V_{OC})}{2\ kT}\right) \tag{2.36}$$

$$n_{S(C)} = N_c exp\left(-\frac{E_c-E_{Fn}}{kT}\right) exp\left(\frac{q(V_{bi}-V_{OC})}{2\ kT}\right) \tag{2.37}$$

$$p_{S(C)} = N_v exp\left(-\frac{E_{Fp}-E_V}{kT}\right) exp\left(-\frac{q(V_{bi}-V_{OC})}{2\ kT}\right) \tag{2.38}$$

The product of the electron and hole concentrations under illumination is described by equation 2.39:

$$np = n_s p_s = n_i^2 exp\left(\frac{qV_{OC}}{kT}\right) \tag{2.39}$$

The recombination mechanism through localized interface traps can be estimated using the Shockley-Read-Hall theory (SRH)[92]. The following equation represents the net recombination rate through interface traps of density N_{ts} per unit area, which create a single localized energy level Ets within the bandgap:

$$U_s = -\frac{dn_s}{dt} = -\frac{C_n C_p N_{ts}(n_s p_s - n_1^2)}{C_n(n_s+n_1)+C_p(p_s+p_1)} \tag{2.40}$$

where C_n and C_p denote the capture coefficients of electrons and holes, N_{ts} density of interface states per unit area.

According to SRH theory, deep energy levels that serve as efficient recombination sites and are located around the mid-gap (E_{ts}=E_i) are considered. In contrast to recombination, the probability of de-trapping charge carriers from shallow energy levels is higher, and they function as charge traps without significantly increasing recombination losses.

$$n_1 = N_c exp\left(-\frac{E_c-E_{ts}}{kT}\right) = n_i exp\left(\frac{E_{ts}-E_i}{kT}\right) \tag{2.41}$$

$$p_1 = N_v exp\left(\frac{E_v-E_{ts}}{kT}\right) = n_i exp\left(\frac{E_i-E_{ts}}{kT}\right) \tag{2.42}$$

Considering equation (2.41), equation (2.42) was rebuilt.

$$U_s = -\frac{C_n C_p N_{ts}(n_0 + p_0+\Delta n)\Delta n}{C_n(n_s+n_i)+C_p(p_s+p_i)} \tag{2.43}$$

Under conditions of high excitation where (Δn =Δp>>n_0 ,p_0), usually observed in organic BHJ solar cells even at relatively low illumination intensities, and assuming a deep localized energy level (E_{ts}=E_i) with (Δn >> n_i, p_i, as well as surface recombination centers at the electron selective electrode (the ZnO/active layer interface in our study). Consequently, Equation (2.43) can be reformulated accordingly. Equations (2.44-2.47) present the total concentration of charge carriers next to each interface between the active layer and the electrodes:

$$n_{S(C)} = \Delta n\ exp\left(\frac{q(V_{bi}-V_{OC})}{2\ kT}\right) \tag{2.44}$$

$$p_{S(C)} = \Delta n\ exp\left(-\ \frac{q(V_{bi}-V_{OC})}{2\ kT}\right) \tag{2.45}$$

$$n_{S(A)} = \Delta n\ exp\ \left(\frac{q(V_{bi}-V_{OC})}{2\ kT}\right) \tag{2.46}$$

$$p_{S(A)} = \Delta n\ exp\left(-\ \frac{q(V_{bi}-V_{OC})}{2\ kT}\right) \tag{2.47}$$

Taking into account the assumptions, equation (2.43) can be modified as follows for each of the interfaces:

$$u_{s(C)} = -\frac{C_p N_{ts}^{C}\Delta n}{exp\left(\frac{q(V_{bi}-V_{OC})}{2\ kT}\right)} \tag{2.48}$$

$$u_{s(A)} = -\frac{C_n N_{ts}^{A}\Delta n}{exp\left(\frac{q(V_{bi}-V_{OC})}{2\ kT}\right)} \tag{2.49}$$

$$C_n = \frac{q}{\varepsilon\varepsilon_0}\mu_n \qquad (2.50)$$

$$C_p = \frac{q}{\varepsilon\varepsilon_0}\mu_p \qquad (2.51)$$

In this context, Δn should be changed with n due to the consideration of a high degree of excitation. The following equations (2.52-2.53) are obtained by normalizing to the active layer thickness L in order to consider the presenting model in the scope of the total recombination losses:

$$U_{S(C)} = -\frac{u_{s(C)}}{L} = -\frac{q}{\varepsilon\varepsilon_0}\mu_p \ \frac{N_{ts}^{C} n}{L\ exp\left(\frac{q(V_{bi}-V_{OC})}{2\,kT}\right)} \qquad (2.52)$$

$$U_{S(A)} = -\frac{u_{s(A)}}{L} = -\frac{q}{\varepsilon\varepsilon_0}\mu_n \ \frac{N_{ts}^{A} n}{L\ exp\left(\frac{q(V_{bi}-V_{OC})}{2\,kT}\right)} \qquad (2.53)$$

The surface recombination rate can be further simplified by using the each charge carrier mobilities (μ_n, μ_p) with an effective mobility μ_{ef}. Various definitions have been utilized for effective mobility in the literature[94]. In this study, the effective charge carrier mobility is presented as $\mu_{eff} = \mu_n = \mu_p$, resulting in:

$$U_{s(C)} = -\frac{q}{\varepsilon\varepsilon_0}\mu_{eff} \ \frac{N_{ts}^{C} n}{L\ exp\left(\frac{q(V_{bi}-V_{OC})}{2\,kT}\right)} \qquad (2.54)$$

$$U_{s(A)} = -\frac{q}{\varepsilon\varepsilon_0}\mu_{eff} \ \frac{N_{ts}^{A} n}{L\ exp\left(\frac{q(V_{bi}-V_{OC})}{2\,kT}\right)} \qquad (2.55)$$

The open-circuit voltage (V_{OC}) can be replaced by the applied bias (V) to characterize the voltage-dependent recombination rate, which is influenced by the exponential decline of the surface recombination rate as forward bias decreases. Equation (2.56-2.57) establish the total net recombination losses in organic solar cells, including bimolecular, bulk, and surface trap-assisted recombination processes for an intrinsic active layer with one interface at either the cathode or anode electrode.

$$\frac{dn}{dt} = -\frac{q}{\varepsilon\varepsilon_0}\xi(\mu_{eff})n^2 - \frac{q\mu_{eff}N_t}{\varepsilon\varepsilon_0}n - \frac{q\mu_{eff}N_{ts}}{\varepsilon\varepsilon_0 L}exp\left[-\frac{q(V_{bi}-V_{cor})}{2kT}\right]n \quad (2.56) \quad \text{intrinsic}$$

$$\frac{dn}{dt} = -\frac{q}{\varepsilon\varepsilon_0}\xi(\mu_{eff})n^2 - \frac{q\mu_{eff}N_t}{\varepsilon\varepsilon_0}n - \frac{q\mu_{eff}N_{ts}}{\varepsilon\varepsilon_0 L}exp\left[-\frac{q(V_{bi}-V_{cor})}{kT}\right]n. \quad (2.57) \quad \text{doped}$$

A semi-empirical method is applied to obtain quantitative results on the recombination process by fitting the recombination current to the charge carrier density and the effective mobility of charge carrier obtained from impedance spectroscopy and the experimental recombination current measured using J-V measurements. This model considers bimolecular, bulk, and trap-assisted recombination processes [93,95,96]. The experimental recombination current is derived from the J-V characteristics, using J_{ph} (photocurrent density), J_l (current density under light), J_{dark} (current density in darkness), and $J_{ph,sat}$ (saturated photocurrent at -2 V).

$$J_{ph} = J_l - J_{dark} \tag{2.58}$$

$$J_{rec} = J_{ph,sat} - J_{ph} \tag{2.59}$$

The recombination current density is the superposition of bimolecular, bulk, and surface trap-assisted recombination's, as expressed in the following equation [93]:

$$J_{rec,sum} = J_{rec,bm} + J_{rec,bulk} + J_{rec,surf}. \tag{2.60}$$

The contribution of the bimolecular recombination current density to the total recombination current density can be expressed by the following equation:

$$J_{rec,bm} = \frac{q^2 L}{\varepsilon_0 \varepsilon_r} \xi (\mu_n + \mu_p) n^2, \tag{2.61}$$

where ξ represents the dimensionless Langevin prefactor, n denotes the charge carrier density, and μ_n and μ_p indicate the effective motilities of electrons and holes, respectively. Equation 2.62 denotes the contribution of bulk trap-assisted recombination, with N_{bt} representing the bulk trap density within the active layer.

$$J_{rec,bulk} = \frac{q^2 L}{\varepsilon_0 \varepsilon_r} \mu_n N_{bt} n. \tag{2.62}$$

The surface trap-assisted recombination current density for intrinsic and doped active layers are represented in two different equations, namely 2.63 for the doped and 2.64 for the intrinsic case, respectively:

$$J_{rec,surf,doped} = \frac{q^2}{\varepsilon_0 \varepsilon_r} \frac{\mu_p N_{st} n}{exp \frac{q(V_{bi} - V_{cor})}{kT}}, \tag{2.63}$$

$$J_{rec,surf,intrinsic} = \frac{q^2}{\varepsilon_0 \varepsilon_r} \frac{\mu_p N_{st} n}{exp \frac{q(V_{bi} - V_{cor})}{2\,kT}}. \tag{2.64}$$

2.4.3 Simulation part

To probe the contrast between intrinsic and doped active layers, a well-known NFA Y6 with donor PM6 was used as the active layer [97–100]. To simulate the dependence of open circuit voltage on light intensity considered the types of active layer as doped and intrinsic, the excition generation rate is determined. The transfer matrix method calculates the distribution of the optical field within the certain device configuration [101,102]. The code of TMM software is available for free [101,102]. It is known that extinction coefficient yields the ability of each layer to absorb the light with certain wavelengths. Since the device consists of multiple layers with different refraction and transmission properties, the proportion of reflected and transmitted light at every junction is influenced by the variation in the refractive index n(λ) of the surrounding layers. The device configuration in conjunction with refractive index and absorption coefficients measured experimentally served as input parameters presented in **Figures 2.12a and b.** Another functional layer's optical properties are obtained from literature[103–105]. The schematic illustration of the inverted device structure Glass/ITO/ZnO/PM6:Y6/MoOx/Ag is shown in **Figure 2.12b.** The generation rate as a function of wavelength and position inside the active layer G(x,λ) is simulated for the PM6:Y6 active layer and presented in a contour plot in **Figure 2.12c**. The wavelength-integrated generation rate in the active layer G(x), with x representing the distance from the anode, is illustrated in **Figure 2.12d**.

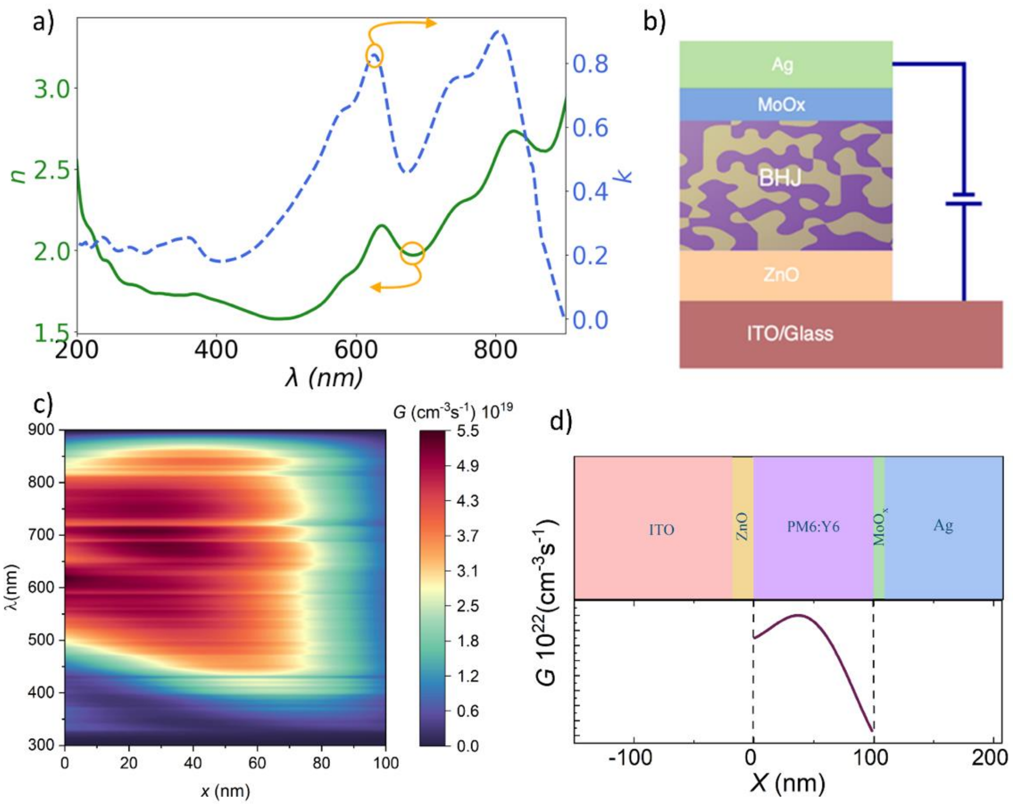

Figure 2.12. (a) Optical properties of PM6:Y6 blend and (b) inverted OSC architecture (c) Generation rate in 2D plot as a function of wavelength and thickness and d) Generation rate of the PM6:Y6 as a function of thikness within the device structure.

Table 2.1. Parameters of PM6:Y6 active layer.

Parameter	**PM6:Y6**
Energy Bandgap E	1.0 eV
Dielectric constant ε	3
Built-in voltage V_{bi}	0.9 V
Thickness L	100 nm
Effective mobility μ_{eff}	$5 \cdot 10^{-5}$ cm^{2}V^{-1}s^{-1}
Geminate recombination prefactor P_g	0.95
Effective density of states N_c	$2.5 \cdot 10^{19}$ cm^{-3}
Temperature T	298 K

To determine the dominant recombination mechanism using the V_{oc} vs. lnI method, the slope is expected to be the following: s = 1.0 kT/q for bimolecular recombination, s > 1.0 kT/q for bulk trap-assisted recombination, and s < 1.0 kT/q for surface trap-assisted recombination[97] [62,85,106]. **Table 1** provides the considered parameters of the PM6:Y6 active layer that was used to simulate the V_{oc} using the presented recombination model. In this example, we separated the V_{oc} vs. lnI analysis into two scenarios: first, considering surface trap-assisted in conjuction with bimolecular recombination, and second, considering the multi-mechanism recombination model that included surface trap-assisted, bulk, and bimolecular recombination.

The V_{oc} dependency on light intensity for intrinsic and doped active layers, including bulk trap-assisted recombination and without, shown in **Figure2.13 a and b**, respectively. The slope (s) as a function of the density of surface traps was calculated for doped and intrinsic, considering only surface and bimolecular recombination, and another case takes into account all three types of considered recombination as shown in **Figures 2.13c and d.** Considering only surface and bimolecular recombination, the slope of doped active layer is reduced with increasing surface trap density. The slope of intrinsic active layer remain constant with s = 1.0 kT/ q at the increasing surface trap density.

In the case of the second scenario, which considers all components of non-geminate recombination, the slope of the doped model yields a modest reduction within the density range of the surface trap 10^{10} - 10^{14} cm^{-2}, reaching 0.75 kT/q, indicating surface trap-assisted recombination dominance.The slope of the intrinsic active layer dropped smoothly compared to the doped active layer, reaching a slope of 1.0 kT/q. It remained the fixed in the range of surface trap density 10^{13} - $10^{14} cm^{-2}$. Based on the results of simulation, we can suggest inadvertent doping of the active layer when the measured slope of the intrinsic model is below 1.0 kT/q. Despite the presence of the intrinsic model, slopes exhibiting less than 1 kT/q may still result the improper energy level alignment at the imperfectly optimized electrodes; thus, it is crucial to acknowledge the necessity of optimized electrodes [107–110].

Figures 2.13e and f show the open circuit voltage as a function of density of surface trap for different value of reduction factor ξ= 1, 0.1, 0.01, 0.001 considered the intrinsic and doped models. The open circuit voltage of intrinsic model reduced rapidly when increasin the density of surface trap compared to doped model. The bulk trap-assisted recombination has no impact on open circuit voltage for both intrins and doped models.

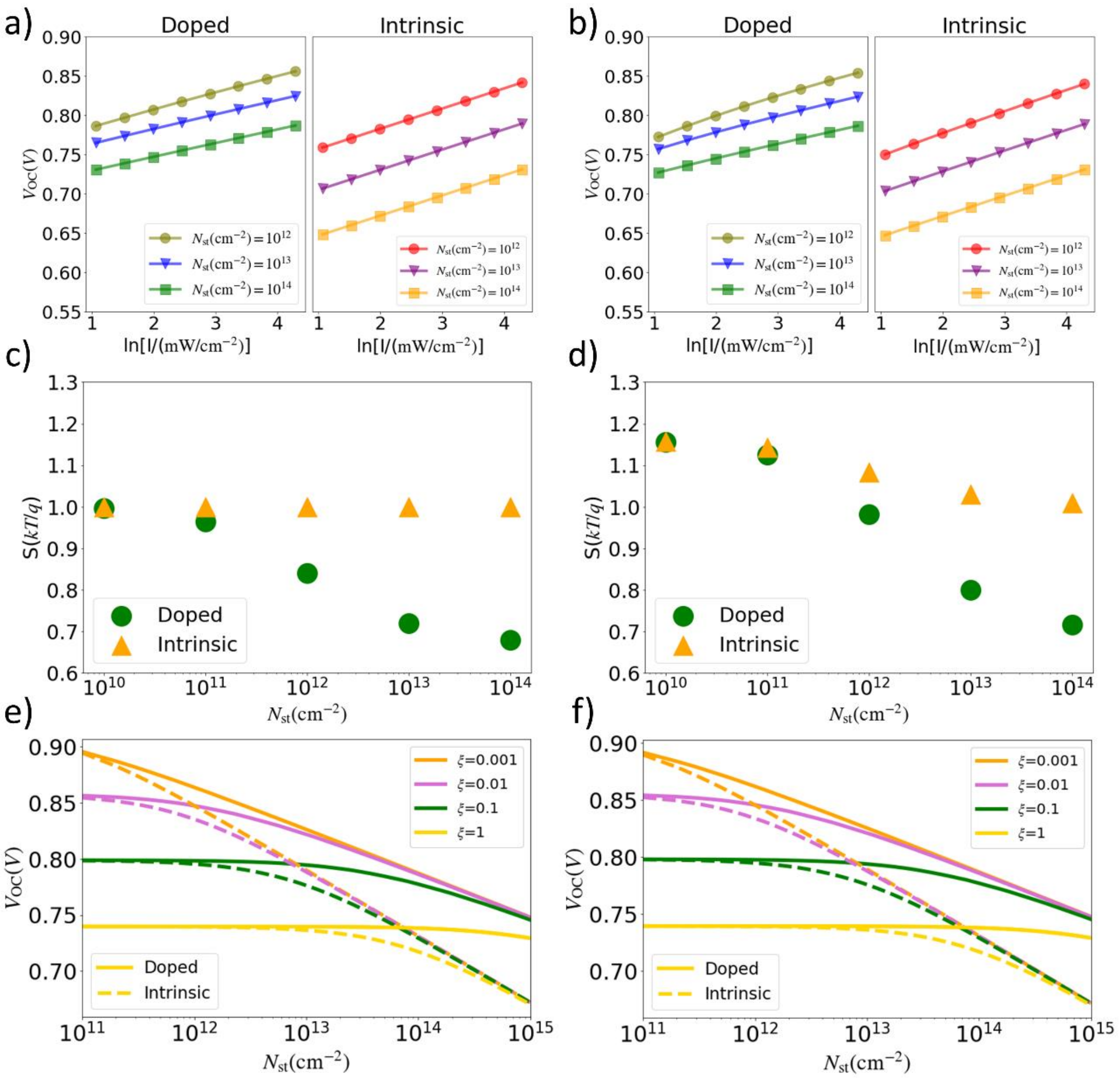

Figure 2.13. (a) and (b) Dependence of V_{OC} on the various light intensities at various concentration of surface. (c) and (d) Slope as a function of surface trap concentration. (e) and (f) Open circuit voltage (V_{OC}) in dependence of the density of surface traps N_{st} simulated at different values of the reduction factor ξ: 1, 0.1, 0.01, 0.001.

Additionally, we analyzed the slope dependent on the high-density surface traps for the intrinsic and doped models shown in **Figure 2.14**. The intrinsic model's slope showed a value of 1 kT/q at the extreme surface trap density 10^{15} to 10^{18} cm^{-2}, which was defined as a very high density of surface traps.

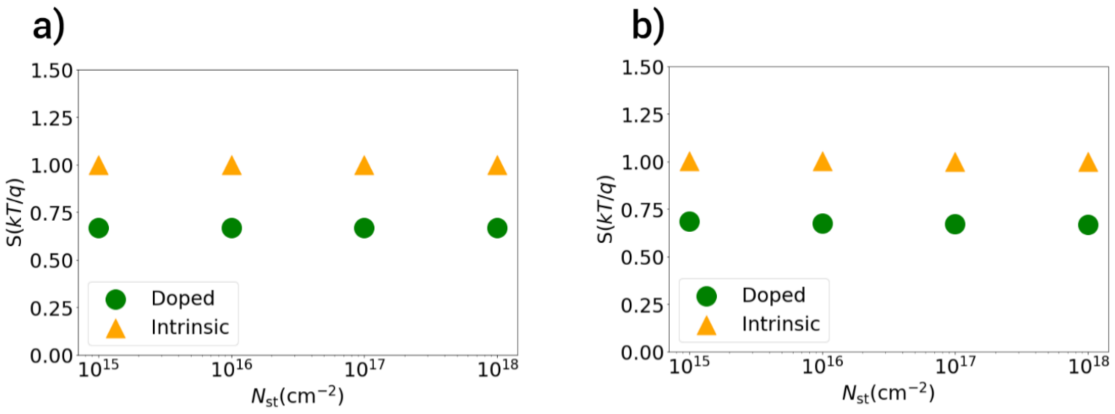

Figure 2.14 Slope as a function of the density of surface traps at the high values (a) without bulk traps and (b) with bulk traps.

2.4.4 Experimental part

To apply the models as intrinsic and doped, the devices with three different blends were fabricated. These examples contain devices using active layer of donor mixed with different donor COTIC-4F ITIC-4F O-IDTBR. **Figure 2.15** represents the chemical structure of the non-fullerene aceptors (ITIC4F, COTIC-4F, and O-IDTBR) and donor (PTB7-Th), device architecture of OSC and energy bangap scheme. Organic solar cells with different active layers were fabricated in the following : ITO/ZnO/BHJ/MoO_3/Ag .

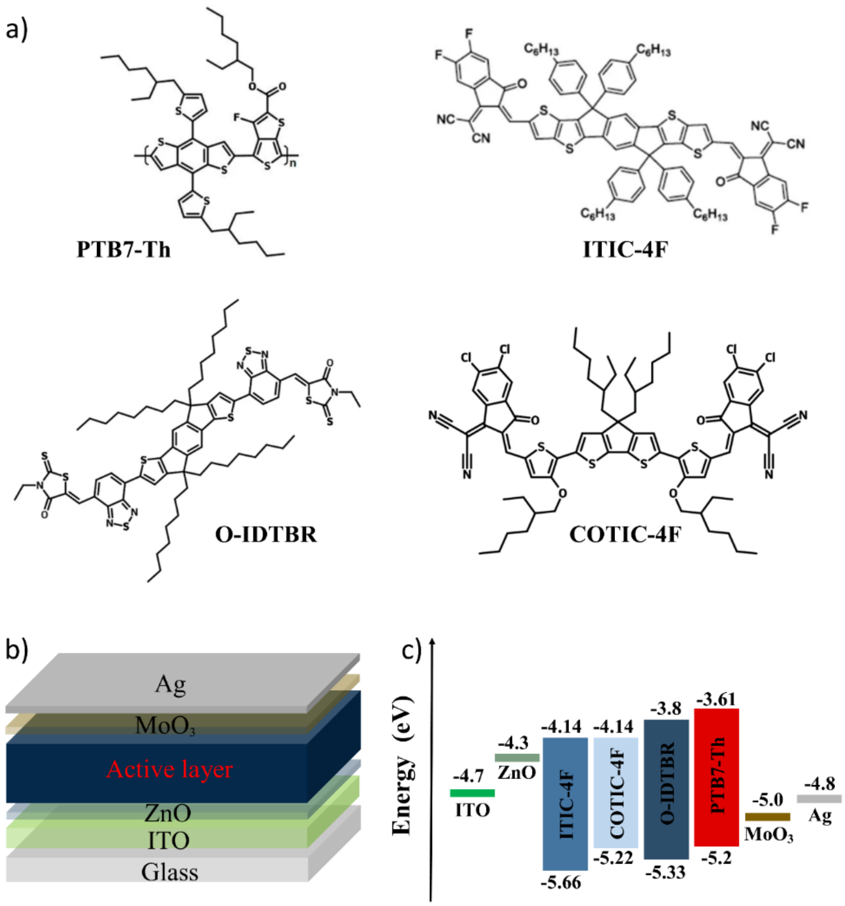

Figure 2.15 (a) Chemical structures of the non-fullerene acceptors O-IDTBR, and ITIC-4F, COTIC-4F, and the donor polymer PTB7-Th and. (b) Inverted device architecture, (c) Bandgap scheme illustrating the corresponding layers of the examined organic solar cells (OSCs).

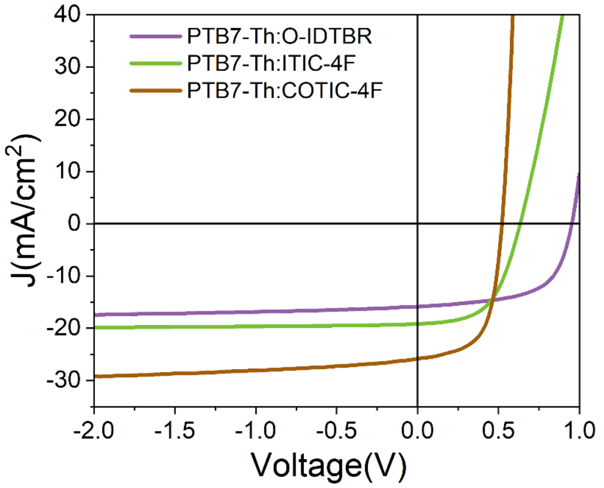

Figure 2.16 Current-Voltage measurements of the different OSCs under 1-sun.

Table 2.2 Photovoiltaic performance of OSCs under 1-sun.

D:A active layer	***FF* (%)**	**V_{OC} (*V*)**	**J_{SC} (mA/cm^2)**	***PCE* (%)**
PTB7-Th:COTIC-4F	57±1.9	0.54±0.007	25.37±0.79	7.76±0.3
PTB7-Th:O-IDTBR	61±1.19	0.95±0.006	16.07±0.36	9.21±0.13
PTB7-Th:ITIC-4F	55±2.1	0.64±0.01	18.79±0.58	6.48±0.23

The devices are fabricated with an identical transport layer and electrodes, using the donor material PTB7-Th with multiple acceptors with differing band gaps, including the small molecule O-IDTBR, the narrow energy band gap ITIC-4F, and the ultralow energy band gap COTIC-4F. The current density-voltage (J-V) characteristics of PTB7-Th using different acceptor devices are shown in **Figure 2.16**, and the statistical data is provided in **Table 2**, based on 10 devices. The inverted devices using PTB7-Th:O-IDTBR show a maximum power conversion efficiency (PCE) of 9.21%, due to a high open circuit voltage (V_{OC}) of 0.95, a short-circuit current density (J_{SC}) of 16.07 mA/cm², and a fill factor (FF) of 61%. Devices with a small acceptor band gap ITIC-4F exhibited significantly lower fill factor FF (55%) and open-circuit voltage (V_{OC}) at 0.64 V, resulting in a dropped average power conversion efficiency (PCE) of 6.48%. A notable decrease in open circuit voltage $V_{OC}$is detected when the ultralow bandgap acceptor COTIC-4F is used. The devices using COTIC-4F exhibited the lowest open circuit voltage (V_{OC}) of 0.54 V and the maximum short circuit current density (J_{SC}) of 25.37 mA/cm², resulting in a power conversion efficiency (PCE) of 7.76%.

The charge carrier recombination dynamic is investigated in this chapter. In order to determine the dominant recombination process in organic solar cells, we analyze how the V_{OC} value depends on the light intensity (V_{OC} versus ln[I]). The slopes of studied devices are shown in **Figure 2.17.**The devices with PTB7-Th:O-IDTBR and PTB7-Th:COTIC-4F blends have slope values larger than 1 kT/q, indicating that the dominant charge carrier recombination is Shockley-Read-Hall (SRH) recombination via deep trap states[96,110]. The slope of PTB7-Th:ITIC-4F blend devices is 1.09 kT/q, which is identified as bimolecular recombination loss.

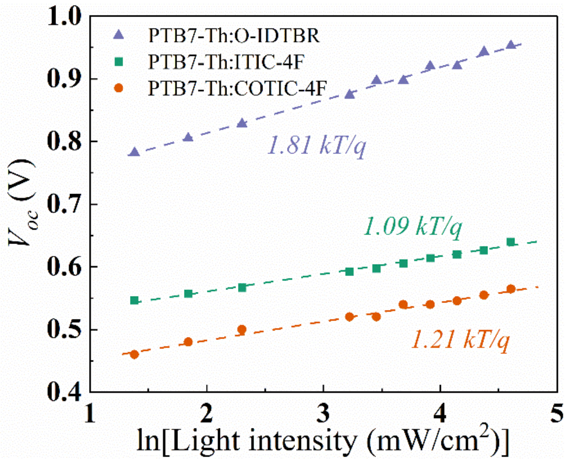

Figure 2.17 Open circuit voltage (V_{oc}) in dependence on of the light intensity of OSCs with different blends.

To investigate the recombination dynamic, the impedance spectroscopy in conjuction with J-V measurements were used. **Figure 2.18** demonstrates the concentration of charge carriers and effective mobility within the active layer as a function of applied voltage. The effective mobility of PTB7-Th:COTIC-4F blend showed lower value to one magnitude comparing to other blends. Related to charge carrier density, all three blend revealed the similar charge carrier density along the applied voltage.

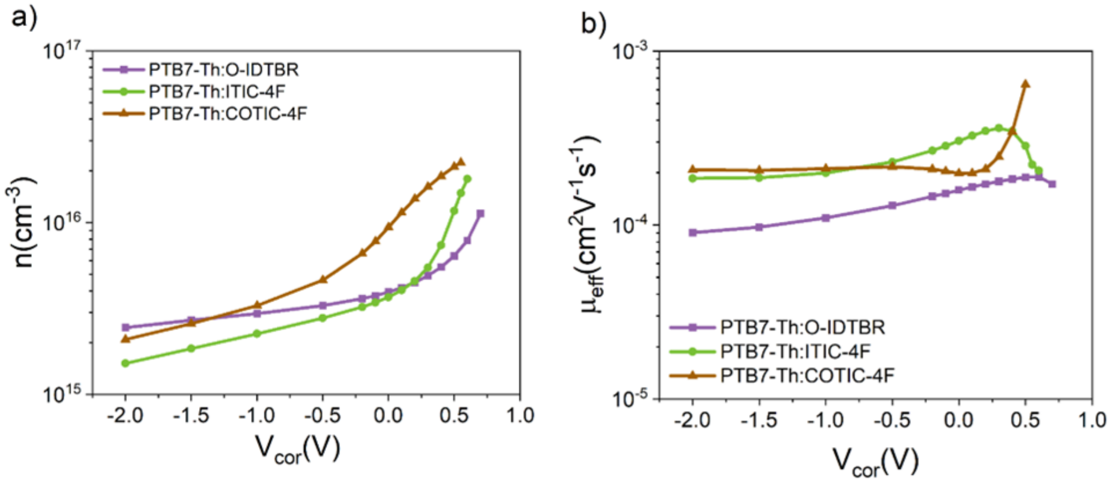

Figure 2.18 (a) Concentration of charge carrier and (b) effective mobility of OSCs with blends:PTB7-Th:O-IDTBR, PTB7-Th:ITIC-4F, and PTB7-Th:COTIC-4F.

The multi-mechanism recombination model was then used to fit the measured recombination current density ($J_{rec,exp}$) for intrinsic and doped models under 1-sun. **Figure 2.18** demonstrates the current density (*J*) dependence on applied bias fitted with the results of the simulated current density. The recombination characteristic variables as ξ, N_{bt}, and N_{st} were used to correctly fit the measured $J_{rec,exp}$ with the simulated recombination current ($J_{rec,sum}$).

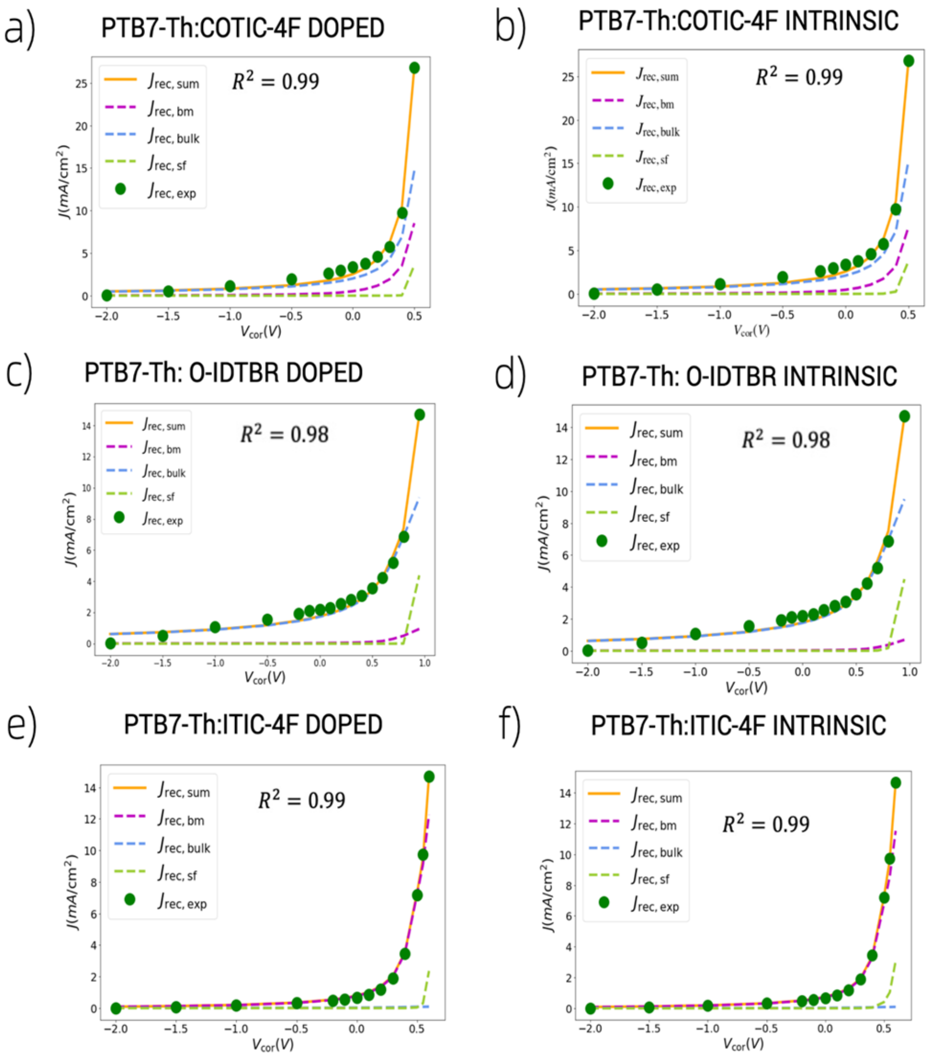

Figure 2.19 Fitting the simulated recombination current densities with experimentally measured.

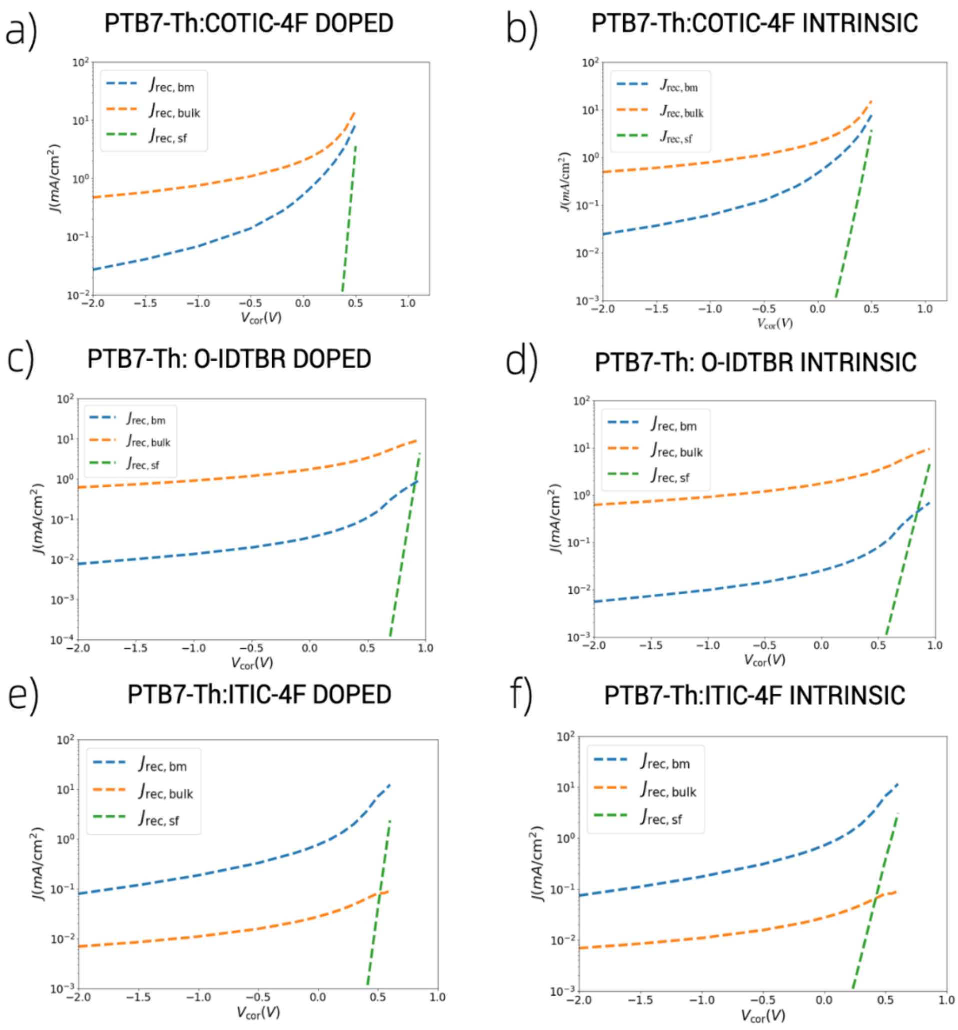

Figure 2.20 The quantity components of the recombination current density .

The reduction factor in the blend with donor PTB7-Th and acceptor ITIC-4F for intrinsic and doped models, derived from the fitting of recombination current, yields a superior value of reduction factor of $\xi = 0.06$ compared to other active layers $\xi = 0.0082$ and $\xi = 0.01$, as depicted in **Figure 2.21a**. Bimolecular recombination losses can be responsible for the moderate fill factor (FF) of 55 % with acceptor ITIC-4F, in comparison with acceptors O-IDTBR with FF of 61 % and COTIC-4F with FF of 57 % which exhibit lower reduction factors of $\xi = 0.0082$ and $\xi = 0.01$, respectively, resulting in reduced bimolecular recombination losses[77,111,112]. The study of the bimolecular recombination for all blends reveals an insignificant distinction between the considered cases:doped and intrinsic models.

The N_{bt} of considered active layers remained unchanged in the cases as intrinsic and doped active layers (see **Figure2.21b**). Different blends with intrinsic and doped active layers differ mainly in the density of surface traps. Surface trap concentrations are significantly higher in the doped active layer cases in all considered active layers than in the intrinsic active layer model (see **Figure2.21c**).

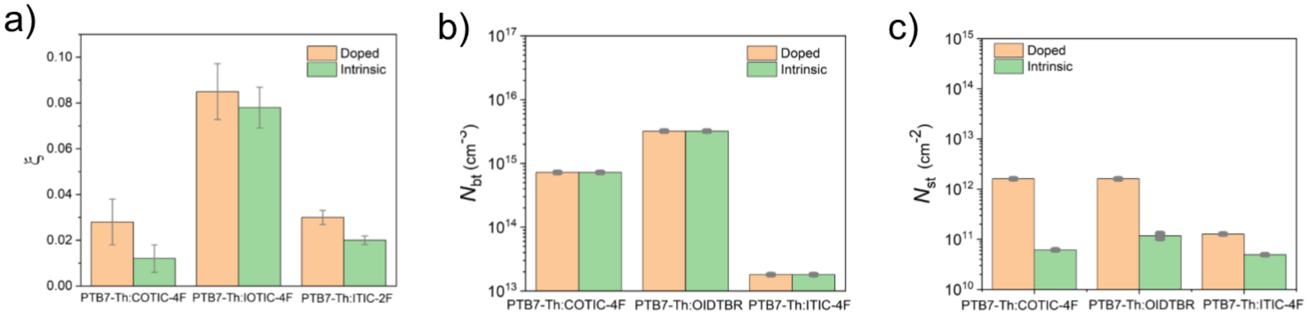

Figure 2.21 The identified recombination parameters (a) the reduction factor (ξ), (b) bulk trap density N_{bt}, and (c) surface trap density N_{st} .

2.4.5 Conclusion

The extended multi-mechanism recombination model to quantify surface recombination dynamics in the intrinsic and doped active layer was used to simulate one of the key parameter V_{OC} in dependence of light illumination. The slope, which is based on V_{OC} dependence on natural logarimph light illumination, presented as the function of surface trap concentration. Interestingly, surface trap–assisted recombination impact insignificantly based on the simulation of the intrinsic active layer's slope from the widely investigated V_{OC} vs. lnI plots. In contrast, doped active layer is influenced hugely by surface trap-assisted recombination showing the different impact on the V_{OC} then the intrinsic active layer. Importantly, those findings conclude unintentional doping of the active layer if the slope of intrinsic active layer achives value less than 1kT/q yet it works at the extreme values of the surface trap density. Based on the impedance spectroscopy measurements of OSC with different active layer, doped active layer possess significantly higher surface trap density compared to intrinsic. Our results demonstrate the essential importance of correctly characterizing and understanding recombination losses contributed by surface traps.

2.4.6 Experimental section

Device Fabrication

The organic devices were fabricated using the inverted device structure: ITO/ZnO/BHJ/MoO_3/Ag. The ITO-coated glass substrates were successively cleaned by ultrasonication with detergent, acetone, and isopropyl alcohol for 15 minutes. A zinc oxide solution was prepared by mixing diethyl zinc and THF in a 1:2 (v/v) ratio. Then, the ZnO film was deposited using a spin-coating technique at 4000 rpm for 15 seconds and annealed at 150 °C for 30 minutes. The blend solutions (20 mg/mL) of PTB7-Th:ITIC-4F (1:1.5 ratio, in CB with 1 vol% DIO), PTB7-Th:COTIC-4F (1:1.5 ratio, in CB with 2 vol% CN) and PTB7-Th:O-IDTBR (1:2 ratio, in CB with 2 vol% CN) were deposited under inert N_2 atmosphere by spin-coating at 2000 rpm. The top electrode was then deposited by thermal evaporation of molybdenum (VI) oxide and silver. The device's active area was 0.1 cm^2.

Characterization

J-V curves were recorded with a Semiconductor Device Analyzer (B1500A, Keysight) paired with an Oriel 3A solar simulator, operating at an intensity of 100 mW/cm^2. Impedande measurements were carried out using an impedance analyzer (SI1260, Solartron).

2.5 Impedance Spectroscopy

Impedance spectroscopy is a nondestructive technique utilized to determine the physical and chemical characteristics of materials, interfaces, and multijunction devices, dependent on applied voltage, light and temperature. In an impedance measurement, the device's response to a time-varying electric field is detected, measuring the ratio of electrical energy stored to that dissipated by the sample, with the relaxation time scale as a function of frequency[113]. In impedance spectroscopy, the input signal is an alternating voltage (V_{AC}). The mechanisms of V_{AC} and relaxation processes, including lattice distortions, electrode polarization, dipole rearrangement, electrical and ionic conduction, are progressively studied by altering the frequency of V_{AC} and monitoring the alternating current response I_{AC}[113]. To study the resistive and capacitive properties of solid-state devices, the impedance spectra measurements are performed in the frequency range from subhertz to megahertz. Impedance spectroscopy is beneficial for analyzing electrical and ionic conduction, as well as "slow" (microseconds to seconds) charge transfer behaviors at material surfaces[113].

In this thesis, impedance spectroscopy is used to examine the electrical process specifically quantitatively defines the extracted charge carrier density in solar cells, providing insight into non-geminate recombination loss[88]. The equivalent circuit enables the analysis of the impedance response of multilayer devices by characterizing it through a combination of ideal capacitors, resistors, inductors, and non-ideal components. An equivalent circuit scheme used for investigation of organic solar cells is presented in **Figure 2.11**[88–90].This circuit consist of an ideal diode, chemical and geometrical capacitance, a shunt resistance R_{sh}, and a source of photo-generated charge carriers J_{ph} in parallel as well as a series resistance R_s. A recombination resistances connected parallel to the shunt resistance which takes into account different recombination processes as bimolecular, bulk trap-assisted and surface trap-assisted as shown in the circuit scheme in **Figure 2.11**. Additionally, the circuit has element called inductance describing the parasitic inductance originated from connections in the device [91].

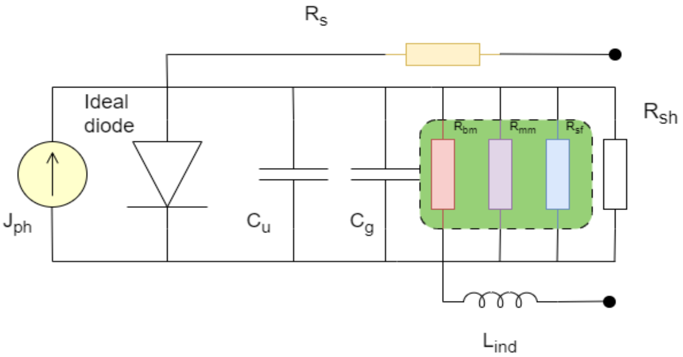

Figure 2.22 Equivalent circuit scheme with non-geminate recombination resistance.

2.5.1 Theory of Impedance Spectroscopy

The impedance spectroscopy measures the transient current under electrical or optical perturbation. Technically, a small-amplitude perturbations in form of a AC-voltage V_{AC} at various applied biases V_{DC} are applied to the device under dark and light illumination. Firstly, a sinusoidal voltage is applied to the solar cells [91] :

$$V(t) = V_0 cos(\omega t) \tag{2.65}$$

generating a response current,

$$I(t) = I_0 cos(\omega t - \varphi) \tag{2.66}$$

where V_0 and I_0 are the voltage and current amplitudes, ω is the angular frequency, and ω is the phase shift between the voltage and current signals.

A complex resistance, known as impedance, is defined in frequency-dependent ratio of the voltage and current using Euler's transformation [91]:

$$Z = \frac{V_0}{I_0} e^{i\varphi} = Z_0 cos\varphi + iZ_0 sin\varphi = Z' + iZ'' \tag{2.67}$$

where Z_0 is the impedance amplitude and Z' and Z'' are the resistance (active part) and reactance (imaginary part) of the circuit.

Nyquist plot shows the relationship of the imaginary and active parts of the impedance as shown in Figure 2.12. Each point on the Nyquist plot of an ideal parallel linked R-C circuit corresponds to a certain frequency; the plot's fashion is a semicircle [91].

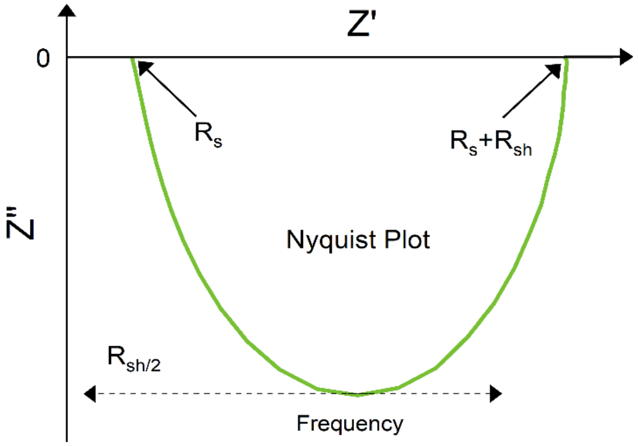

Figure 2.23 Example of Nyquist plot of OSC.

The method below allows one to distinguish the capacitance contribution from the active layer, transport layer, and electrodes, thereby probing the charge carrier density in solar cells. The transformation method from capacitance to charge carrier necessitates consideration of operating conditions, certain assumptions, and necessary corrections, which we will discuss below. We measure the devices' impedance under both dark and illuminated conditions, varying the frequency and bias accordingly. The applied bias as an input voltage to the device are started from approximately -3 V or -2 V and reach the open circuit voltage (V_{OC}). Additional correction to the capacitance must be taken into account including the effect of series resistance and parasitic inductance in the circuit. Impedance, inductance, and series resistance are used to determine the corrected capacitance presented in the equation 2.23 [91]:

$$C_\mu = -\frac{1}{\omega}\frac{Z'' - \omega L_{ind}}{(Z' - R_s)^2 + (Z'' - \omega L_{ind})^2} \tag{2.68}$$

The series resistance is influential parameters specifically in the considered range of frequency while the inductance is accounted for the parasitic inductance of the connecting cables.

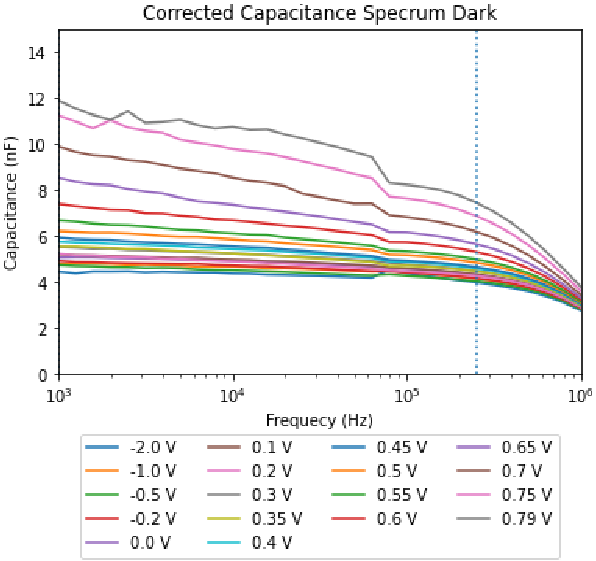

Figure 2.24 The corrected capacitance of OSC under dark condition at different bias from -2 V to 0.79 V.

The corrected capacitance of organic solar cells can be classified as either frequency-dependent or frequency-independent. The chemical capacitance in frequency-dependent conditions is generated from free charge carriers. The frequency-independent capacitance is derived from the Maxwell displacement current, which can be classified as either voltage-independent, referred to as geometrical capacitance, or voltage-dependent, determined by the capacitance of a space charge area[95].

$$C_{cor} = C_{in} + C_M \tag{2.69}$$

$$C_{in} = qAL\frac{dn}{dV_{cor}} \infty G \tag{2.70}$$

$$C_M = \frac{\varepsilon\varepsilon_0 A}{W} = A\sqrt{\frac{\varepsilon\varepsilon_0 qN}{2(V_{bi} - V_{cor}}} \tag{2.71}$$

The geometrical capacitance consist of characteristics of device as thickness, area and dielectric constant of active layer as shown in equation [114] :

$$C_g = \frac{\varepsilon_r\varepsilon_0 A}{L} \tag{2.72}$$

here ε_0 is the vacuum permittivity and ε_r is the dielectric constant of the active layer.

To date the charge carrier density, one should consider the total charge carrier consisting of the voltage independent from saturated capacitance (Equation 2.28) and voltage dependent defined from chemical capacitance (equation) [115].

$$C_{sat} = C_{light} - C_{\ g} \tag{2.73}$$

$$C_\mu(V_{cor}) = C_{light}(V_{cor}) - C_{\ g} \tag{2.74}$$

The total charge carrier density equation is presented in the next equation:

$$n_{tot}(V) = n_{sat} + n_{exc}(V) \tag{2.75}$$

$$n_{exc}(V_{cor}) = \frac{1}{qAL}\int_{V_{sat}}^{V_{OC}} C_\mu dV_{cor} \tag{2.76}$$

The boundary conditions of chemical capacitance should be identified correctly. The upper boundary condition is the open circuit voltage under the conditions with the highest background illumination. The lower boundary condition is measured at the reverse bias and can be referred to as saturation voltage. Due to series resistance the applied voltage is undergo to the loss and the correction is made as $V_{cor} = V_{DC} - JR_s$.

The next part of charge carrier is obtained from voltage independent capacitance which is saturated capacitance calculated from the difference under dark and light mode of the saturated voltage.

$$C_{sat} = C_{light}(V_{sat}) - C_{dark}(V_{sat}) \tag{2.77}$$

The result integration of the saturated charge carrier density is presented in equation:

$$n_{sat} = \frac{C_{sat}}{qAL} \times (V_0 - V_{sat}) \tag{2.78}$$

where V_0 - the built in voltage.

The effective mobility is calculated using the charge carrier density and current density in the following formula[114]:

$$\mu_{eff} = \frac{J(V_{cor})\, d}{2qn(V_{cor})[V_{cor} - V_{oc}]} \tag{2.79}$$

where d- thickness of the active layer and q is the elementary charge carrier, $J(V_{cor})$- the measured current density in dependence of the corrected voltage. The parameters as charge carrier density and the effective mobility allow to calculate the recombination currents associated with bimolecular, trap-assisted including surface and bulk traps.

2.6 Proton Accelerator

2.6.1 INURA pulsed high-current proton/electron accelerator

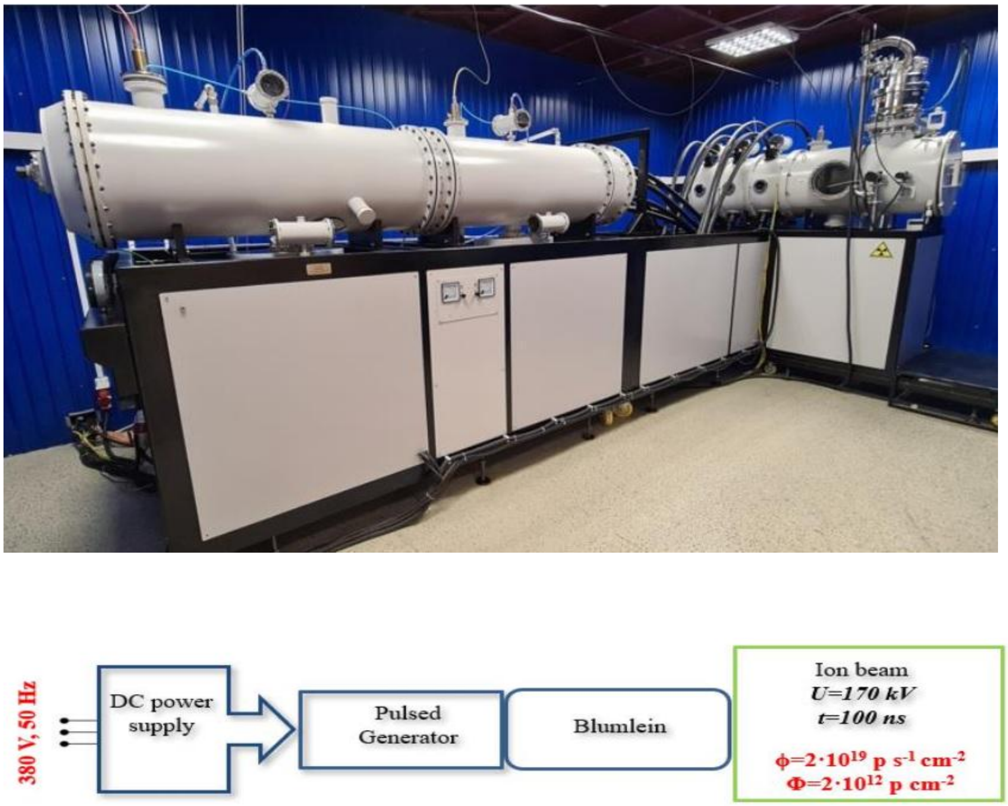

Figure 2.25 INURA pulsed high-current proton/electron accelerator

The i-NURA (Nazarbayev University's Research Accelerator) pulsed high-current proton/electron accelerator includes a high-voltage pulse generator and the diode system of the accelerator. A diode is exposed to a high-voltage impulse that endures for 100 nanoseconds and with a rate of over 10^{12} volts per second. Afterwards, the anode's surface generates the discharge plasma, and the acceleration of the proton beam proceeds by a single voltage impulse. In order to expose the device to radiation, it is positioned on a rotating table inside a vacuum chamber. The distance between the device and the diode is 35 cm. The vacuum chamber then presses it down to a pressure of 5×10^2 mTorr. Before irradiating the device, a collimated Faraday cup with a magnetic cutoff is used to calibrate the proton beam[116].

2.6.2 Electron accelerator

The electron linear accelerator ILU-10 at the Institute of Nuclear Physics in Almaty, Kazakhstan, was used to irradiate samples with an electron energy of 5 MeV, delivering a total fluence of 7×10^{13} e/cm². The absorbed doses of high-energy electrons were measured using GEZ B6001 polystyrene calorimeters and GEX B3002 film dosimeters.

2.6.3 SRIM/TRIM software package

The software program SRIM (Stopping and Range of Ions in Matter) is frequently used to simulate how ions interact with matter. The SRIM/TRIM package's objective is to calculate the amount of energy that is lost when a beam of particles passes through a material or becomes trapped into a substance of a specific thickness. For the purpose of simulation, the input parameters, which include the properties of the target and the ions, especially the energy of the ions, the thickness of the target, and its density, should be provided. The simulation results show the ion distribution in the material together with other properties like sputtering rate, ionization, penetration depth, vacancy concentration, and so on.

One of the applications of the SRIM/TRIM package is the research and technology in the radiation sector that pertains to radiation materials. In Chapters 3 and 4, the simulation of energy loss in organic solar cells was carried out with the assistance of the SRIM/TRIM package's capabilities [117].

Chapter 3 Thin vs Thick :Active Layer thickness role in organic solar cell resillence to proton irradiation

3.1 Introduction

Improvements in material processing techniques have revolutionized the photovoltaic performance of organic solar cells due to their tunable bandgap and cost-effective solution-based fabrication. There exists a growing interest in harnessing solar energy from high-efficiency organic solar cells to power future space infrastructure, including the increasing number of small satellites and potential space missions The space environment presents an individual mix of extreme conditions, including solar ultraviolet radiation, high vacuum, irradiation and temperature cycling. Learning about potential degradation under these extremes is essential to maintain and enhance the stability of space solar cells. The results of low energy proton irradiation of organic solar cells conclude the moderate decrease of photovoiltaic performance. Under proton irradiation with fluence ranging from 10^{12} to 10^{15} p cm², organic photovoltaic systems using the absorber layer PTB7-Th:PC71BM demonstrate superior performance compared to solar cells with a GaAs absorber layer[118]. A close study of how ionizing radiation affects organic materials shows that it breaks down the bounds between atoms because it transfers kinetic energy. Due to their low energy, covalent bonds are prone to breaking easily. For organic semiconductors, the release of H atoms causes the formation of localized defect states in the bandgap that act as recombination centers[119]. Furthermore, the self-healing effect of organic solar cells with PCE10:ITIC-4F blend was previously unknown, but was discovered in a freshly performed work using the fluence $2*10^{12}$ proton irradiation[120]. However, one of the key elements in the operational functionality of solar cells is how device physics characteristics are affected by extreme environmental conditions of space. This study dedicated to the understanding how organic solar cells perform under intense low-energy proton irradiation, focusing particular attention to parameters as active layer thickness and device physics characteristics as generation, recombination, and extraction. Furthermore, the post-annealing treatment was employed on the irradiated device to study the effect of recovery of recombination centers.

3.2. Results and Discussion

3.2.1 Device Physics

Here, we study the most promising blend with the highest PCE achieved so far and it includes Poly[[4,8-bis[5-(2-ethylhexyl)-4-fluoro-2-thienyl]benzo[1,2-b:4,5-b']dithiophene-2,6-diyl]-2,5-thiophenediyl[5,7-bis(2-ethylhexyl)-4,8-dioxo-4H,8H-benzo[1,2-c:4,5-c']dithiophene-1,3-diyl]-2,5-thiophenediyl] **(PM6)** as a polymer donor and 2,2'-((2Z,2'Z)-((12,13-bis(2-ethylhexyl)-3,9-diundecyl-12,13-dihydro-[1,2,5]thiadiazolo[3,4-e]thieno[2",3'':4',5']thieno[2',3':4,5]pyrrolo[3,2-g]thieno[2',3':4,5]thieno[3,2-b]indole-2,10-diyl)bis(methanylylidene))bis(5,6-difluoro-3-oxo-2,3-dihydro-1H-indene-2,1-diylidene))dimalononitrile **(Y6)** as an electron acceptor.

In order to investigate the influence of proton irradiation on the device characteristics, the inverted device structure of ITO/ZnO/PM6:Y6/MoOx/Ag with certain energy levels of functional layers were utilized as shown in **Figure 3.1 a and b**. The inverted OSCs with PM6:Y6 system were fabricated at varying thickness as 60 nm and 100 nm with the solvent additive 0.5 % CN , 260 and 400 nm thickness with the solvent additive 1.5 % CN. By increasing the amount of the solvent additive (chloronaphthalene (CN)) in the thick PM6:Y6 blend, the packing and crystallinity of the donor and acceptor components in the blend are modified, resulting in improved fill factor parameters of the organic solar cell that are equivalent to those of thin OSC [77].

The protons, carrying an energy of 170 keV, interact with the structure of the device with different thickness of PM6:Y6 namely 60, 100, 260, and 400 nm. The INURA accelerator's parameters used for proton irradiation are shown in **Figure SI3** which includes the function of accelerating voltage (170 keV) and beam current ($2A/cm^2$) on time. The proton beam fluence is in the range 1-$1.3 \cdot 10^{12}\ p\ cm^2$. The proton irradiation was applied to the rear side, namely Ag electrode and collisions occur in all functional layers of solar cells. **Figure 3.1d** presents the energy loss of protons in PM6:Y6 blend is 0.01 eV/Å-Ion and the highest value of energy loss taking place in ITO is 0.04 eV/Å-Ion.

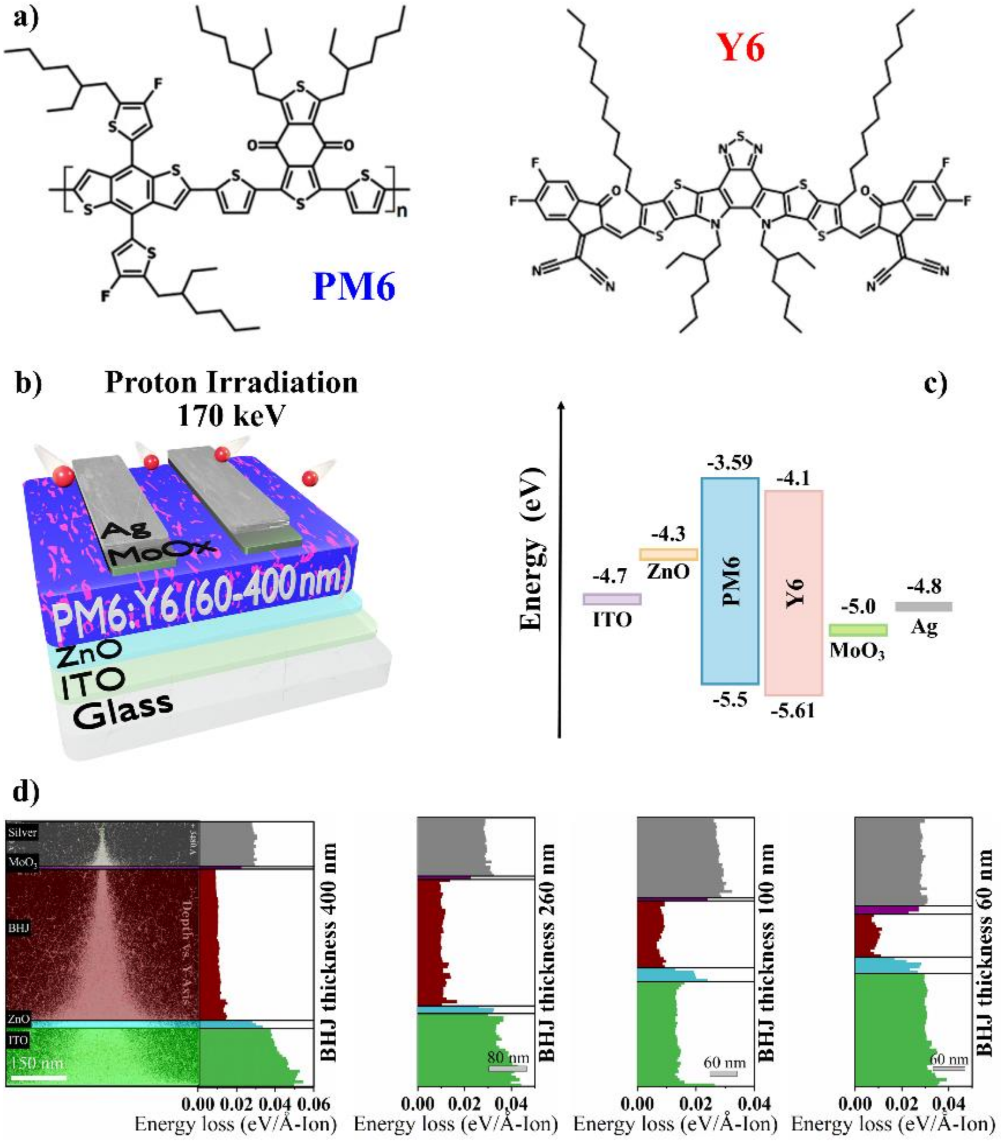

Figure 3.1 a) Chemical structure of organic solar cell b) Irradiation mechanism of solar cells from rear side (Ag electrode) c) energy level of functional layers d) Energy loss calculation in functional layers.

3.2.2 PM6:Y6 Bulk-Heterojunction Layer

This section focuses on analyzing the material properties of a PM6:Y6 blend deposited on glass with different thicknesses (60, 100, 260, and 400 nm) in order to investigate optical, surface roughness and morphological properties. Next, the PM6:Y6 were exposed to proton irradiation and post-annealing treatments. Optical properties of PM6:Y6 blend deposited on glass, transmission and reflectance are measured by UV-vis spectroscopy and shown in **Figure 3.2-3.3**. Reflection of PM6:Y6 thin film exhibits similar values of PM6:Y6 thin films at different thickness identifying the reflection peaks at 640 and 880 nm corresponding to PM6 and Y6[121] .The reflectance measurements show consistent results for all thicknesses, with no significant changes after irradiation and post-annealing. Transmission of PM6:Y6 blend thin films is dependent on the thickness of the blend. As it can be seen in **Figure 3.3** that PM6:Y6 blend with thickness of 60 nm show higher transmission of 56% at 435 nm wavelength. At the same wavelength, active layer with 400 nm thickness shows transmission of 12.5 %. Proton irradiation of PM6:Y6 thin film does not affect its optical characteristics, a similar finding was observed when protons with 30 keV energy irradiated PM6:Y6 [122].To determine the influence of proton irradiation and post-annealing on the surface topography of the PM6:Y6 system as presented in **Figure 3.4**, atomic force microscopy (AFM) was employed to image the height scan and calculate a root-mean-square (RMS). A uniform and smooth surface was detected in 100 nm thickness of PM6:Y6 showing RMS value 0.86 nm, 0.88 nm and 0.88 nm for as-prepared, irradiated and post-annealed, respectively. However, the surface roughness parameter (RMS) for thick (400 nm) thin film exhibits a slight decrease after proton irradiation from 7.1 nm to 5.4 nm. Due to a relatively high surface roughness of 400 nm as-prepared thick films, proton irradiation heats up the surface, therefore the roughness of the thick film’s surface smooths the surface. To investigate the morphology features of PM6:Y6 thin film, the Transmission Electron Microscopy was used and the images are displayed in **Figure 3.5**. The PM6:Y6 thin film with 100 nm thickness exhibits an advantageous interpenetration of D-A nano-fibrous and homogeneous morphology compared to other thicknesses such as 60, 260 and 400 nm. In the case of 400 nm thickness, the adverse interpenetration of D-A phase and larger course phase-separated grains are observed. TEM images of thin and thick films are dissimilar because the thick films increase the elastic scattering due to fixed the mean-free path[123] . Therefore, we observe similar morphology of thin film with thickness 60,100 and 260 nm but the morphology of 400 nm shows a strong contrast of dark and bright area because of the mass-thickness effect. Moreover, there is no change in morphology observed after proton irradiation and post-annealing.

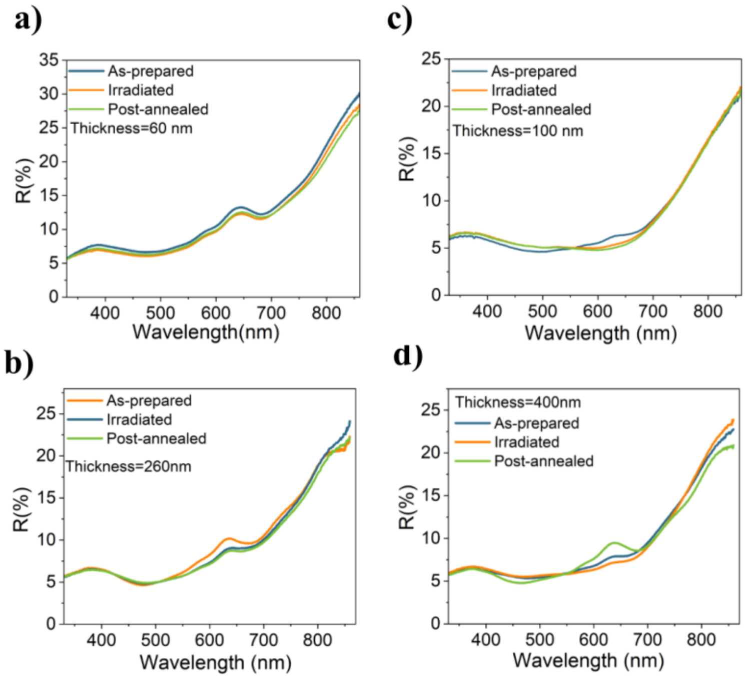

Figure 3.2 Reflectance of PM6:Y6 thin film with thickness a) 60 nm b) 100 nm c) 260 nm d) 400 nm

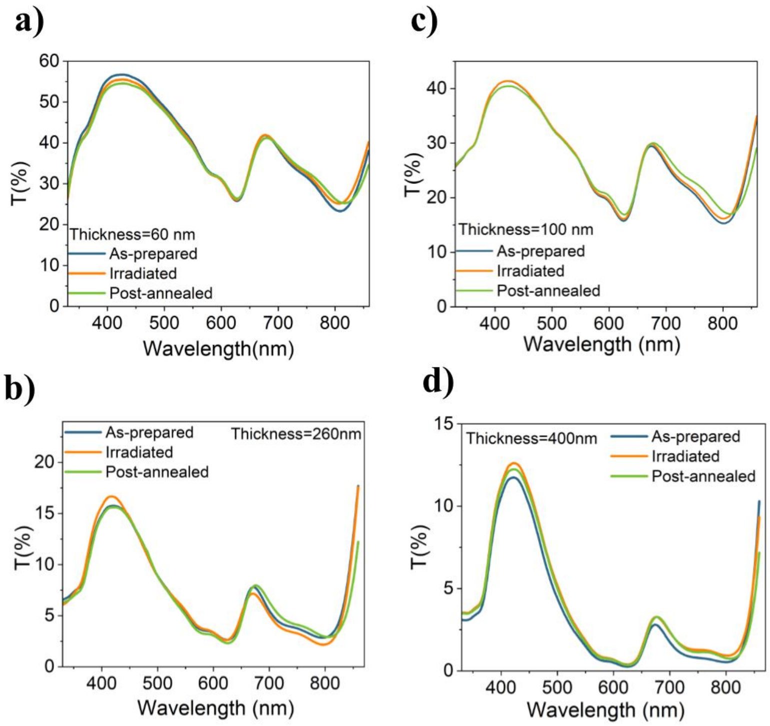

Figure 3.3 Transmittance of PM6:Y6 thin film with thickness a) 60 nm b) 100 nm c) 260 nm d) 400 nm.

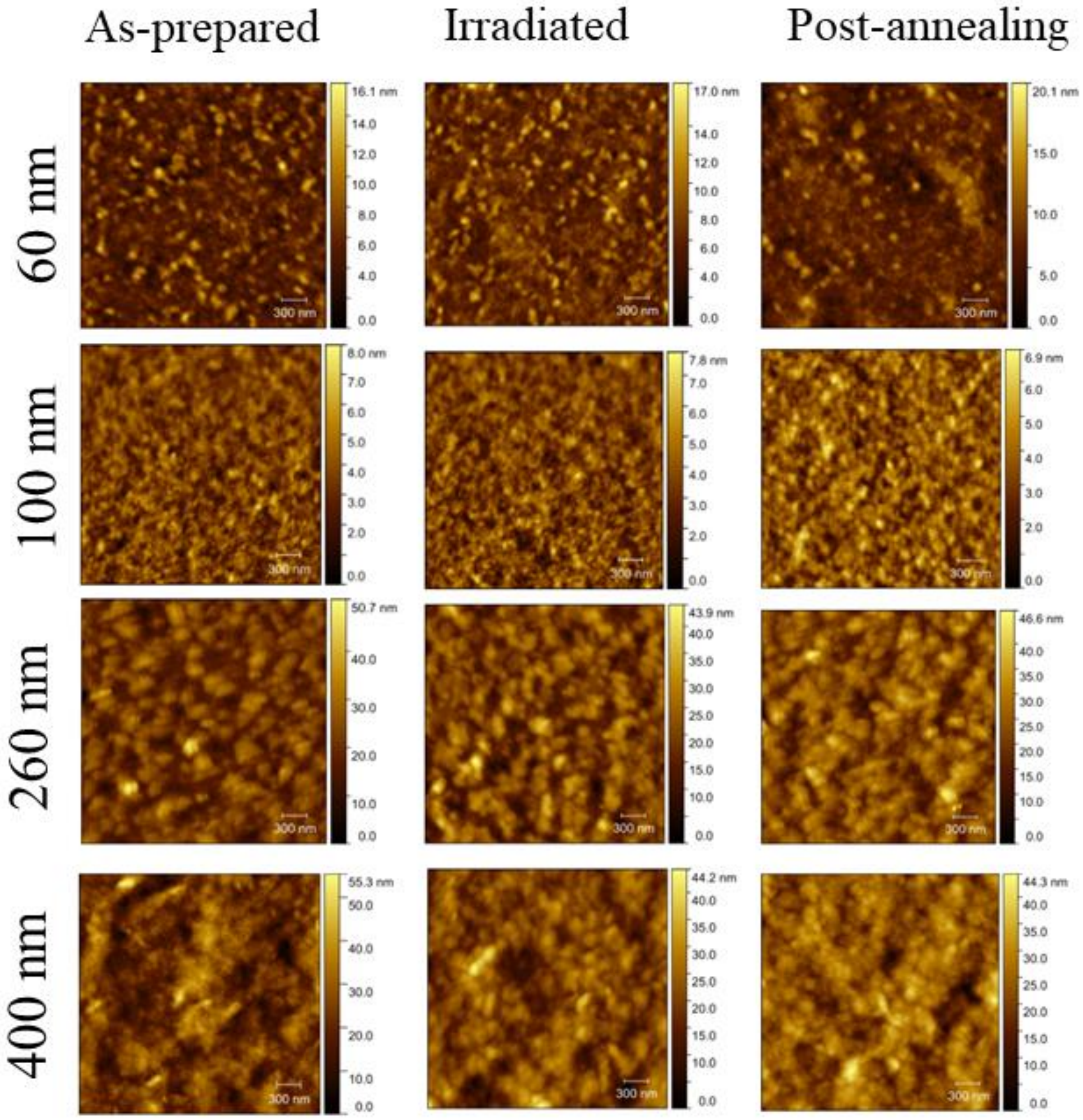

Figure 3.4 $3\mu m$ x $3\mu m$ AFM (Atomic Force Microscope) height images of PM6:Y6 blend.

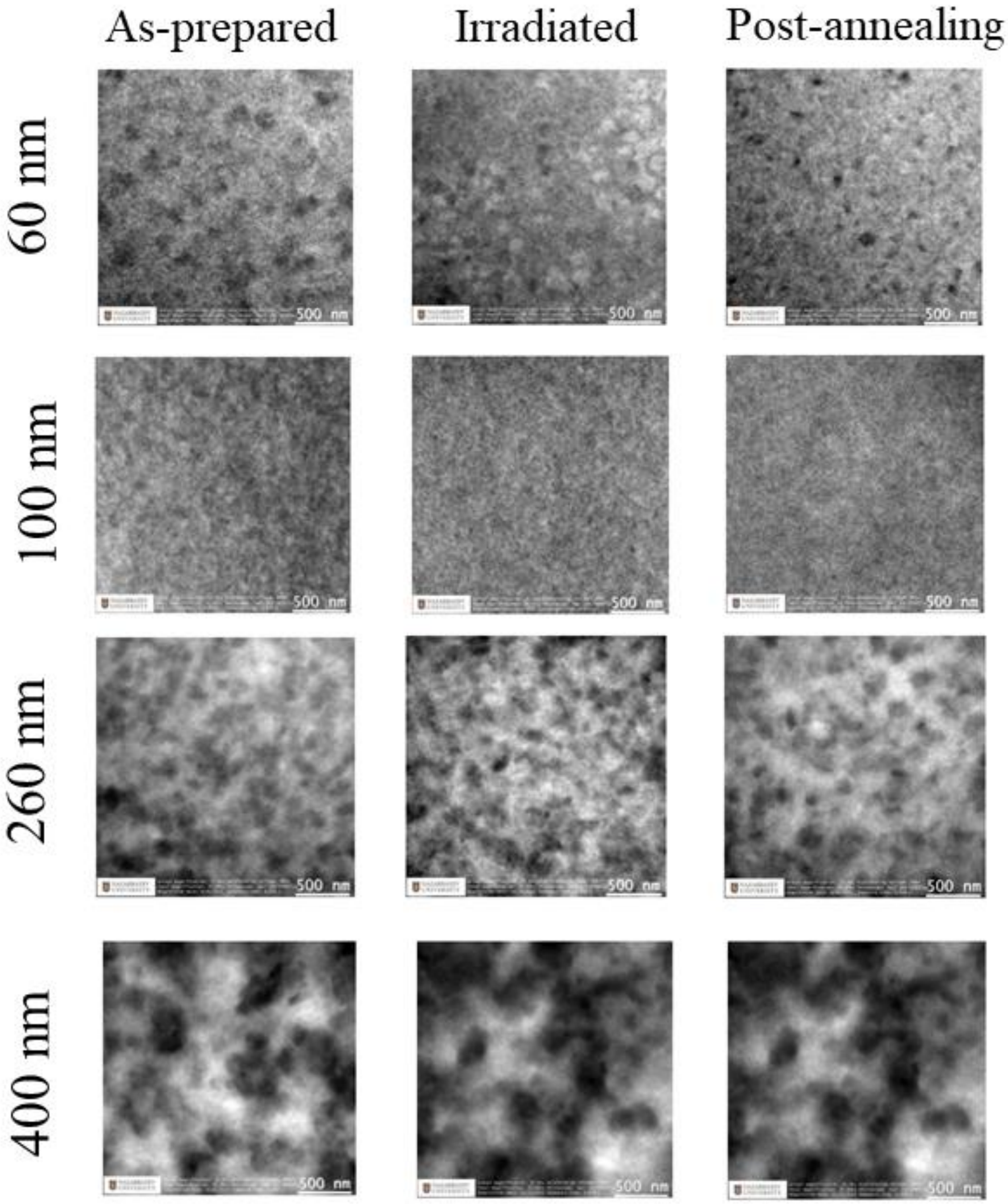

Figure 3.5 TEM images of PM6:Y6 thin film with different thickness for as prepared, irradiated and post-annealing.

3.2.3 Photovoltaic Characteristics

Figure 3.6 presents the J-V characteristics of studied devices and EQE spectra. The detailed photovoltaic performance data of OSC are provided in **Table 3.1**. Devices with thickness 60 and 100 nm of active layer revealed the highest PCE of 13.9 % and 14.3 % compared to thick active layer (260 nm and 400). To assess the degradation level of OSC after proton irradiation and post-annealing treatment, remaining factor defined as the ratio of PV parameter (irradiated or post-annealed) to the initial PV parameter was used. **Figure 3.7a** shows the dependents of remaining factor on the thickness of active layer. There is a small influence of thickness on the V_{OC} parameter after proton irradiation, since the V_{OC} of devices along thickness is almost flat. The J_{SC} of thicker devices suffered severely after proton irradiation, and its remaining factor reaches roughly 0.19 and 0.16, 260 nm and 400 nm, respectively. In comparison to thick devices, the J_{SC} of thin devices were degraded in a moderate behaviour, reaching a remaining factor of 0.36 for 60 nm and 0.23 for 100 nm. An increase in the thickness of the active layer correlates with a reduction in the J_{SC} of the irradiated devices as shown in **Figure 3.6 e,f,g and h**. As shown in **Figure 3.6b**, photovoiltaic characteristcs of devices were improved after post-annealing treatment. On thin devices, the J_{SC} parameter has shown the greatest impact in terms of improvements, and its remaining factor has improved to 0.2. Thicker devices, on the other hand, showed just a small improvement. In addition to enhancements in the short circuit current density parameter, the EQE of the device has been also improved.

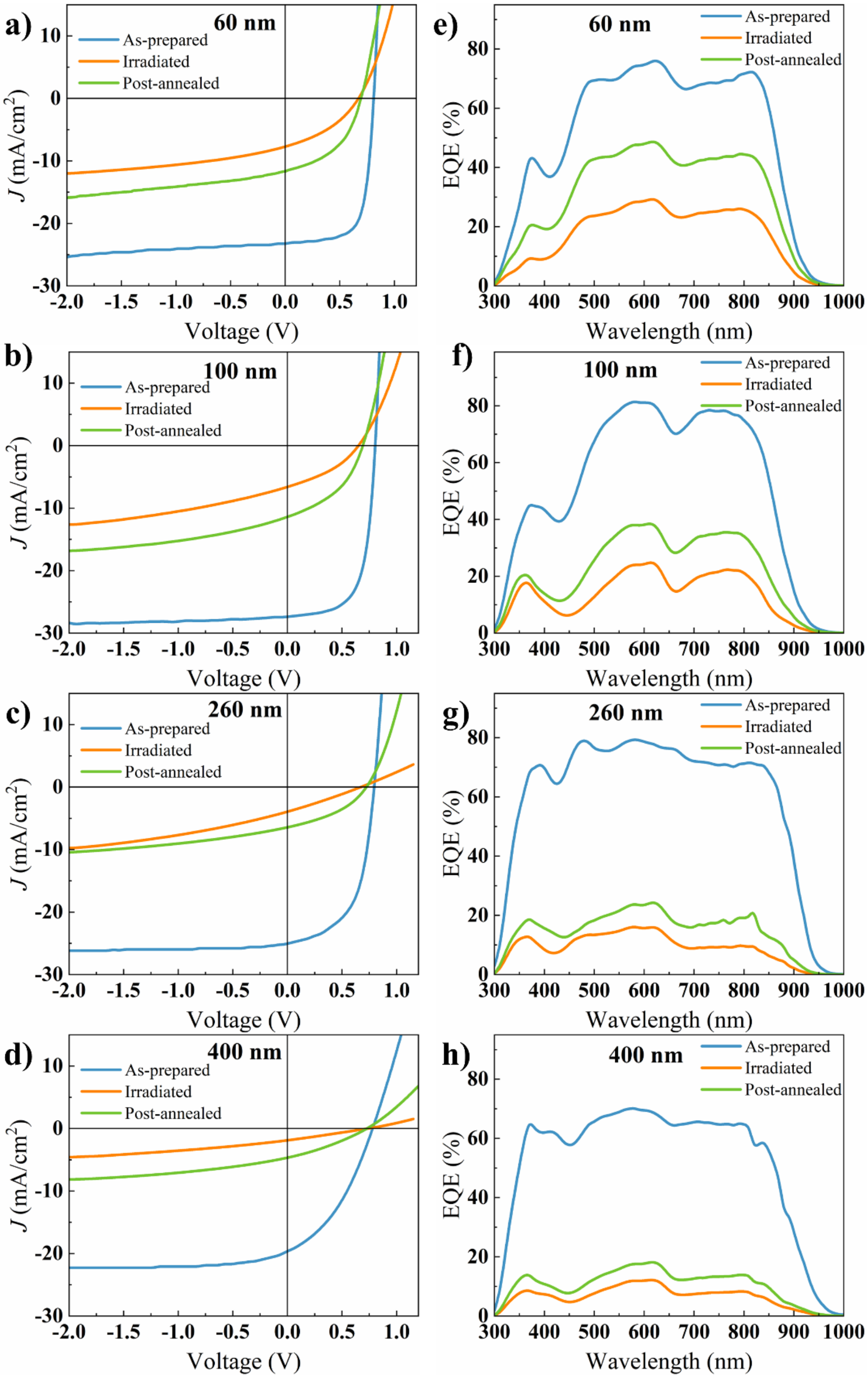

Figure 3.6 J-V charcateristics of devices measured under a) AM 1.5G solar irradiation at 100 $mW\ cm^{-2}$ b) irradiated c) post-annealed. External quantum efficiency spectra of devices under d) as deposited e) irradiated f) post-annealed.

Table 3.1. Photovoltaic parameters of PM6:Y6-based devices under AM 1.5G solar illumination.

	Thickness (nm)	V_{OC} **(V)**	J_{SC} **(mA/cm^2)**	***FF*** **(%)**	***PCE*** **(%)**
As-prepared	60	0.82 (0.81±0.003)	23.6 (23.4±0.18)	70.5 (69.4±1.55)	13.6 (13.21±0.36)
Irradiated		0.66(0.66±0.01)	8.12 (7.81±0.27)	39.81(38.73±1.43)	2.1 (2.00±0.11)
Post-annealed		0.70 (0.69±0.02)	11.6(12.13±2.16)	45.88 (43.95±2.8)	3.73 (3.74±0.94)
As-prepared	100	0.8 (0.8±0.01)	27.3(27.83±0.38)	64.75 (64.75±0.65)	14.27 (14.2±0.06)
Irradiated		0.65(0.65±0.003)	6.0(6.3±0.29)	36.47(36.22±0.24)	1.42 (1.48±0.06)
Post-annealed		0.69(0.7±0.002)	11.4(11.83±0.38)	41.59(41.59±0.25)	3.41 (3.4±0.12)
As-prepared	260	0.79(0.79±0.001)	25(25±0.099)	56(55.97±0.07)	11.18(11.13±0.07)
Irradiated		0.66(0.67±0.003)	3.36 (3.65±0.28)	27.07(55.97±0.07)	0.6 (0.66±0.05)
Post-annealed		0.7(0.71±0.01)	5.1(3.65±0.04)	36.82(36.7±0.15)	1.32 (1.32±0.015)
As-prepared		0.78(0.71±0.008)	19.67(18.55±1.73)	37.6 (37.97±0.65)	5.8 (5.51±0.38)
Irradiated		0.68(0.7±0.039)	2.27(2.07±0.19)	23.34 (24.69±1.9)	0.36(0.36±0.0014)
Post-annealed		0.72(0.73±0.004)	4.66 (4.52±0.26)	30.26 (30.6±0.53)	1.04(1.01±0.05)

The average parameters of 3-4 devices are presented in brackets.

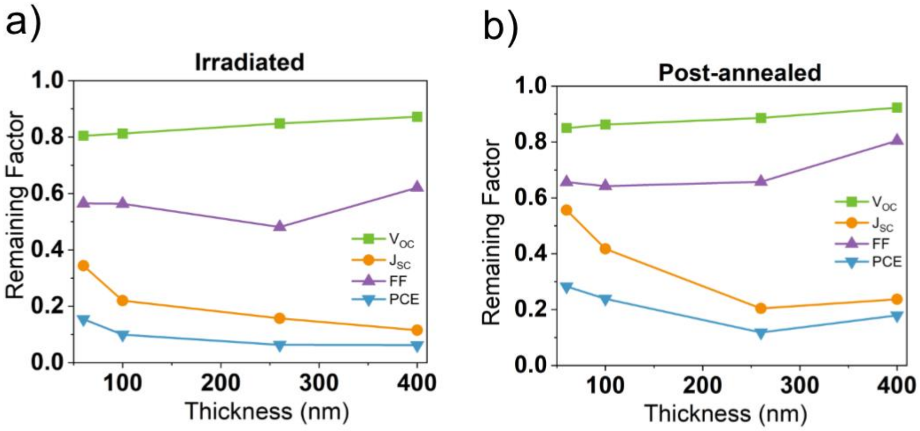

Figure 3.7 Remaining factor of photovoiltaic charcateristics of devices after a) proton irradiation and b) post-annealing treatment.

3.2.4 Thermal Annealing

To explain the recovery mechanism of the irradiated devices, the irradiated device with 100 nm thickness was heated up at 110 °C for 5 hours inside a nitrogen glovebox. The OPV performance of the irradiated devices are detected as a function of heating time , and result is presented in **Table 3.2**. It is noteworthy that the J_{SC} of the irradiated device is rised gradually from 6.3 mA/cm^2 to 17.87 mA/cm^2 during 5 hours, as shown in **Figure 3.8**. However, upon heating the irradiated device for 1 hour, FF and V_{OC} are reached the highest value are reached at 1 hour, and those parameters fluctuate slightly the rest of the time. The research conducted by Professor S. Forrest revealed a comparable pattern regarding the recovery process in the irradiated OSC. The study[122] utilized a proton energy of 30 keV to irradiate the organic solar cells (OSCs) composed of the PM6:Y6 blend, followed by heating the irradiated OSCs at 85°C for 5.5 hours. Examining the irradiated OSCs at different temperature (85 °C [122] and 110 °C (this work)) increased PCE by 25.53% and 29% during the similar time, respectively. The study demonstrated a comparable tendency of consistently increasing the J_{SC}, as shown in our research.

Table 3.2. Photovoltaic parameters of PM6:Y6-based devices at different time of thermal annealing.

Conditions	Post-Annealing Time	V_{oc}, V	J_{sc}, mA/cm^2	*FF*	*PCE*, %	$PCE_{Irr\ or\ Anneal}/PCE_{as-prepared}$,%	Comparison to S.Forrest work[122] $PCE_{Irr\ or\ Anneal}/PCE_{as-prepared}$, %
As-prepared		0.8±0.01	27.83±0.38	64.75±0.65	14.27±0.06	-	
Irradiated		0.65±0.003	6.3±0.29	36.22±0.24	1.48±0.06	10.37	50
Post-annealed	5 min	0.68±0.01	11.23±2.68	38.6±0.87	2.97±0.71	20.8	
Post-annealed	10 min	0.7±0.002	11.83±0.38	41.59±0.25	3.4±0.12	23.8	
Post-annealed	30 min	0.69±0.02	13.07±3.6	42.03±2.81	3.74±0.76	26.2	
Post-annealed	1 hour	0.69±0.01	13.85±3.7	43.79±3.36	4.05±0.81	28.38	62
Post-annealed	2 hours	0.7±0.01	16.75±1.32	41.54±0.92	4.8±0.55	33.6	
Post-annealed	3 hours	0.69±0.01	17.96±0.39	41.47±0.78	5.1±0.26	35.7	75
Post-annealed	5 hours	0.68±0.01	17.87±0.71	41.78±0.96	5.13±0.37	35.9	At 5.5 hours 79

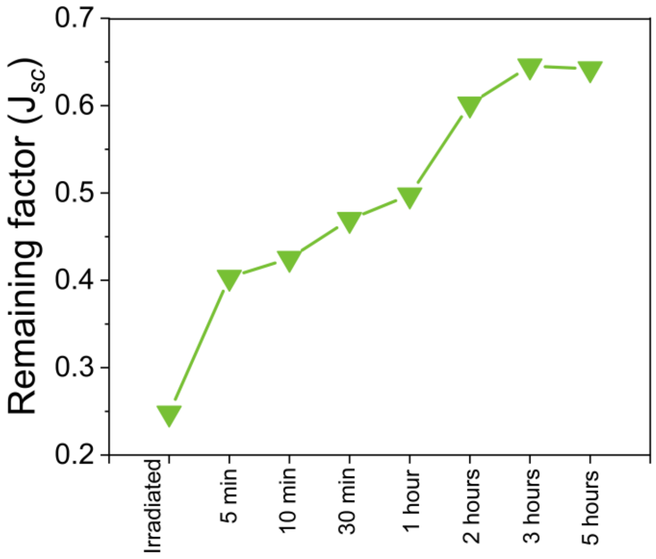

Figure 3.8 Remaining factor of J_{sc} at various stages of thermal annealing.

3.2.5 Generation, Recombination and Extraction processes

Generation rate

The thickness of each functional layer of the device and its optical properties (**Figure 9 and 10**) are used as input parameters for the transfer matrix approach, which models the generation rate at which excitons are created in OSC with a PM6:Y6 blend [101,102,124] .The generation rate as a function of wavelength λ and position within the active layer are plotted in a 2D plot fashion. The generation rate possesses the highest peak near the contact of the active layer with the ZnO transport layer in the $0 < x < 40$ nm range and decrease along the thickness of the active layer. During the light illumination from the ZnO transport layer, the active layer absorbs the most photons; therefore, the generation rate reaches the peak near the interface. Notably, the generation rate profile exhibits no change after irradiation and post-annealing as shown in **Figures 3.11**. This is mainly because the optical properties of the PM6:Y6 active layer insignificantly change after irradiation and post-irradiation annealing.

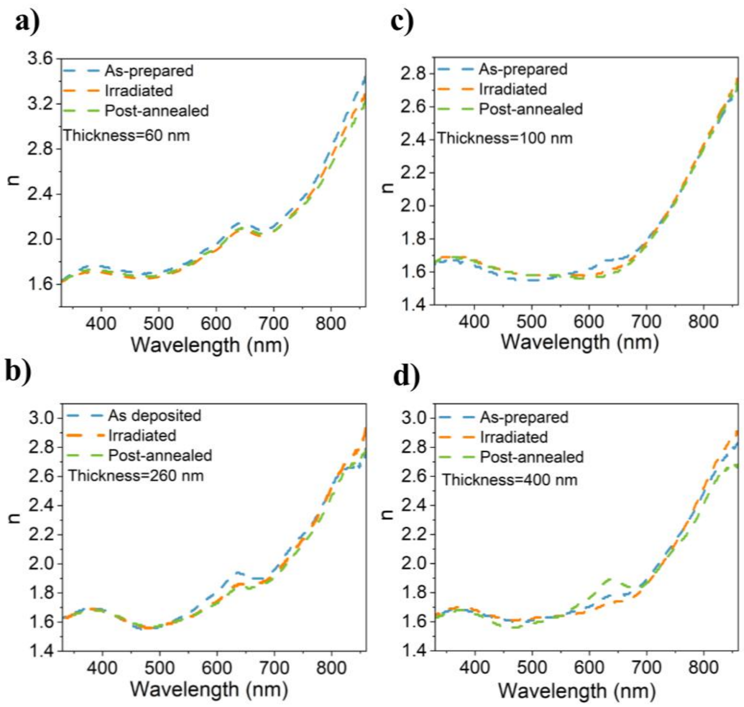

Figure 3.9 Refractive index (n) of PM6:Y6 thin films with thickness a) 60 nm b) 100 nm c) 260 nm d) 400 nm.

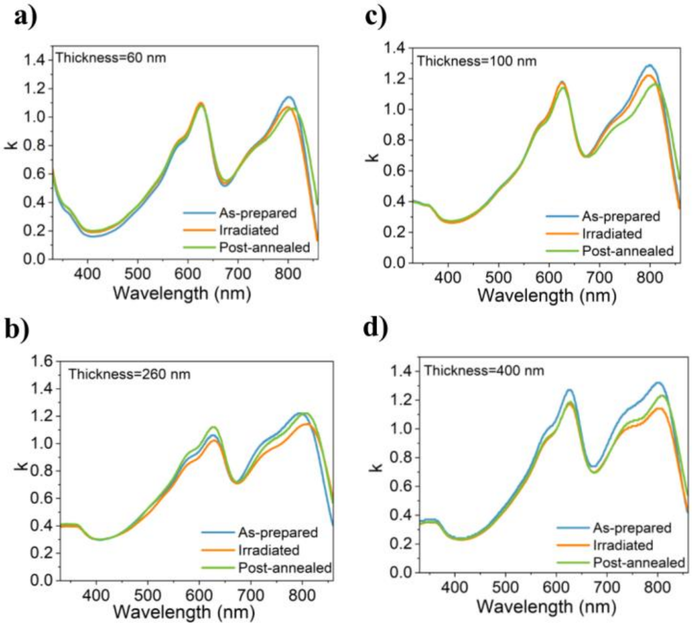

Figure 3.10 Extinction coefficient (k) of PM6:Y6 blend with thickness a) 60 nm b) 100 nm c) 260 nm d) 400 nm.

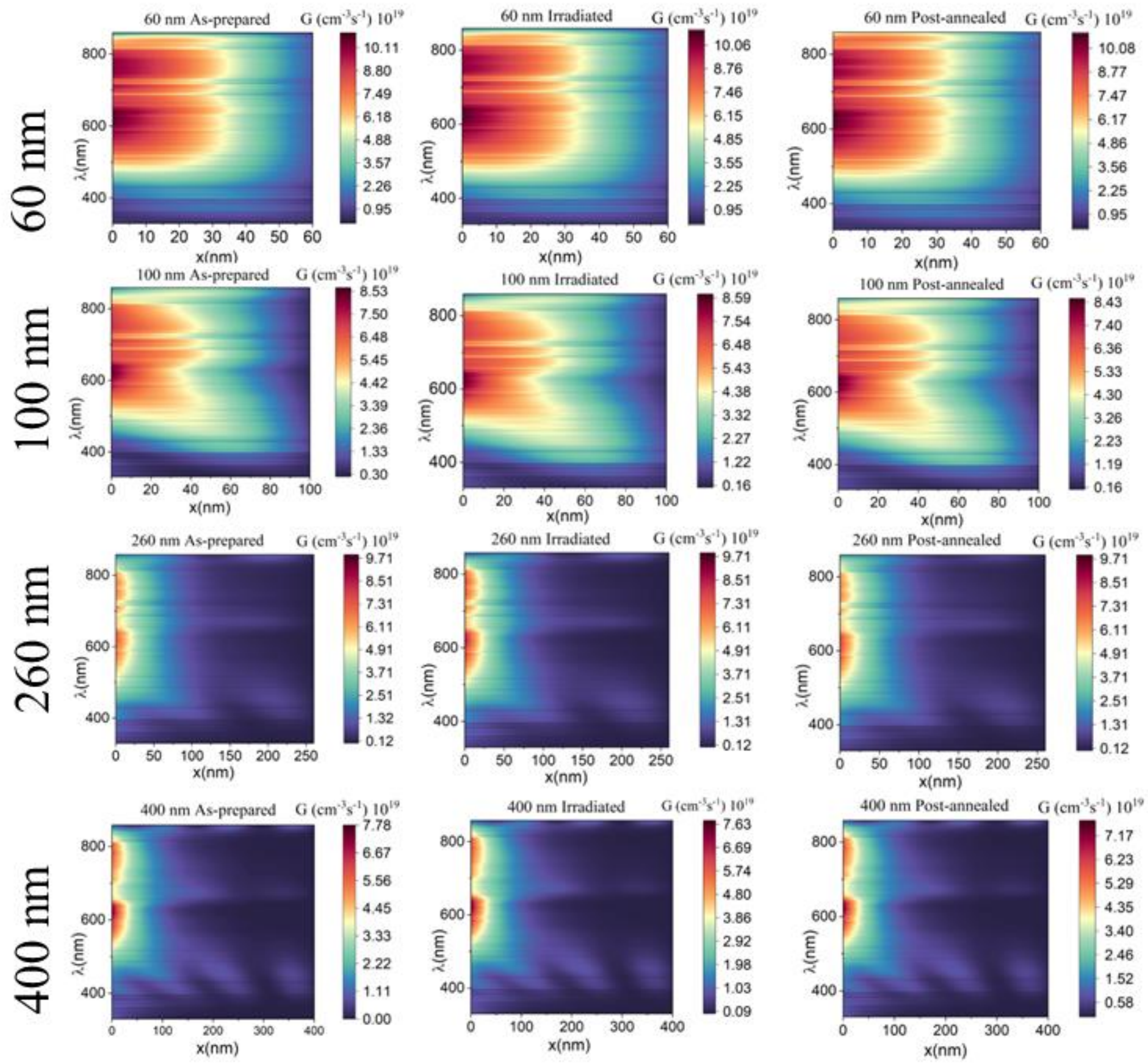

Figure 3.11 2D contour plot of Generation rate in PM6:Y6 in dependence of wavelength and thickness.

Recombination dynamic

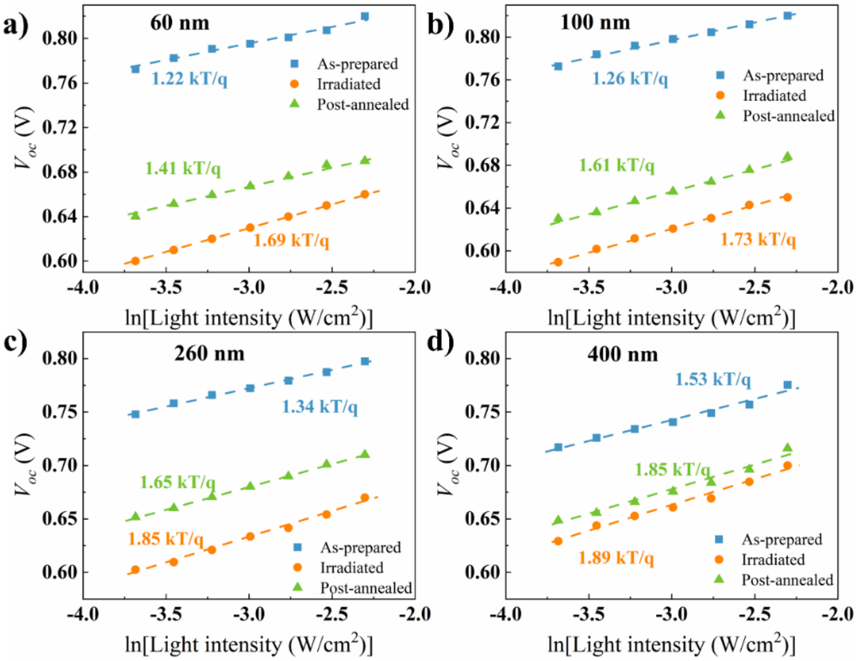

Figure 3.12 Voc vs Ln[Light Intensity] measurements of OSC for as prepared, irradiated and post-annealed treatments a) 60nm b) 100 nm c) 260 nm and d) 400 nm.

Figure 3.12 shows the V_{OC} measurement as a function of the natural logarithm of light intensity, identifying the slopes of the studied devices in order to evaluate the dominant recombination. For an as-prepared device with varying thicknesses, the slope of V_{OC} vs Ln (light illumination) measuremnts are slightly higher then 1 kT/q, indicating that trap-assisted recombination is dominant. Proton irradiation significantly increases the slopes of the studied devices and there is trend when thickness of active layer is increased the slopes of the irradiated device is also increased identifying the dominant trap-assisted (SRH) recombination in the bulk of PM6:Y6. Post-annealing treatment reduces the slope value in all devices, revealing recovery of radiation-induced traps. Noticeably, only devices with 400 nm thickness reveal a slight decrease in slope under post-annealing treatment, showing the poor recovery of traps.

To date the quantitative charcateristics of recombination processes, the impedance-voltage spectroscopy measurement combined with J-V characteristics was used. At first, the density of charge carriers and effective mobility are calculated using the measurements of impedance-voltage of devices for as-prepared, irradiated and post-annealed devices. The density of charge carriers were decreased for all studied devices after proton irradiation and recovered notably for devices with thin active layer (60 nm and 100 nm) after post-annealing as shown in **Figure 3.13**. **Figure 3.14** shows the effective mobility as a function of V_{corr}. For as-prepared devices, thick devices demonstrate a higher effective mobility of charge carriers compared to thin devices. The enhanced effective charge carrier mobility observed in thicker devices can be attributed to the higher concentration of 1.5% (v/v) 1-chloronaphthalene (CN) used as a solvent additive in the PM6:Y6 blend solution, in contrast to the 0.5% CN concentration employed in thinner devices[77]. The effective mobility of charge carriers in the irradiated devices were reduced by one order of magnitude in thick devices compared to a half of magnitude reduction in thin devices. Devices with thick active layers (260 and 400 nm) showed a marginal improvement, while those with active layer thicknesses of 60 and 100 nm exhibited almost complete recovery in their effective mobilities.

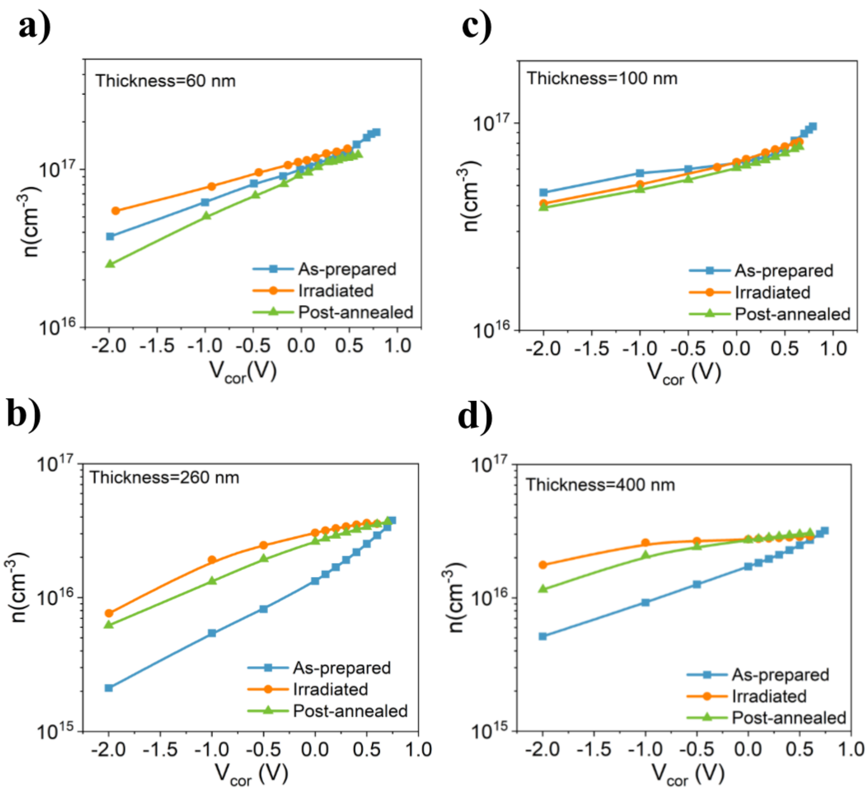

Figure 3.13 Charge carrier density of devices at conditions: As prepared, Irradiated and Post-annealed a) 60 nm b)100 nm c)260 nm and d)400 nm.

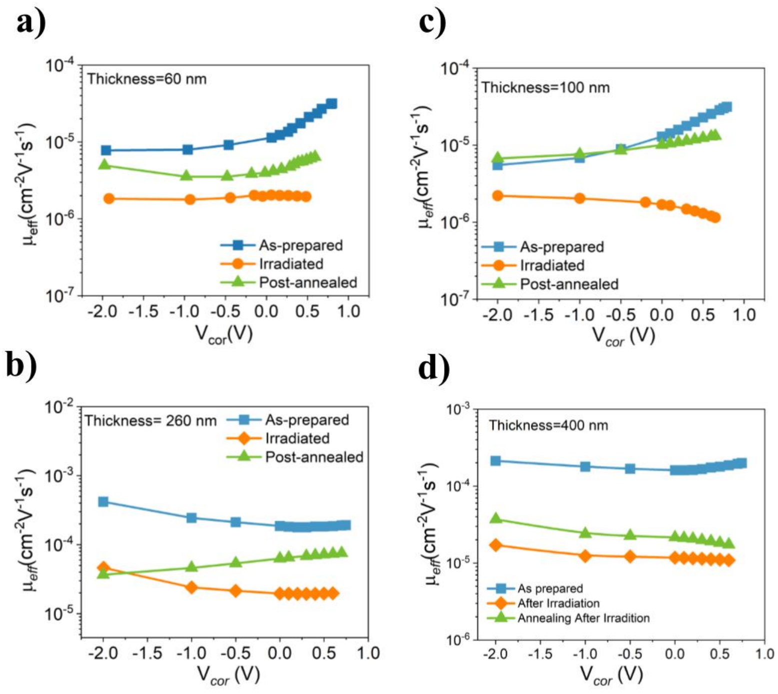

Figure 3.14 Effective mobility of the devices at conditions: As prepared, Irradiated and Post-annealing a) 60 nm b) 100 nm c) 260 nm and d)400 nm.

The multi-mechanism recombination model was applied to quantify the density of traps in both the bulk and surface, along with the bimolecular recombination. The fitting parameters as the Langevin coefficient ξ, the density of traps in the bulk N_{tb}, and the density of surface traps N_{ts} were employed to fit the simulated recombination current with experimental recombination current. The Langevin reduction factor revealed the stable behavior upon proton irradiation and post-annealing treatment. The unaltered Langevin reduction factor in all studied devices is correletes with optical properties and morphology of PM6:Y6 thin films[120].

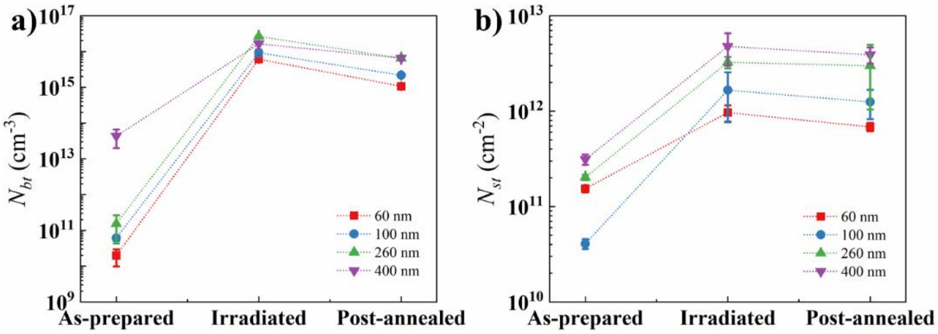

Figure 3.15 a) the density of traps in the bulk b) the density of the trap at the surface.

Figures 3.15 a and b present the density of bulk and surface traps after irradiation and post-annealing treatment. Due to the larger, coarse, phase-separated grains, the prepared devices with a thickness of 400 nm exhibited the highest density of bulk and surface traps. The as-prepared device with a thickness of 100 nm exhibited the lowest density of surface traps, leading to both good photovoltaic performance and a low roughness value. Conversely, the thick active layer devices exhibited the highest density of surface traps in the as-prepared device, which was associated with a high roughness value. Proton irradiation increases the density of bulk traps by almost 5 orders of magnitude in all devices. Importantly, the density of traps in the bulk was increased as the thickness of the active layer increased. Consequently, a high concentration of traps in the bulk led to the degradation of the$J_{SC}$and EQE spectra.

The post-annealing treatment slightly restores the traps in the bulk of the active layer. Furthermore, post-annealing treatments recover slightly the density of traps in the surface in all devices. Based on the research carried out by the work[119], it has been shown that the radiation created traps in P3HT:PCBM and PCDTBT:PCBM systems, and it has identical electronic properties, and certain traps can be reversed by post-annealing. Since proton irradiation increases the density of traps in the surface, post-annealing treatment slightly recovered the trap in the surface in all thicknesses. This suggests that the residual compounds are surface traps that were recovered during post-annealing, as a result of the removal of trapping centers at the ZnO/BHJ interface[119,120].

Charge extraction dynamic

The photocurrent density as a function of the effective voltage on a double logarithmic scale was used to provide the understanding of the extraction process in OSCs. The photocurrent density, denoted as J_{ph}, is calculated as the difference between the current density under light (J_{light}) and the current density under dark (J_{dark}). V_{eff} is defined as the difference between V_0 and V_{corr}, where V_0 - is the voltage at zero photocurrent and $V_{applied} - J \cdot R_s$ is the corrected voltage that includes the voltage loss over the series resistance. As it can be seen in **Figure 3.16**, the photocurrent of as-prepared thin devices is higher compared to thick devices while the saturation voltage in thin devices is lower compared to thick devices. Due to the high density of trap in the irradiated device, the increased saturation voltage and the reduced photocurrent density of irradiated devices are determined. The important observation is that the saturation regime of all irradiated and post-annealed devices has not been detected within the measured voltage range. This indicates that higher $V_{applied}$ should be applied to all irradiated and post-annealed devicse in order to extract all charge carriers. Even with the requirement of higher applied voltage, the thin device shows better photocurrent compared to thicker devices, identifying the influence of the thickness of the active layer.

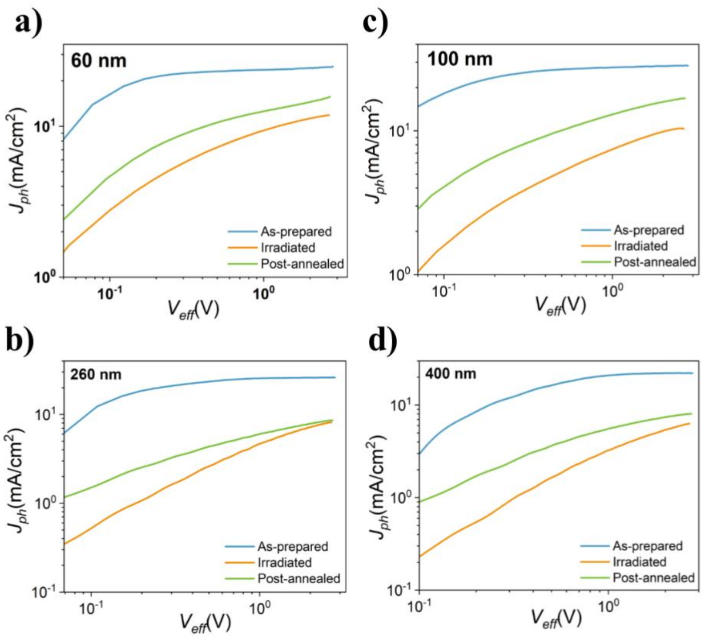

Figure 3.16 Photocurrent density versus the effective voltage.

The Hecht equation calculated the average extraction efficiency by combining the extraction efficiency for electrons and holes, both of which are dependent on the position (x) of the active layer [125]. The equations (3.1-3.4) define the average extraction efficiency of the inverted organic solar cells, which are illuminated from the ZnO transport layer. To describe the average extraction efficiency, the mean free path defined how charge carriers move in the active layer (with a thickness of L) before the charge carriers are recombined. The mean free path is defined by the multiplication of the internal electrostatic field V_{bi}/L with mobility and lifetime [114].

$$\bar{\eta} = \eta_n + \eta_p \tag{3.1}$$

$$\eta_n = \frac{w}{L}(1 - exp(\frac{-(L-w)}{w})) \tag{3.2}$$

$$\eta_p = \frac{w}{L}(1 - exp(\frac{-x}{w})) \tag{3.3}$$

$$w = \frac{\mu\tau V_{bi}}{L} \tag{3.4}$$

Figure 3.17 illustrates the average extraction efficiency of the devices under short-circuit conditions, for as-prepared, irradiated, and post-annealed devices. Specifically, the irradiated thin devices deteriorate moderately ($\bar{\eta}$= 0.37 for thickness 60 nm), while the thicker devices degrade severely ($\bar{\eta}$ = 0.07 for thickness 400 nm). Proton irradiation reduces the extraction efficiency, which correlates with thickness of PM6:Y6. **Figure 3.17** illustrates that the post-annealing treatment improves the extraction efficiency of thin devices with a thickness of 60 nm , reaching a value of 0.62. In contrast, a device with a thickness of 400 nm shows insufficient recovery, reaching only $\bar{\eta}$ =0.13.

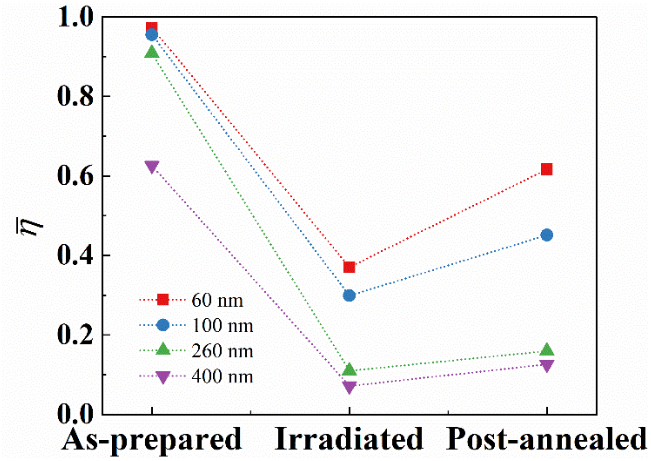

Figure 3.17 The average extraction efficiency of devices at 0 V for PM6:Y6 blend with thicknesses 60, 100, 260, and 400 nm at conditions: as-prepared, irradiated, and post-annealing.

Organic semiconductors possess distinctive material characteristics in contrast to inorganic and perovskite semiconductors. Proton irradiation induces shallow traps in perovskite; nevertheless, these shallow traps do not participate in the nonradiative recombination process. Instead, they function as unintentional doping sources that unintentionally induce doping in perovskites. Proton irradiation in organic semiconductors generates traps within the deep energy levels of the bandgap. The breakdown of C-H and N-H bonds occurs due to their low mass, resulting in the formation of H-vacancies [122].The irradiation-induced trap, positioned as mid-gap states within the bandgap, is responsible for recombination due to the growth of bulk and surface traps, which function differently at varying thicknesses. Another distinctive characteristic of organic semiconductors is their reversibility during thermal annealing. Significantly, the C-H bond can reconnect and partially restore the functionality of OSC. According to the literature [33,126], N-H bonds can only be reversed at a temperature of 30 K. The irreversible nature of the N-H following heating may hinder the complete recovery of OSC.

3.4 Experimental Section

Materials:

The PM6 was bought from 1-Material Inc. company and the Y6 was bought from Ossila. The glass substrates coated with ITO were purchased from Ossila Ltd., GB. The diethyl zinc, tetrahydrofuran, chlorobenzene, and 1,8-diiodooctane were acquired from Sigma–Aldrich, USA. The molybdenum oxide powder and silver pellets were acquired from Kurt J. Lesker, USA.

Material Characterization Characterization

TEM images were obtained with a Jeol JEM-1400 Plus setup. The films were spin-coated as the active layers on Glass/PEDOT:PSS. Then, each film was carefully detached from the substrate by dissolving the PEDOT:PSS layer in distilled water so that the film could be transferred to a copper 100 mesh TEM grid. The active layer analysis was performed at an accelerating voltage of 80 kV and 30 kx total magnification by Jeol JEM-1400 Plus system. For analysis of chemical composition, PM6:Y6 active layers were deposited on Glass/ITO substrate by spin-coating method. The transmission and reflection spectra of the PM6:Y6 active layer were measured using UV–vis-NIR spectrophotometer (Lambda 1050, PerkinElmer). Atomic Force Microscope SmartSPM 1000 was used to measure the roughness of the PM6:Y6 active layer. The thickness of PM6:Y6 thin films were measured by contact profilometer (Dektak XT , Bruker company).

Fabrication of Organic Solar cells

The organic solar cells were fabricated in an inverted device structure as Glass/ITO/ZnO/PM6:Y6/MoOx/Ag. The Glass/ITO substrates were cleaned with soap and sonicated in distilled water, acetone, and isopropyl alcohol for 15 min. For the inverted device structure, a bottom contact ZnO prepared by a solution of tetrahydrofuran and diethylzinc in a 2:1 volume ratio, then spin-coated at 4000 rpm for 15 s in air. The Glass/ITO/ZnO was annealed at 150 °C for 30 min and subsequently transferred to a nitrogen glovebox. The active layer PM6:Y6 with thickness 60 and 100 nm (11mg/mL and 17.6 mg/mL, 1:1.2 D/A mass ratio in chloroform with 0.5% chloronaphthalene) were deposited on the top of ZnO by spin coating at 3000 and 3600 rpm , respectively, for 30 s inside the glovebox. For the thickness 260 and 400 nm, the optimized receipt of PM6:Y6 was [77] (25 mg/mL, 1:1.2 D/A mass ratio in chloroform with

1.5% chloronaphthalene) was deposited by spin coating at 1800 rpm and 750 rpm, respectively, for 30 s. Then Glass/ITO/ZnO/PM6:Y6 samples were annealed on the hot plate inside glovebox at 110 °C for 10 min. The electrode and the hole transport layer, Ag (120 nm) and MoOx (5nm) were deposited by thermal evaporation system in a vacuum deposition at pressure 10^{-6}. The active area of the solar cell is 0.1 cm^2 and the mask with 0.0512 cm^2 the active area was used for measurements.

Proton Irradiation

Irradiatedof samples and devices were performed by INURA pulsed high-current proton/electron accelerator placed at Nazarbayev University.

INURA pulsed high-current proton/electron accelerator consists of a high voltage generator that produces an impulse with a rate of $10^{12}\ p\ cm^{21}$ and 100 ns duration.

The production of proton beam is based on the formation of the surface discharge plasma on the anode which is the birthplace for the proton beam. It is important to mention that a proton beam is gained by a single voltage impulse. The samples and devices are placed inside a vacuum chamber and at a distance of 35 cm from the diode which is pumped down to 5×10^{-2} mTorr. The characteristics of proton beam: 150 ns, 170 keV, and flux $10^{12} p\ cm^{-2}$.

Thermal Annealing

The irradiated PM6:Y6 thin films deposited on glass and OSC devices were placed inside the glovebox. Devices and PM6:Y6 thin films deposited on glass were annealed on the hot plate at 110 ° C for t=10 min inside the glovebox.

Device Characterization

Semiconductor Device Analyzer (B1500A, Keysight) in union with an Oriel 3A solar simulator with an intensity of 100 mW cm−2 were utilized to measure the J–V characteristics of devices.For Voc & light intensity measurements, the same solar simulator system was used in conjunction with filter NDK01 by the company THORLABS. To measure the frequency-resolved capacitance, impedance analyzer (SI1260, Solartron) were used. The impedance spectra depending on frequency in the range of $10^1 - 10^6$ Hz was measured under 1 sun and dark modes, applying a small AC disturbance of 40 mV. The range of applied bias is in the range of -2 V to the respective V_{OC} . In the case of EQE, ORIEL IQE 200 measurement system (Newport) was used to measure the external quantum efficiency spectra of the devices.

3.5 Supplementary Information

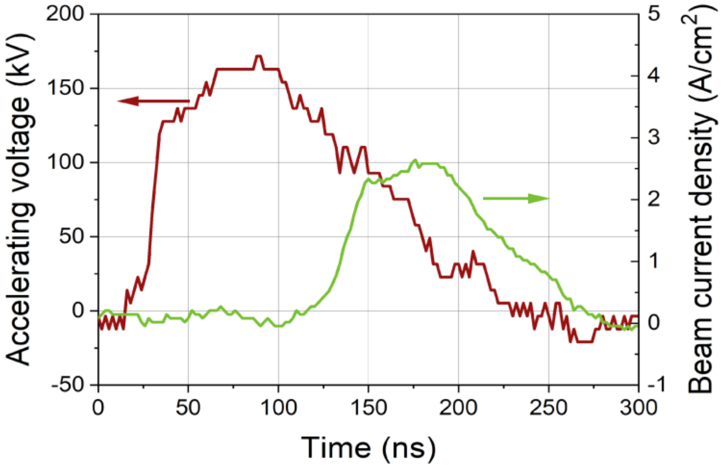

Figure S3.1. The parameters of INURA accelerator: the accelerating voltage and proton beam current density.

Table S3.1. The series resistance of studied devices.

Thickness of PM6:Y6 blend	As prepared R_s(ohm cm^2)	Irradiated R_s(ohm cm^2)	Post-annealed R_s(ohm cm^2)
60 nm	3.55	25.34	12.01
100 nm	3.81	39.74	19.7
260 nm	4.85	103.98	37.52
400 nm	4.22	353	93.34

Recombination Current density

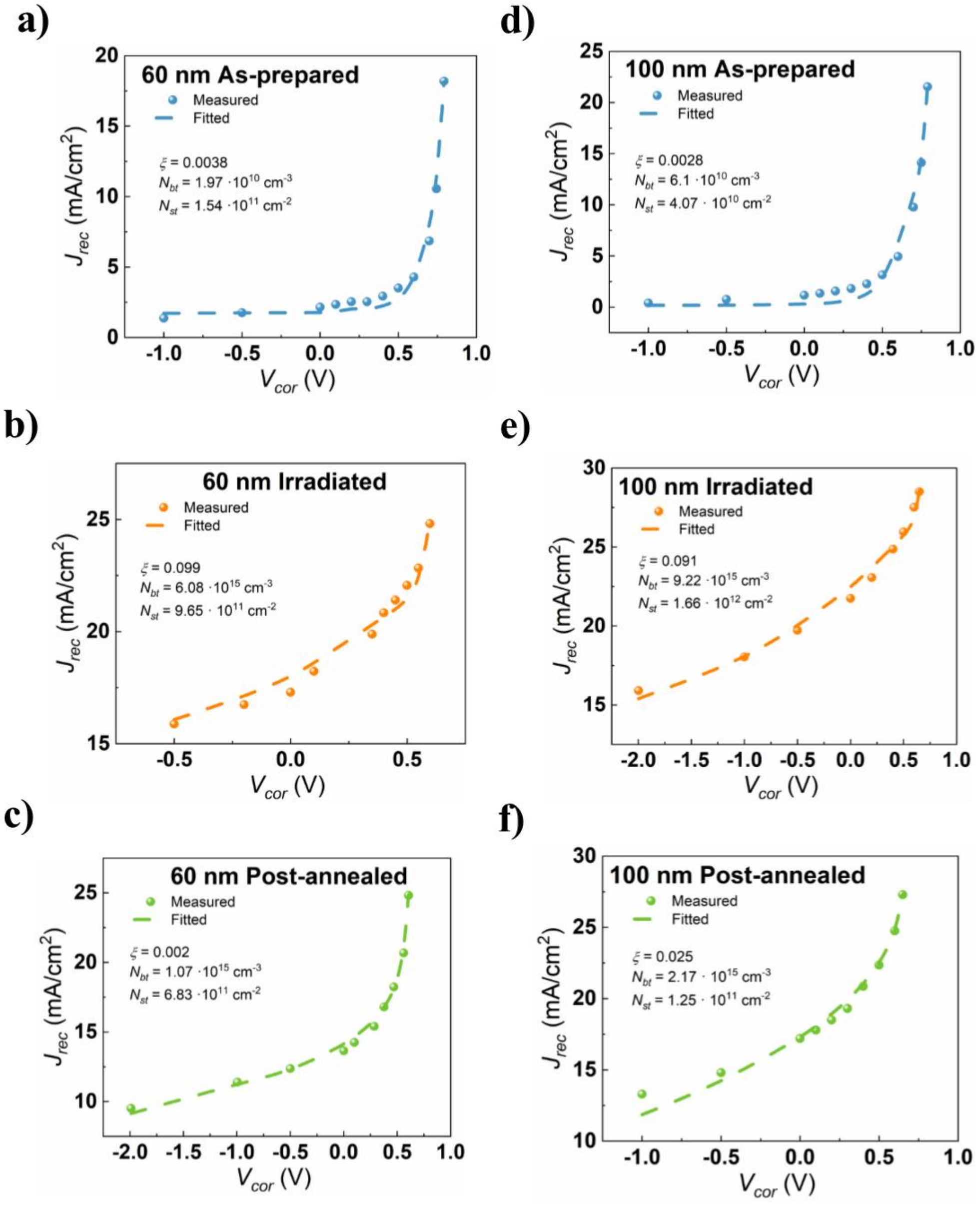

Figure S3.2. Fitting of experimentally measured recombination current density to simulated recombination current density for thinkness 60 nm a) As prepared b) Irradiated c) Post-annealed and 100 nm d) As prepared e) Irradiated f) Post-annealed.

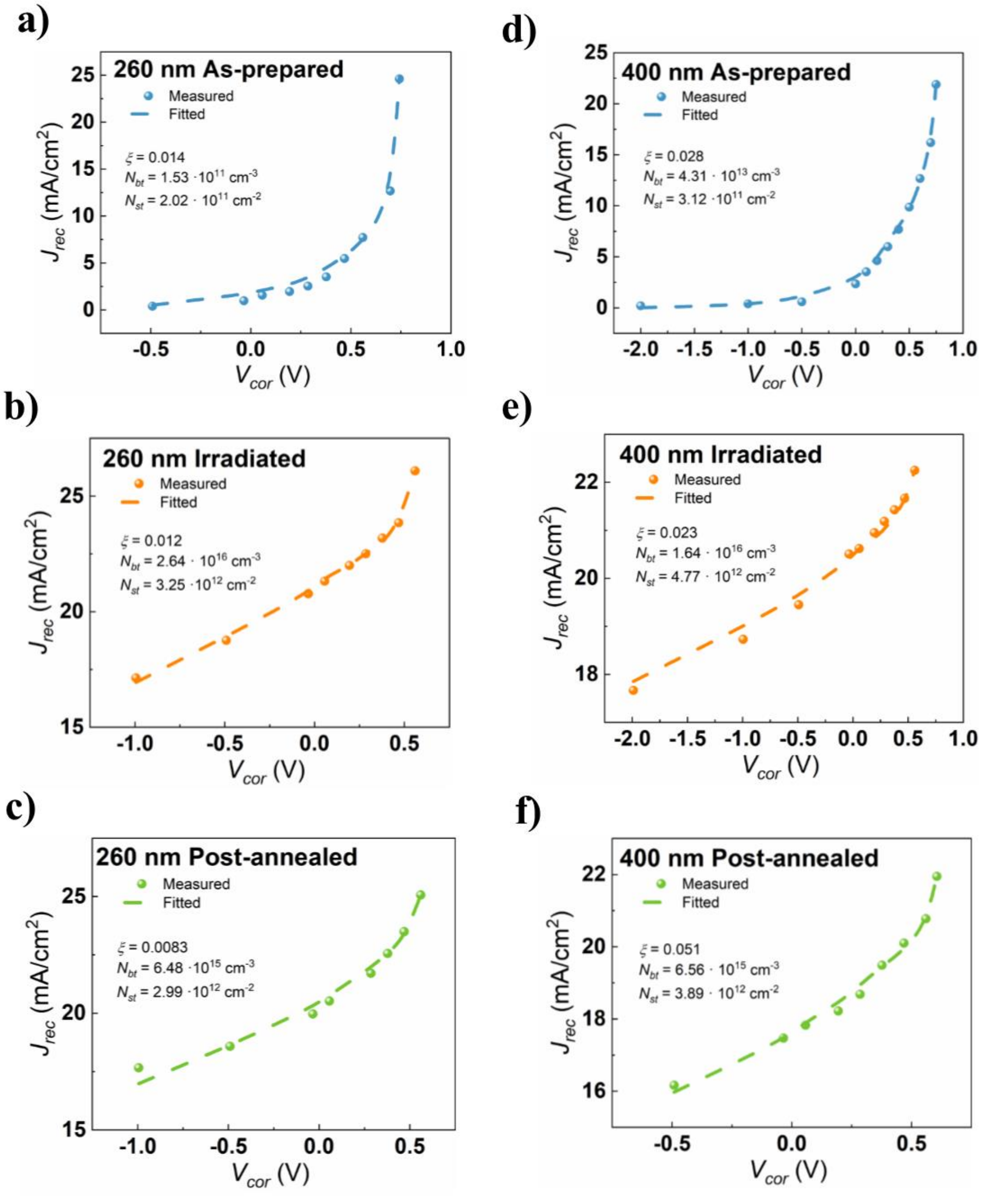

Figure S3.3. Fitting of experimentally measured recombination current density to simulated recombination current density for 260 nm a) As prepared b) Irradiated c) Post-annealed and 400 nm d) As prepared e)Irradiated f) Post-annealed.

Chapter 4 Inverted vs Conventional structure of organic solar cells under proton irraditian and characteristics of radiation tolerance of functional layer

4.1 Introduction

The photovoltaic performance and stability of OSC are improved by transport layers, which extract electron and hole carriers from the photoactive layer and transfer them to the appropriate electrodes [71]. The transport layer in the device acts to adjust energy level alignment at the electrode/active-layer interfaces, tailor the built-in electric field, define electrode polarity and enhance charge selectivity, control surface energy by modifying the active layer's morphology, and enhance transport stability between the active layer and electrodes [127–130] . The insertion of an transport layer between the active layer and the electrode intends to prevent the formation of a Schottky barrier, specifically by aligning the Fermi energy levels of the electrodes with the quasi-Fermi energy levels of the bulk heterojunction (BHJ) and selectively extracting charges [112]. This improvements enhance the increase of $V_{OC}$and FF parameters [131].

Based on electrode polarity and transport layer properties, the structure of organic solar can be inverted or conventional. Notably, C-OSC suffer from rapid deterioration and low lifetime caused by the acidic and hydrophilic nature of PEDOT:PSS, and the sensitivity of low WF metal anodes to oxygen and moisture [132,133]. The advantageous of inverted (I-OSC) is the device stability due to high WF metals (i.e., Au, and Ag) as the top electrode and a low WF metal oxide cathode interface layer (CIL) modified ITO as the transparent cathode.

Placing OSC into space consisting of the exposure of protons and electrons causes the deterioration of functional layers due to radiation-induced defects. For example, the investigation of the recombination process in organic solar cells under proton irradiation reveals the formation of traps in the bulk and at the interface. Especially, the formation of proton-induced defects in the ZnO and MoO transport layer raise the question about the radiation resistance of the functional layer[120]. Since the heart of a solar cell is semiconductor material, the radiation resistance of a variety of semiconductors has been investigated widely. However, the radiation resistance of the functional layer should be investigated separately in order to distinguish the deterioration from active layer and transport layer/electrodes. Particularly, systematic discussions should explain the influence of each functional layer as well as the impact that the material properties of functional layers have on OSC device performance under harsh environment. More importantly, the radiation induced defects created within the transport layer affects the properties of the structural, optical and morphology features of functional layers which in turn affects the work function and mobility characteristics of the functional layers.

Therefore, we investigate the radiation tolerance of the inverted (I-OSC) and conventional (C-OSC) organic solar cells with absorber layer PM6:Y6 blend specifically focusing on the radiation resistance of the functional layers as electrodes and transport layers. Next, material characteristics of functional layers such as optical and structural are investigated.

4.2. Results and Discussion

4.2.1 Device Physics

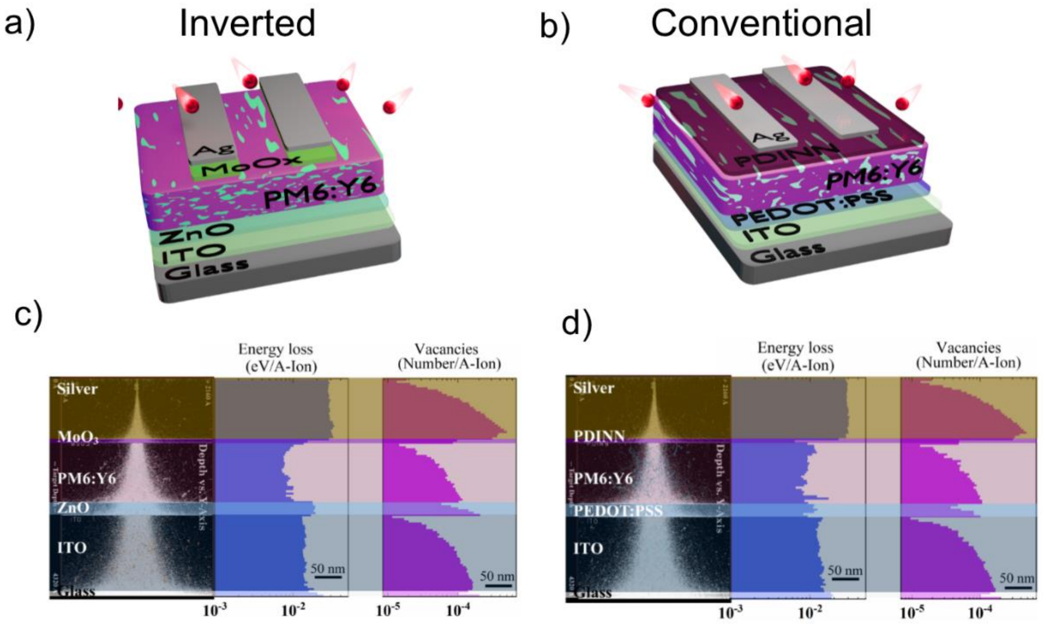

Figure 4.1. Device structure under proton irradiation a) inverted and b) conventional. The SRIM simulation of proton penetration within a device with quantitative analysis of energy loss and vacancies in each functional layer for c) inverted and d) conventional.

Herein, we investigate the radiation resistance of inverted (I-OSC) and conventional (C-OSC) solar cells with absorber materials as the blend of Poly[[4,8-bis[5-(2-ethylhexyl)-4-fluoro-2-

thienyl]benzo[1,2-b:4,5-b']dithiophene-2,6-diyl]-2,5-thiophenediyl[5,7-bis(2-ethylhexyl)-4,8-dioxo-4H,8H-benzo[1,2-c:4,5-c']dithiophene-1,3-diyl]-2,5-thiophenediyl] **(PM6)** as a polymer donor and 2,2'-((2Z,2'Z)-((12,13-bis(2-ethylhexyl)-3,9-diundecyl-12,13-dihydro-[1,2,5]thiadiazolo[3,4-e]thieno[2",3'':4',5']thieno[2',3':4,5]pyrrolo[3,2-g]thieno[2',3':4,5]thieno[3,2-b]indole-2,10-diyl)bis(methanylylidene))bis(5,6-difluoro-3-oxo-2,3-dihydro-1H-indene-2,1-diylidene))dimalononitrile **(Y6)** as an electron acceptor. **Figure 4.1 a and b** display the structure of the inverted and conventional structure consisting of following functional layers in I-OSC: Glass/ITO/ZnO/PM6:Y6/MoOx/Ag and C-OSC: Glass/ITO/PEDOT:PSS/PM6:Y6/PDINN/Ag. As it can be seen from device structure, the electrodes are identical but the polarity of electrodes are different due to interface layers. To identify the proton irradiation effect on the photovoltaic performance of I-OSC and C-OSC, the PM6:Y6 blend is prepared with the same thickness (100 nm) and identical receipt in both architectures. Identical proton irradiation and transportation conditions were applied to all devices. The interaction between protons and the device structure results in the loss of proton energy, causing atoms in the lattice to move and creating vacancies and interstitials. The SRIM software is used to determine the energy loss and vacancy production in device stack. The SRIM simulation is carried out using the density and thickness of the layers, as well as the energy of protons. **Figure 4.1 c and d** illustrate the energy loss in both configurations of organic solar cells. The proton beam has the following characteristics: proton energy of 170 keV and a fluence of $1 \cdot 10^{12}$p cm^{-2}.

4.2.2 Photovoltaic Performance

The photovoltaic charcateristics of devices are presented in **Table 4.1**. The external quantum efficiency (EQE) spectra are shown in **Figure 4.2b.** To evaluate the level of degradation in the irradiated devices, the remaining factor framework is used which is determined as the ratio of irradiated PV parameters to its initial value. The proton irradiation causes a minimal decrease in the open circuit voltage (V_{OC}), with a remaining factor of 0.9 for I-OSC and 0.86 for C-OSC. The fill factor of the irradiated device exhibited moderate degradation with only minor difference observed between inverted and conventional OSC structures. The most significant degradation is observed in the remaining factor of J_{SC} is 0.45 of the inverted structure and 0.35 of the conventional structure. It appears that the OSC with conventional structure suffers a significant decrease, notably the short circuit current density. **Figure 4.2b** displays the external quantum efficiency (EQE) spectrum. The as-prepared inverted device exhibited a maximum EQE of approximately 83% at a wavelength of 560 nm. In comparison, the as-prepared conventional device demonstrated a slightly lower maximum EQE of 80.6% at the same wavelength. Upon exposure to ionizing irradiation, the EQE spectrum of the inverted device showed moderate degradation, with the EQE at 560 nm decreasing from 80% to 40%. In contrast, the irradiated conventional device displayed a more pronounced decline, with a maximum EQE of only 31%, observed at 470 nm. The EQE spectra of both irradiated and non-irradiated devices in both architectures show good correlation with the integrated short-circuit current density (J_{SC}), as presented in **Figure 4.3**.

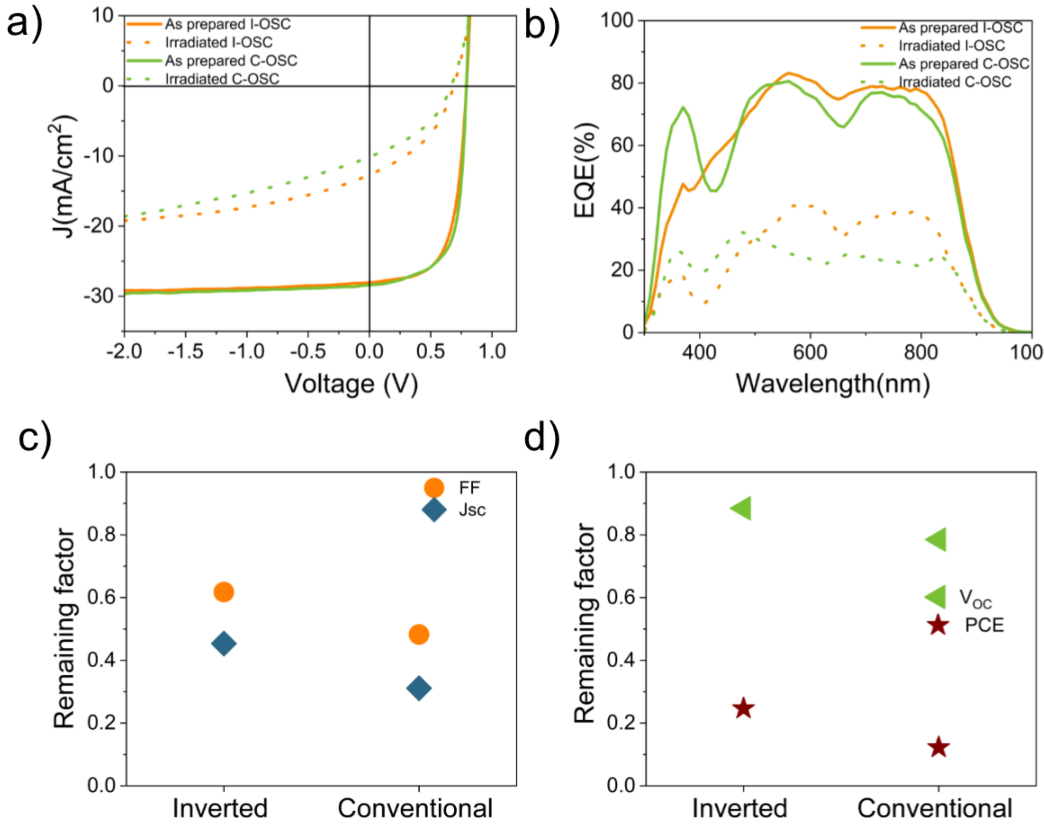

Figure 4.2. a) J-V measurement of as-prepared and proton irradiated OSC b) EQE c) Remaining factor of FF and Jsc d) Remaining factor of PCE and V_{OC}.

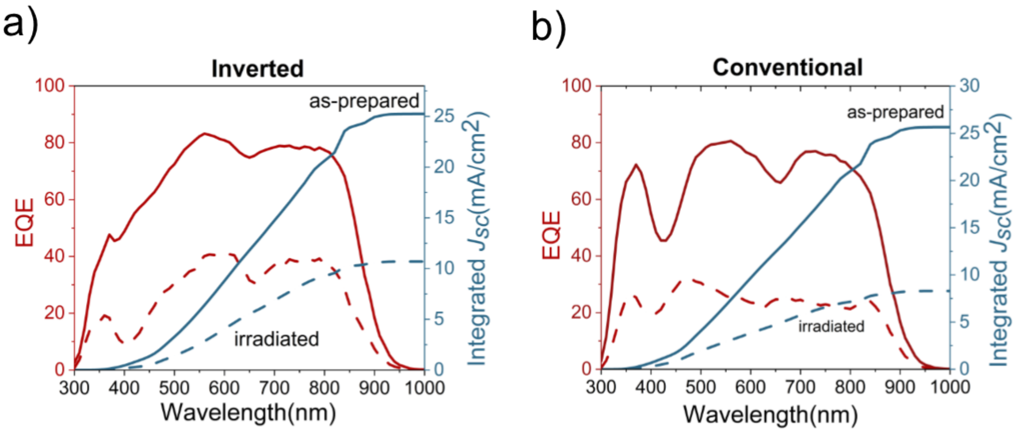

Figure 4.3 EQE and integarted J_{SC} for as prepared and irradiated devices.

4.2.3 Recombination

To identify the dominant recombination, we employed the qualitative analysis of V_{OC} vs Light intensity of OSC in inverted and conventional structure before and after irradiation. Prior to proton irradiation, the as-prepared devices revealed the slope 1.3 kT/q and 1.22 kT/q for inverted and conventional structure as shown in **Figure 4.4 a and b** , respectively. This indicates trap-assisted recombination dominance in both structure. The irradiation exposure of devices led to increase the value of the slope to 1.87 kT/q and 1.93 kT/q, for inverted and conventional, respectively. Considered in the scope of Shockley-Read-Hall (SRH) formalism, the increase of slope dictates the degradation of PM6:Y6 due to generated radiation-induced traps in the bulk and surface. However, the different levels of degradation in fill factor, V_{OC} and J_{SC} of device imply the non-identical radiation resistance of transport layers.

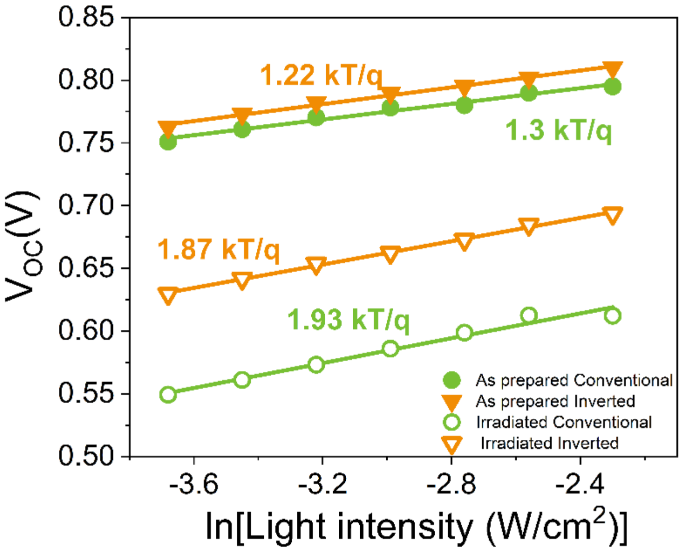

Figure 4.4 V_{OC} dependence on Ln (Light intensity) of both architectures e) As prepared and e) Irradiated.

Table 4.1. The photovoltaic performance of OSC.

Device Type	**Treatment**	V_{OC} **(V)**	$J_{SC}(mA/cm^2)$	**FF (%)**	**PCE$_{MAX}$ (PCE$_{AVE}$) %**
Inverted	As-prepared	0.8 (0.78±0.005)	28.0 (27.4±1.12)	63.6 (64.8±1.22)	14.1 (13.9±0.34)
	Irradiated	0.69 (0.69±0.002)	12.7 (12.23±0.5)	40.0 (39.8±0.23)	3.5 (3.37±0.15)
Conventional	As-prepared	0.79 (0.78±0.008)	28.38 (28.4±0.15)	65.9 (66.9±0.82)	14.8 (14.9±0.14)
	Irradiated	0.62 (0.61±0.02)	8.9 (7.9±1.4)	31.6 (31.1±0.48)	1.8 (1.52±0.068)

The average parameters of 3-4 devices are presented in brackets.

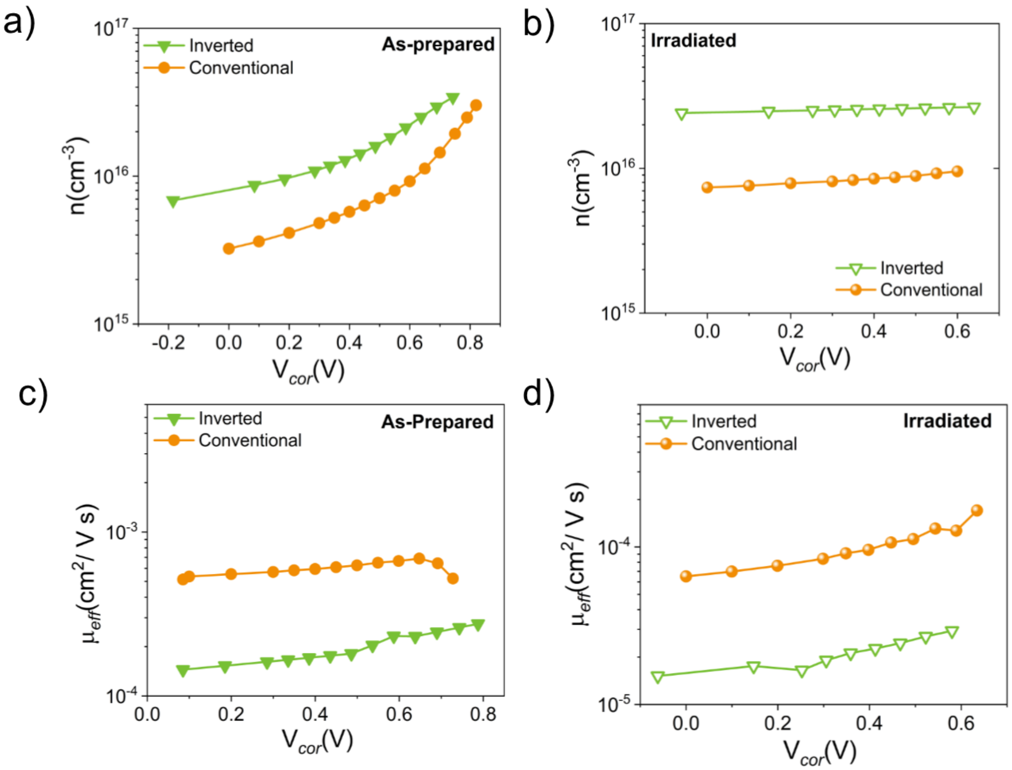

Figure 4.5 a) Charge carrier concentration n of as-prepared devices b) Charge carrier concentration n of irradiated devices the effective mobility of charge carriers c) as-prepared devices d) irradiated devices.

Impedance-voltage spectroscopy was used in order to determine the charge carrier density as well as the effective mobility of charge carriers before and after proton irradiation. The dependency of charge carrier concentration on the corrected voltage is shown in **Figure 4.5 a and b**, respectively, for both the as-prepared and the irradiated devices. By increasing the DC bias that is applied to the as-prepared device in both structures, the density of charge carriers are increased. The photo-generated charge carriers are driven to separate as a result of the simultaneous exponential charge injection and the reduction of the internal electric field [93]**.** Compared to inverted architecture, conventional structure shows a higher charge carrier density in the as-prepared device, leading to better photovoltaic performance.

Under forward bias, the irradiated devices yielded the minor change of charge carrier concentration from 0 V to V_{OC}. The irradiated inverted devices resulted in higher charge carrier concentration than conventional devices.The effective mobility of charge carriers in the irradiated devices was decreased in both structure due to proton irradiation.

4.2.3 Material characterization of transport layers

Both the as-prepared and the irradiated devices have been tested to an analysis of the photovoltaic properties and recombination loss in conventional and inverted structure. Due to the fact that the active layer and electrode are identical in both architectures, it is necessary to analyse the characteristics of the transport layers, such as structural and optical properties, in order to identify the differences in PV performance and recombination loss for each structure.

Structural Characterization

The crystallinity and phase of thin film, which serve a huge role in terms of mobility of charge carriers and work function, can be identified through interpretation of diffraction patterns.The structural features of functional layers such as ZnO, MoOx, Ag, PEDOT:PSS, and ITO were characterized using Grazing Incident X-ray Diffraction as shown in **Figure 4.6**. For ZnO thin film, the grazing incident angle was at 0.3° degree. As prepared ZnO thin film shows the intense peaks at planes as (100) and (002), and (101) with low intensity and weakly observable, identified as hexagonal phase corresponding to JCPDS no. 36-1451[134]. As-prepared ZnO thin film presents the pure nanocrystalline ZnO based on diffraction patterns. The GIXRD pattern of $\mathrm{MoO_x}$ the thin film exhibited no obvious peaks of crystalline $\mathrm{MoO_x}$. Due to room temperature deposition of $\mathrm{MoO_x}$, $\mathrm{MoO_x}$thin film showed the amorphous structure in diffraction pattern and corresponded to the following work [135,136].The diffraction pattern of Ag thin film indicates the (111) plane with high intensity and relatively small intensity of (200) plane ; it corresponds to PDF NO.41-1104 [137].

The irradiated ZnO and $\mathrm{MoO_x}$ thin films yield no peaks in diffraction patterns, thus the structure of thin films transformed to the amourphous structure [138]. Interestingly,proton irradiation creates radiation-induced defects in ZnO thin film, thus it disorders the crystallinity resulting in amourphous structure. In contrast, the irradiated Ag thin films reveal the plane (111) at 2 θ =34.8 with reduced intensity which implies the change the phase transformation due to the knock-on process [137]. Additionally, the irradiated Ag thin film has no (200) plane identyfing the disorder in crystallinity. The stable structural characteristics under proton irradiation exhibited by ITO and PEDOT:PSS thin films shown in **Figure 4.6 d and e**.

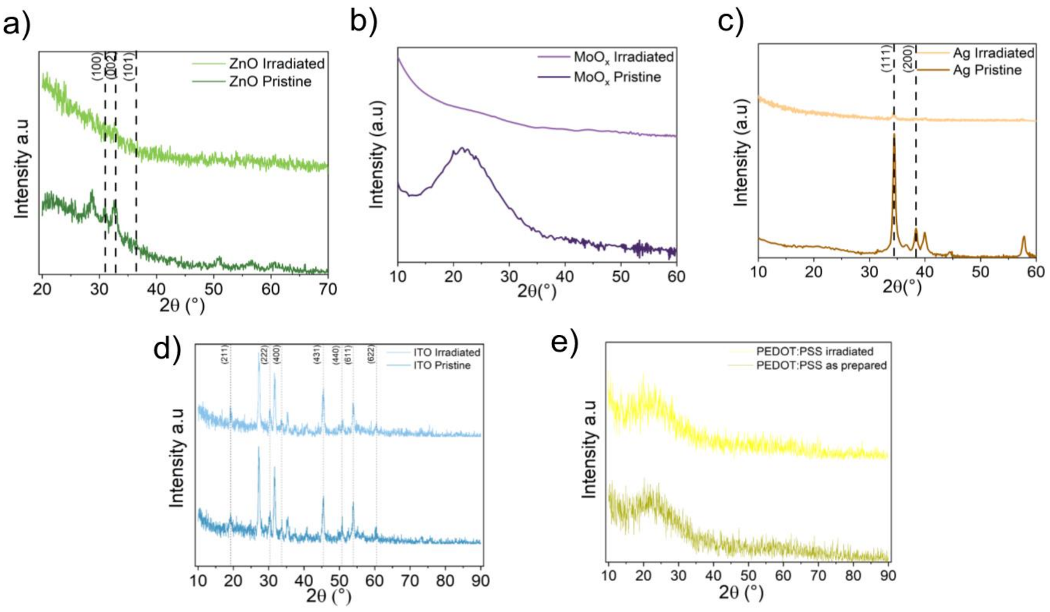

Figure 4.6. a) GIXRD spectra of ZnO as-prepared and irradiated b) GIXRD spectra of MoOx thin films as-prepared and irradiated c) GIXRD spectra of Ag thin films as-prepared and irradiated d) sheet resistance of thin films ITO and e) PEDOT:PSS for as-prepared and irradiated thin films.

Optical Characterization

Transmission parameter is an essential requirement for ETL and HTL in OSC in order to improve the light absorption by the active layer. Spectroscopic ellipsometry was used to evaluate transmission before and after proton irradiation in the 200–2500 nm region in order to determine the influence of proton radiation on the transmission of ETL, HTL, and ITO. **Figure 4.7** displays the transmission spectra of thin films including PEDOT:PSS, PDINN, ZnO, MoOx, and, as a function of wavelength. Among all thin films, ZnO and ITO thin films show negligible shifts in transmission value in the visible range. Proton irradiation causes no significant alteration in the other thin layers. The transmission of a glass substrate is known to decrease noticeably when it is exposed to irradiation with 69 MeV protons, and this exposes the penetration depth of protons to be around 1 mm [32,34]. However, due to the shallow penetration depth, the glass that has been irradiated with low energy protons such as 250 KeV and the glass exposed with 150 KeV lack any observable influence on transmission [139].

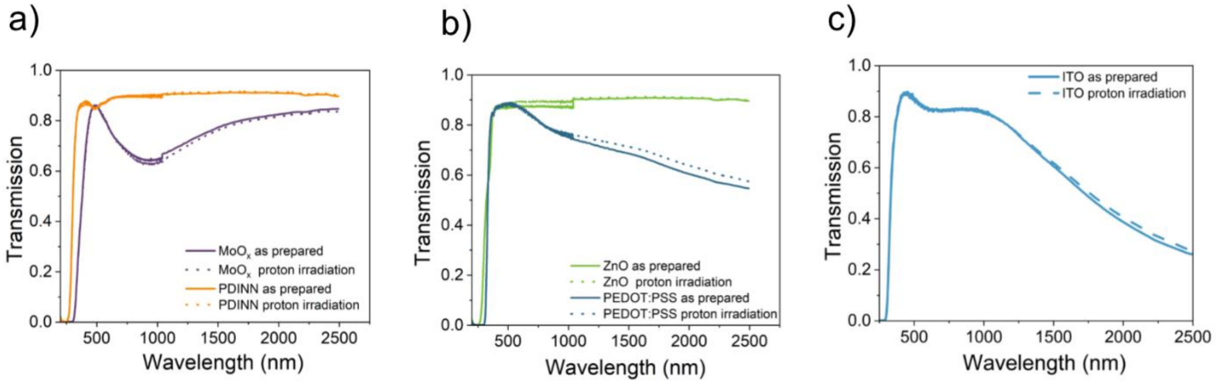

Figure 4.7 Transmittance measurements of a) MoOx and PDINN, b) ZnO and PEDOT:PSS , c) ITO .

Surface Morphology

Figure 4.8 displays surface images of ZnO and Ag thin films, both as-prepared and after proton irradiation. Spin-coating deposition is used for the deposition of ZnO thin films, while a thermal evaporator deposits Ag thin films. As-prepared ZnO thin film reveals multiple hole-shaped surfaces; however, the proton irradiation smooth those hole-shaped surfaces, and the surface became homogenous. Ag thin films deposited by thermal evaporators reveal the grains of different sizes in the as-prepared thin films. However, proton irradiation alters the size of grains in Ag thin films, leading to the unification of some small, coarse particles into grains. GIXRD measurements confirm this observation, indicating a shift in crystallinity into amorphous Ag thin films. The beam impulse of low-energy protons heat the surface of thin films, leading to alteration in structural properties, as observed in GIXRD measurements. There were no modifications observed on the surface of the remaining thin films, which included PEDOT:PSS, PDINN, MoOx, and ITO thin films, when they were exposed to proton irradiation as shown in **Figure 4.9-4.10**.

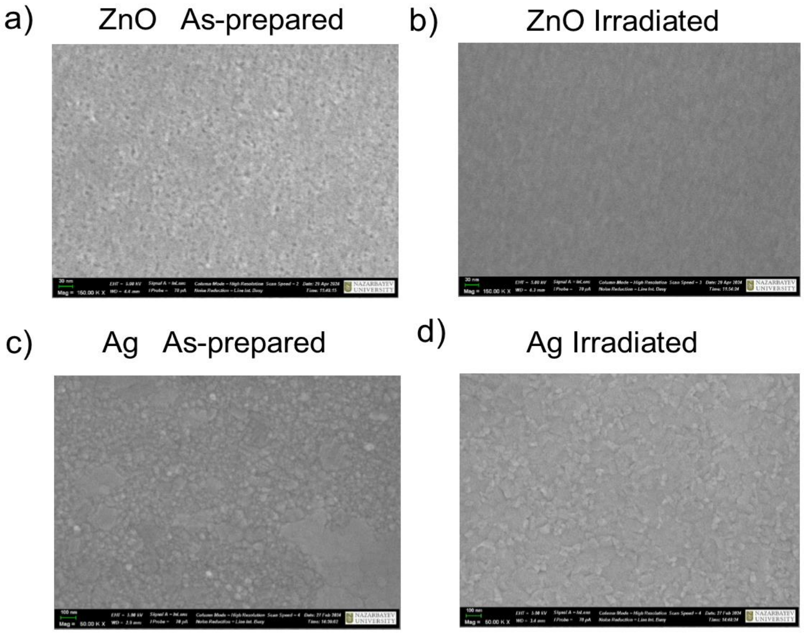

Figure 4.8. SEM image of the surface of the as-prepared and irradiated ZnO and Ag thin films.

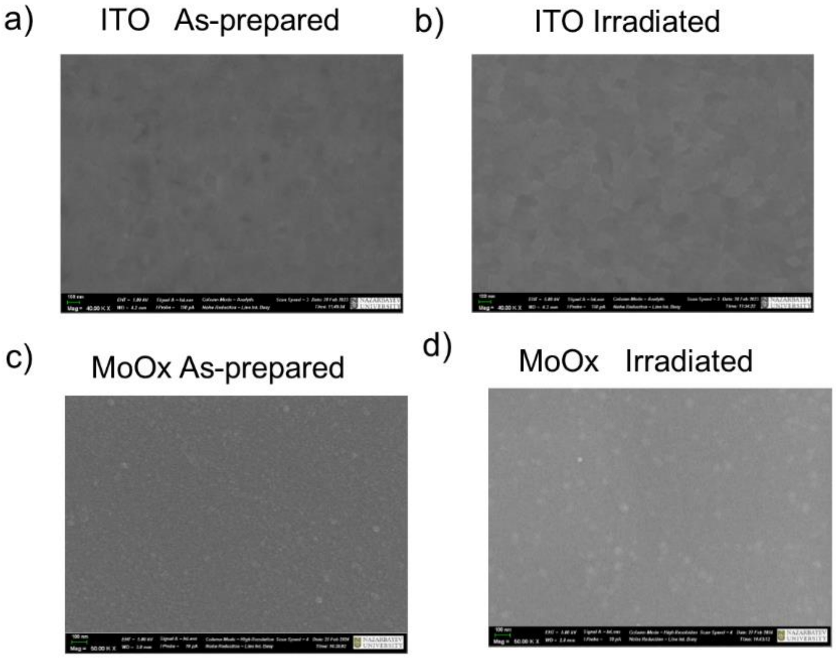

Figure 4.9 SEM images a) MoOx as prepared b) the irradiated MoOx c) ITO as prepared d) the irradiated ITO.

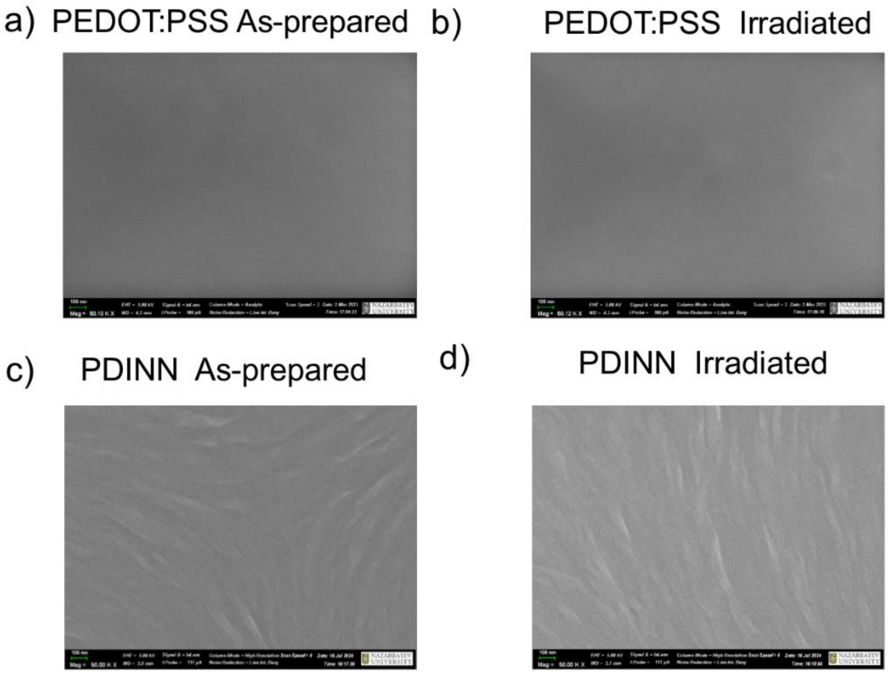

Figure 4.10 SEM images of PDINN and PEDOT:PSS thin film for as-prepared and irradiated.

4.4 Experimental section

Fabrication of organic solar cells

The organic solar cells were fabricated in an inverted device structure as Glass/ITO/ZnO/PM6:Y6/MoOx/Ag and conventional structure as Glass/ITO/PEDOT:PSS/PM6:Y6/PDINN/Ag. The glass/ITO substrates were cleaned with soap and sonicated in distilled water, acetone, and isopropyl alcohol for 15 min. For the conventional device structure, we cleaned a bottom contact PEDOT:PSS with filters 0.45 um and spin-coated it at 4000 rpm for 15 s in air. The glass/ITO/PEDOT:PSS was annealed at 150 °C for 20 min and subsequently transferred to a nitrogen glovebox. The active layer PM6:Y6 with thickness 100 nm (17.6 mg/mL, 1:1.2 D/A mass ratio in chloroform with 0.5% chloronaphthalene) was deposited on the top of PEDOT:PSS by spin coating at 3000 and 3600 rpm, respectively, for 30 s inside the glovebox. Then Glass/ITO/PEDOT/PSS/PM6:Y6 samples were annealed on the hot plate inside the glovebox at 110 °C for 10 min. In the next step, a methanol solution of CIMs (PDINN) was added to the active layer at a concentration of 1.0 mg mL^{-1} and spun at 3000 rpm for 30 seconds.

A thermal evaporation system deposited the electrode, Ag (120 nm), under vacuum deposition at pressure10^{-6}. The solar cell has an active area of 0.1 cm^2, and we used a mask with an active area of 0.0512 $cm^2$for our measurements.

4.5 Supplementary Information

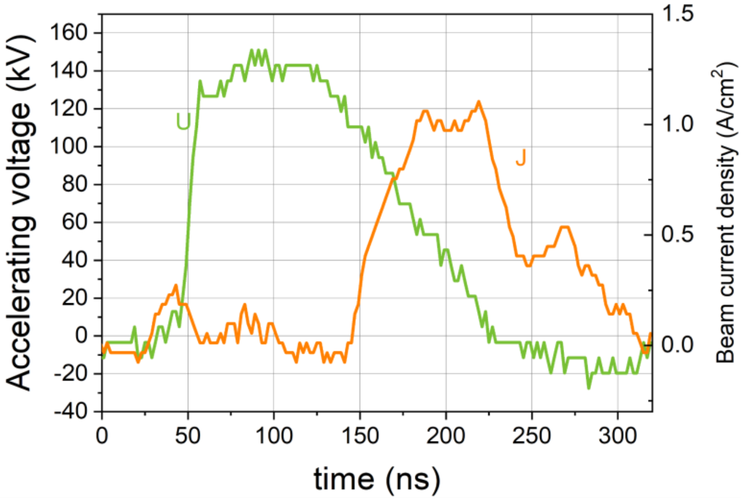

Figure S4.1 The accelerator characteristics used in the current work : Accelerating voltage and beam current density.

Table S1. The series resistance parameter of OSC.

Device Type	Inverted		Conventional	
Treatment	As prepared	Irradiated	As prepared	Irradiated
R_S (ohm cm^2)	4.9 (4.56±0.38)	18.78 (20.26±1.5)	4.08 (4.09±0.23)	31.7 (31.7±0.01)

Chapter 5 The effect of electron irradiation on TiN thin films properties deposited on Quartz and Sapphire Substrates

5.1 Introduction

Space electronics indeed involves a complex interplay of various materials such as semiconductor, insulator and conductor. The design and integration of these materials to space electronics must account the harsh conditions of space, including radiation, temperature extremes, and vacuum, to ensure reliability and functionality in space missions. The impact of high-energy particles on space electronics leads to the breaking of chemical bounds within materials and changes their structural and morphological properties [140,141]. In semiconductor materials, radiation produces a significant amount of nonequilibrium electron-hole pairs, which impairs the functionality of optoelectronic devices by changing their optical and electrical characteristics [142,143]. The main physical process in material structure originating from radiation is the displacement of atoms within the lattice, which results in the formation of defects and dislocations[144]. This causes the charge carrier flow to become distorted, which eventually results in current leakage within the device [140,144,145]. The intricate mechanism of space electronics and the space environment need radiation-resistant materials, not just for semiconductors but also for functional materials such as transport layers and electrodes[146,147].Titanium nitride has unique physiochemical and a wide bandgap characteristics which is the promising candidatesfor space technology. TiN thin film possesses a unique capacity to operate as semiconductor and electrode for electronic applications, in addition to possessing remarkable mechanical qualities. Due to the outstanding thermal, optical and electrical properties, TiN thin films is a potential candidate for photovoltaic, nuclear energy, and battery[148,149].

According to the work, cumulative damaging effects to space technology arose from trapped electrons rather than other sources. From a scientific and commercial viewpoint, it is necessary to understand the degradation mechanism of titanium nitride (TiN) thin film properties used in optoelectronic devices under electron radiation. With this motivation, here, we investigated the radiation resistance of electrical, optical, and structural properties of TiN thin films deposited on quartz and sapphire substrates.

5.2 Results and Discussion

5.2.1 TiN thin film deposition

We use DC reactive magnetron sputtering to deposit TiN thin film on substrates as quartz and sapphire (c-0001). Ti - target and N-gas (4.8×10^{-3} mbar) were used along with an annealing substrate holder (300°C) and 120 W of power to deposit a 90-nm-thick TiN thin film, and thickness of TiN thin film shown in **Figure 5.1.**

Electron irradiation was conducted at the Institute of Nuclear Physics in Almaty, Kazakhstan, employing the ILU-10 linear accelerator. The electron energy was adjusted to 5 MeV, achieving a total fluence of 7×10^{13} e/cm^2. The electron fluence were measured using GEZ B6001 polystyrene calorimeters and GEX B3002 film dosimeters [150].

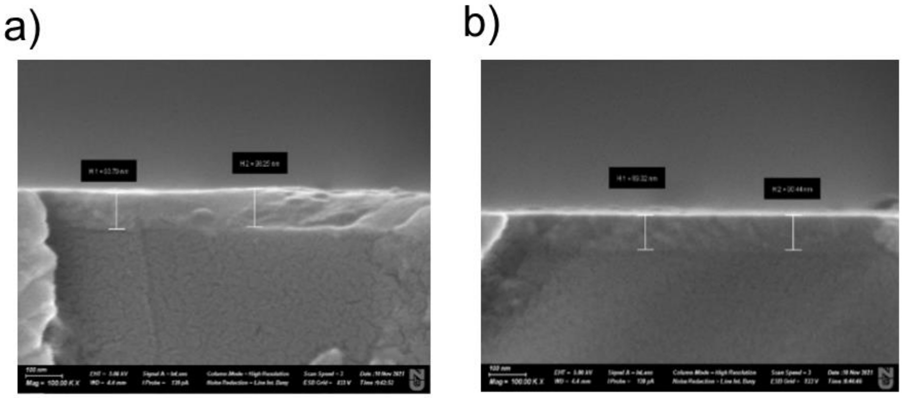

Figure 5.1. Cross section SEM image of thickness TiN: a) before irradiation and b) after irradiation.

5.2.2 Structural analysis

To evaluate the impact of electron irradiation on TiN thin film's crystalline structure, diffraction pattern measurements were performed using the GIXRD system both pre and post-irradiation. In the case of magnetron sputtering, the crystalline structure of the thin film is mostly constructed by the substrate's crystallinity and the deposition conditions. The as prepared TiN thin films deposited on c-(0001) plane sapphire substrate revealed a polycrystalline structure, featuring the (111), (200), (220), and (222) planes, which corresponds to literature[151], as illustrated in Figure 5.2. In contrast, the diffraction pattern of TiN films fabricated on quartz showed the (200) plane, corresponding to prior research [150,152]. At post-irradiation treatment, the crystallinity of TiN on quartz substrates exhibited a peak at 40°, corresponding to the (111) plane with the highest intensity, and another peak at 44° identified as the (200) plane. Moreover, a peak around 53° in the diffraction pattern can indicate the various crystallographic phases, with two possible versions being hexagonal close-packed (hcp) titanium (COD ID 9011600) and anatase titanium oxide correspondes to (ICSD:172914). Based on the results of the diffraction pattern findings , high-energy electron bombardment caused lattice defects and crystallographic disorder in the TiN thin films deposited on sapphire and quartz. Additionally, electron exposure appeared to produce new peaks attributed to vacancies and interstitials, resulting in a phase transition observed in the TiN films fabricated on quartz.

Grain size analysis based on the diffraction patterns of the TiN thin films are represented in **Table 5.1**.The limitations encountered during the thin film deposition process affect grain size and crystallinity, leading to various texture modifications and shifts in diffraction angles. The disorder levels in TiN thin films on sapphire and quartz prior to irradiation varied significantly, mainly due to differences in grain sizes across various planes. The grow of grain size under high-energy electron exposure is affected by phase transitions from crystalline to amorphous states due to the electron knock-on mechanism[153]. This mechanism generates an electrostatic force through the polarization of atoms and ions caused by electron exposure, which promotes the movement of free atoms and ions, thereby aiding in the absorption and dissolution of nanograins [154]. Previous studies have indicated that a significant consequence of this type of irradiation is an increase in entropy and a shift in Gibbs free energy, that might potentially cause changes in texture and modifications in diffraction angles[155] .

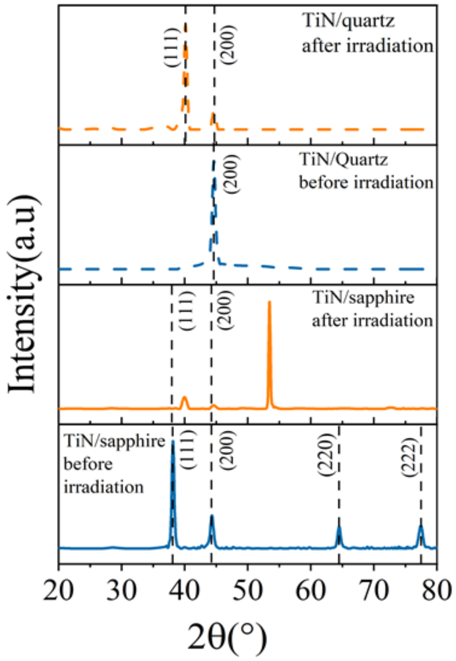

Figure 5.2. Diffraction pattern analysis of TiN thin films deposited on quartz and sapphire: pre- and post-irradiation.

Table 5.1. Grain sizes determined using the Scherrer equation utilizing the measured diffraction patterns of the TiN.

Name	**2 theta**	**FWHM**	**D (grain size in nm)**	**Cps**	**Plane**
TiN/quartz before	44.58	0.57	15.82	351	200
TiN/quartz after	44.67	0.48	19.47	35	200
TiN/sapphie before	38.086	0.42	20.91	157	111
TiN/sapphie after	39.88	0.37	23.87	94	111

5.2.3 Surface analysis

The surface of thin film dictates the interfacial loss in optoelectronic devices. The surface of TiN thin film is characterized by AFM in order to determine the RMS parameter. **Figure 5.3** presents the topogpahy images of TiN thin films in size 5 μm ·5 μm before and after irradiation. As explained earlier, during the deposition process some level of disorder existed due to the surface of substrates which also affects the surface of TiN thin film. The RMS parameter of as-prepared TiN thin film deposited on sapphire is 5.18 nm higher than TiN thin film on quartz with 0.68 nm. In case of irradiated TiN thin films deposited on sapphire, RMS is decreased by 2 times. The opposite effect of electron irradiation is observed in TiN thin films on quartz revealing the increase of RMS to 0.23 nm. Interestingly, electron irradiation impacted TiN thin film's surface differently depending on the substrate. The images of surface at higher magnification by SEM showed no visible changes before and after irradiation as shown in **Figure 5.4**.

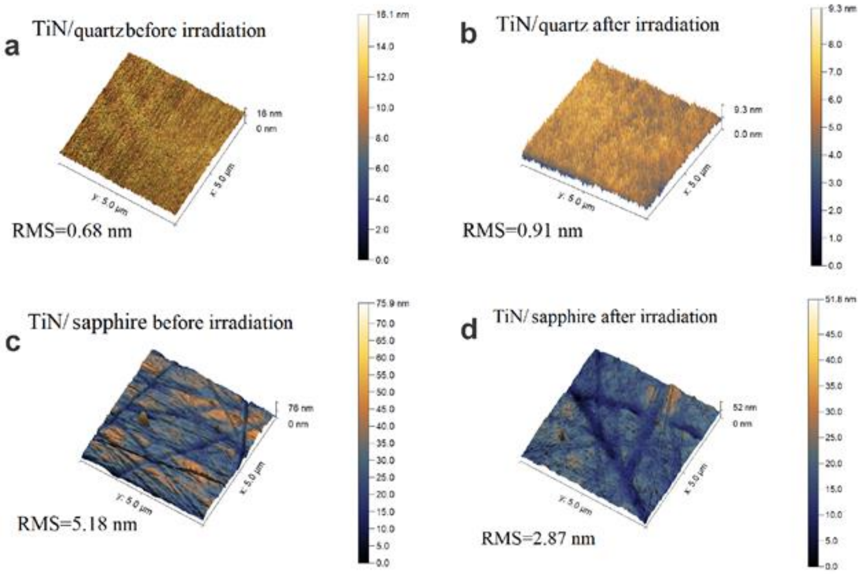

Figure 5.3. Surface topogrophy of TiN thin films for pre and post-irradiation.

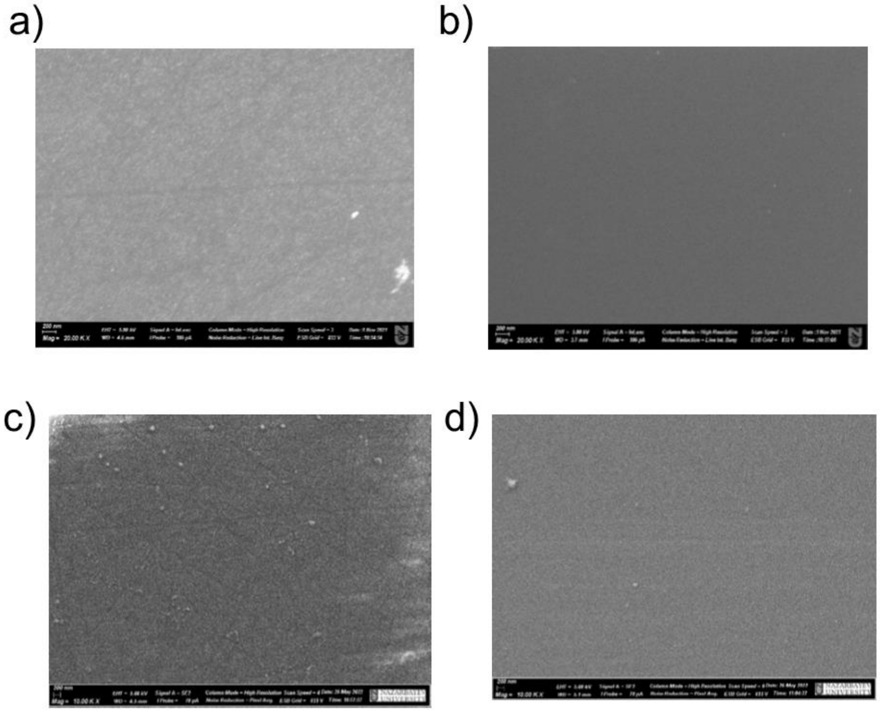

Figure 5.4. SEM image of the TiN thin film’s surface.

5.2.4 Chemical composition analysis

The XPS tool conducted a chemical composition measurement on the TiN thin film to evaluate the effect of electron exposure. TiN thin films grown by magnetron sputtering were exposed to the air, so the surface contamination was cleaned up with argon ions (etching process). As shown in **Figure 5.5**, the XPS Ti 2p spectra identified two pairs of spin−orbit splitting of Ti $2p_{3/2}$ and Ti $2p_{1/2}$. The XPS spectra is fitted according to the chemical composition of TiN based on the following reference : Ti−N (454.9 and 460.8 eV), Ti−O−N (456.8 and 462.5 eV), and Ti−O (456.3 and 464.0 eV). The as-prepared TiN thin films showed Ti $2p_{3/2}$ peaks at 454.9 and 454.7 eV, attributed to Ti–N bonding, in quartz and sapphire, respectively. According to works [151,156], TiN thin films demonstrate that, in these systems, shake-up peaks at 462.5 eV (Ti-O-N) and 460.8 eV (Ti-N) arise from broad Ti3d-N2p hybridized states near the Fermi level that enable several transitions to different states. The binding energy of the Ti $2p_{3/2}$ doublet in the spectra of irradiated TiN on sapphire is detected at 455.4 eV, and the full width at half-maximum (FWHM) value is tracted to be 2.6 eV (**Figure 5.5b**), while the irradiated TiN on quartz is shown in **Figure 5.5d**, where the Ti $2p_{3/2}$doublet is located at 454.6 eV (FWHM value of 2.4). Moreover, variations in the relative intensity of Ti 2p peaks are noted in all specimens, correlating with alterations in the crystal structure. Analysis of the Ti $2p_{3/2}$and Ti $2p_{1/2}$peaks after electron irradiation revealed a transformation from Ti−N bonding to Ti−O in the TiN thin films on sapphire. Electron irradiation, however, influenced the TiN thin films formed on quartz by altering the chemical bonds from Ti−N and Ti−O to Ti−O−N, as illustrated in **Figures 5.5 a and b**. This discovery can be ascribed to a complex process involving electrochemical interactions between electrons and component atoms, along with the exchange of subsurface nitrogen with oxygen adatoms [152–154].

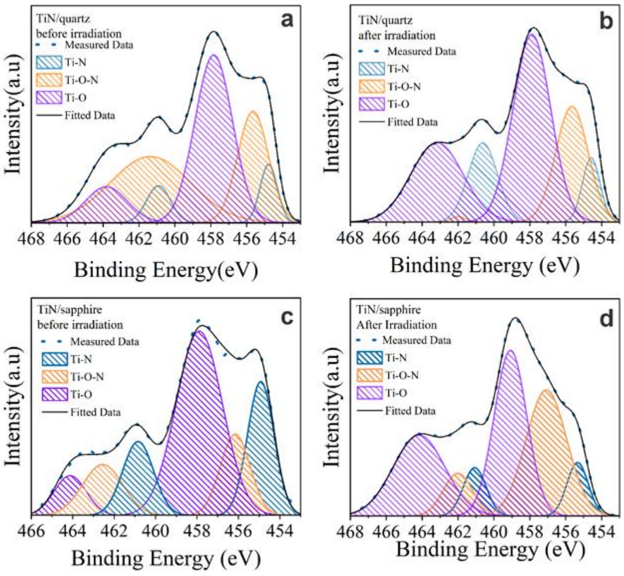

Figure 5.5. The results of chemical composition analysis (XPS spectra) of TiN thin film

5.2.5 Work Function

To quantitively analysis the impact of electron exposure on TiN thin film, UPS technique was employed to measure the work function. The work function of the TiN thin film is calculated from the onset position of measured UPS spectra.The UPS spectra of TiN thin films deposited on quartz and sapphire pre - and post electron exposure are shown in **Figure. 5.6a**. The UPS spectra are enhanced by two with electron irradiation for as-deposited TiN on both substrates.The cut-off energy of the as-prepared TiN is shown to be higher than irradiated TiN thin films on both substrates, presented in **Figure 5.6b**. The UPS spectrum indicated a broad defect band existion after irradiation with a highly dense concentration of localized states under the Fermi level [155].Fermi level pinning and the density of interface states can influence band alignment[157]. TiN thin films on both substrates have a work function a little bigger than 4.2 eV before electron exposure. However, the work function of irradiated TiN is lowered and showed 4.05 eV as the consequence of the change in the density of free charge carriers and surface dipoles as shown in **Figure 5.6d**[158].

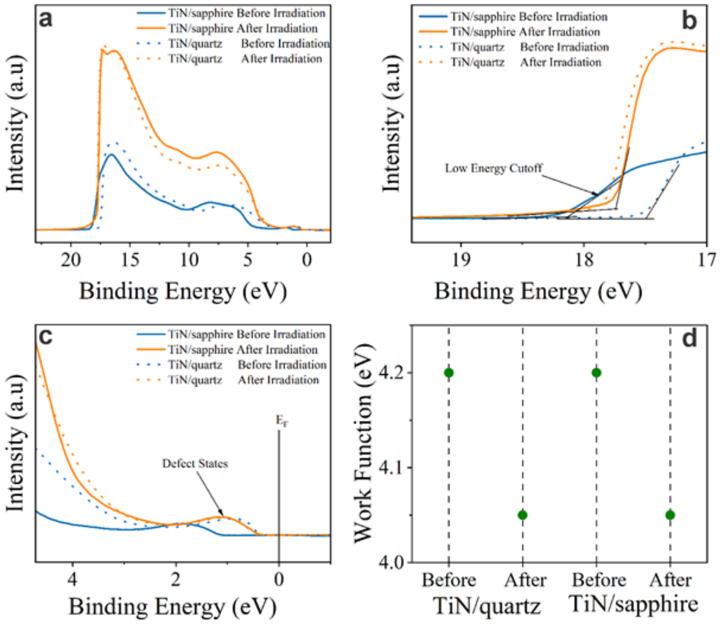

Figure 5.6. UPS spectra and work function analysis of the TiN thin films.

5.2.6 Electrical properties

The van der Pauw technique was employed to measure Hall coefficients of TiN thin films and further identification of the electrical characteristics: Hall mobility, specific conductivity, and charge carrier density. The electrical properties of the as prepared and irradiated TiN thin film are illustrated in **Figure 5.7** identifying the n-type conductivity on the both substrates. The specific combination of titanium and nitrogen atoms enables titanium nitride (TiN) to form metallic and covalent bonds, leading to a high density of free electrons in the conduction band. The source of high-concentration electrons in the conduction band results from thermal activation of energy levels linked with excess titanium atoms[159] . The carrier concentration of TiN thin film post-irradiation increased by two orders of magnitude on quartz and exhibited a modest increase on sapphire substrate. In terms of specific conductivity, the TiN thin film on a sapphire substrate exhibited a major shift from 97 Ω^{-1} cm^{-1} to 228 Ω^{-1} cm^{-1}, while TiN on quartz displayed a minor rise. There is an inverse relationship between charge carrier concentration and mobility in TiN thin films [160]. It was found that the electron mobility in the irradiated TiN thin films on both substrates are decreased. The alteration in electrical properties of TiN thin films can be affected by point defects, implanted atoms and grain boundaries [161] .

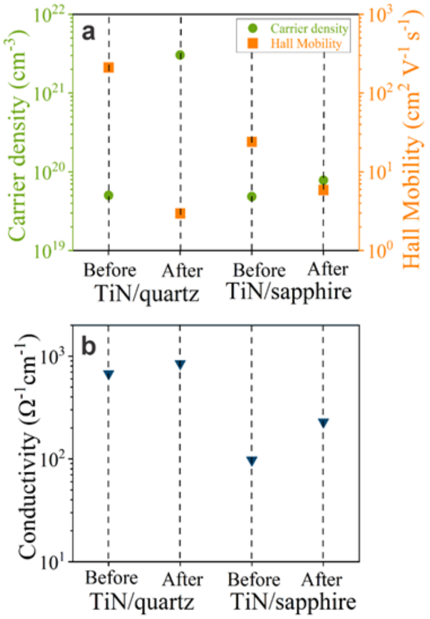

Figure 5.7 The electrical features of TiN thin films.

5.2.7 Optical properties

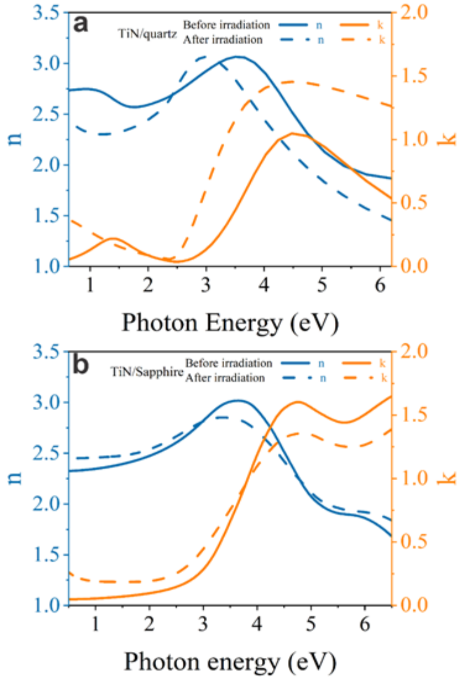

Figure 5.8 Optical properties of TiN as-prepared and irradiated conditions on different substrates: a)quartz and b) sapphire.

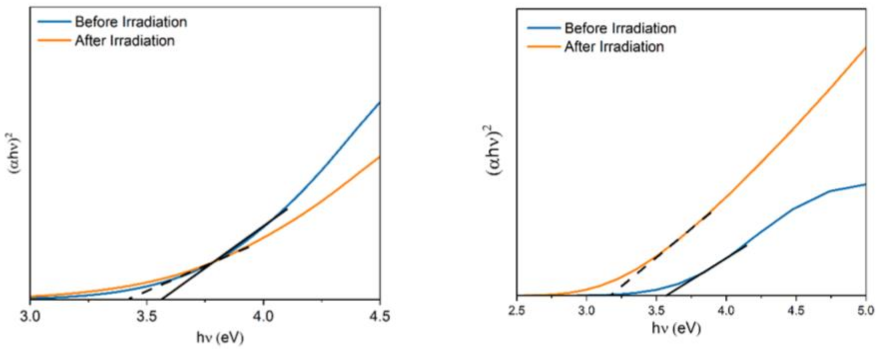

Figure 5.9. Tauc plot of the TiN on sapphire, extrapolated lines to define Energy gap: (a) black line- before irradiation and dashed line –after irradiation, Tauc plot of the TiN on glass (b) , extrapolated lines to define Energy gap: black line- before irradiation and dashed line –after irradiation.

Having examined the effect of electron exposure to TiN thin films deposited on different substrates, Lorentz and Drude dispersion models were applied to fit the Delta and Phi function characteristics measured by spectroscopic ellipsometry. The pre and post-irradiated TiN thin films deposited on quartz remain their forms of extinction coefficients as well as refractive index in the measured range 0.6-6 eV. However, the high energy electron exposure propogates the increase in the extinction coefficient of TiN deposited on quartz at the visible range. The electron exposure propogates the phase transition identified by GIXRD measurements that explaines the increase in extinction coefficient in TiN thin film deposited on quartz. In contrast to the extinction coefficient TiN thin film deposited on quartz, TiN on sapphire revealed totally opposite effect of electron exposure. The extinction coefficient of TiN thin film on sapphire slightly enhanced under electron exposure in the range from 0.6 eV to 3.6 eV photon energy. The interband characteristic of transition is identified in TiN thin films based on the certain shape of extinction coefficient due to the grow of nitrogen p-states and titanium d-states[162]. Even so the electron exposure changed the electroric structure of TiN thin film, the metallic characterics of TiN thin films retained after high energy electron exposure based on 2.7 eV value as shown in **Figure 5.8 a and b**.

The refractive index of TiN on quartz is reduced during electron exposure in the low photon energy range of 0.6-2.5 eV; however, a transition from reduction to an increase in refractive index is observed in the range of 2.5 to 3.1 eV under electron exposure. Compared to low photon energy,the refractive index of the irradiated TiN thin film on quartz is moderately reduced at high energy photon energy range. Due to electron exposure TiN thin film on sapphire, the refractive index changed slightly differently in the whole range of photon energy. Band gap of thin films is important parameter in semiconductor fields based on absorption coefficient using Tauc plot. The Tauc plot is based on the relationship between $(\alpha h\upsilon)^2$ and the incident photon energy, where the extrapolation of the linear segment of the $(\alpha h\upsilon)^2$ against $h\upsilon$ to the photon energy axis determines the band gap value. Band gap of TiN thin film is decreased to 0.1 eV deposited on the sapphire and 0.3 eV on quartz, respectively as shown in **Figure 5.9**.

6 Conclusion

This thesis presents a comprehensive investigation into the performance of OSCs under conditions relevant to space applications, with a particular focus on radiation effects. Radiation exposure, including both electron and proton irradiation, is among the most critical environmental stressors in space. The operational mechanisms of OSCs with varying active layer thicknesses were evaluated using the i-NURA proton accelerator, which provided high-energy proton irradiation at 170 keV with fluences in the range of $1–1.3 \times 10^{12}$ p/cm^2—conditions that approximate three years of operation in LEO. Post-annealing was also conducted to assess recovery effects. Devices with thinner active layers (60 nm) demonstrated superior performance post-irradiation. This enhancement is attributed to reduced bulk trap densities, minimized space-charge accumulation, and improved charge-carrier extraction. Thinner active layers shorten the carrier transport distance, thereby reducing recombination losses and mitigating the impact of radiation-induced trap states. Moreover, they exhibit less field screening and charge accumulation in tail states, which often hinder charge collection in thicker films. These combined factors contribute to the enhanced efficiency and recovery of thinner OSCs after radiation exposure. Based on findings by Prof. Stephen Forrest, proton irradiation primarily affects the C–H bonds in OSCs, given the low atomic mass of carbon and hydrogen. However, displaced hydrogen atoms can reattach to the molecular structure during thermal annealing at temperatures above 45 °C, enabling partial recovery of device performance which corresponds with current research.

A comparative study between inverted and conventional OSC architectures under proton irradiation (170 keV, 1×10^{12} p/cm^2) further highlighted the superior radiation resistance of the inverted structure. Photovoltaic characterization of irradiated devices revealed that inverted OSCs, incorporating inorganic transport layers such as ZnO and MoO_3, exhibit greater resilience compared to conventional devices that employ organic transport layers as PEDOT:PSS and PDINN. This difference is attributed to the higher energy bond of inorganic materials under irradiation. Overall, the results demonstrate that reducing the active layer thickness and employing inverted architectures with inorganic transport layers are effective strategies for enhancing the radiation hardness of OSCs. These insights are crucial for the design and development of lightweight, robust, and efficient OSCs tailored for the challenging conditions of space, thereby underscoring their potential for next-generation photovoltaic applications.

The final part of the thesis explores titanium nitride (TiN) as a potential transparent conductive material due to its excellent thermal, optical, and electrical properties, and its wide bandgap. It was observed that conventional glass substrates undergo significant changes in optical properties under 68 MeV proton irradiation, motivating the research for more stable substrates[32]. Consequently, studying the radiation resistance of TiN deposited on quartz and sapphire substrates under electron irradiation is necessary. TiN films deposited on quartz and sapphire substrates were subjected to electron irradiation at 5 MeV to assess their suitability for space applications. Post-irradiation analyses revealed changes in the structural, optical, and electrical properties of TiN films. Notably, TiN deposited on sapphire exhibited increased specific conductivity after electron exposure, suggesting its promise as a transparent conductive layer for solar cells in space environments.

Limitations

As with any experimental work, certain limitations in the experimental setup are inevitable. For accurate evaluation of solar cell performance, the AM0 solar spectrum—characterized by a total irradiance of 136.7 mW cm^{-2} -should ideally be employed, as it more accurately replicates the solar environment in space, where ultraviolet radiation is more intense and atmospheric scattering and absorption are absent. However, in this study, the AM1.5 solar spectrum with an irradiance of 100 mW cm^{-2} was utilized to assess the radiation resistance of organic photovoltaic (OPV) devices. This deviation was due to technical constraints that prevented the implementation of an AM0 testing setup. Additionally, challenges with the X-ray Photoelectron Spectroscopy (XPS) equipment and the INURA accelerator limited the scope of chemical composition and surface analysis of the transport layers, thereby restricting the depth of the characterization in this aspect.

Future Work

Following the evaluation of ionizing radiation resilience in organic photovoltaic (OPV) devices, the next critical aspect for space qualification is the assessment of thermal stability through thermal cycling tests. One of the key challenges in establishing the experimental setup is the requirement for co-location of ionizing radiation facilities, thermal cycling equipment, and fabrication laboratories within the same building. This logistical constraint is essential to minimize sample degradation due to environmental exposure during transport and to ensure consistency and accuracy in performance measurements.

References

1. Solar Arrays on the International Space Station - NASA https://www.nasa.gov/image-article/solar-arrays-international-space-station-2/.

2. Phillips 66, China University of Technology, and Solarmer Energy Set a World Record in Solar Power Conversion Efficiency evwind.

3. Giorgia Burzachechi Organic solar panels: a flexible and sustainable future for renewable energy.

4. Transmission Electron Microscopy | Nanoscience Instruments https://www.nanoscience.com/techniques/transmission-electron-microscopy/.

5. Akyildiz, I.F., and Kak, A. (2019). The Internet of Space Things/CubeSats. IEEE Netw. *33*, 212–218. https://doi.org/10.1109/MNET.2019.1800445.

6. Satellite Database | Union of Concerned Scientists https://www.ucsusa.org/resources/satellite-database.

7. What is a satellite? - NASA https://www.nasa.gov/general/what-is-a-satellite/.

8. Look Up Space Reports More Than 10,000 Active Satellites in Orbit - SpaceWatch.GLOBAL https://spacewatch.global/2024/06/look-up-space-reports-more-than-10000-active-satellites-in-orbit/.

9. Kuwano, Y., Nakano, S., and Tsuda, S. (1991). Recent progress in Si thin film technology for solar cells. In International Conference on Thin Film Physics and Applications (SPIE), pp. 200–209. https://doi.org/10.1117/12.47302.

10. Bouisset, P., Nguyen, V.D., Akatov, Y.A., Siegrist, M., Parmentier, N., Archangelsky, V.V., Vorojtsov, A.S., Petrov, V.M., and Kovalev, E.E. (1992). Quality factor and dose equivalent investigations aboard the Soviet space station MIR. Adv. Space Res. *12*, 363–367. https://doi.org/10.1016/0273-1177(92)90130-P.

11. Messenger, S.R., Burke, E.A., Walters, R.J., Warner, J.H., and Summers, G.P. (2005). Using SRIM to calculate the relative damage coefficients for solar cells. Prog. Photovolt. Res. Appl. *13*, 115–123. https://doi.org/10.1002/pip.608.

12. Moon, S., Kim, K., Kim, Y., Heo, J., and Lee, J. (2016). Highly efficient single-junction GaAs thin-film solar cell on flexible substrate. Sci. Rep. *6*, 30107. https://doi.org/10.1038/srep30107.

13. Iles, P.A., Yeh, Y.-C.M., Ho, F.H., Chu, C.-L., and Cheng, C. (1990). High-efficiency (>20% AM0) GaAs solar cells grown on inactive-Ge substrates. IEEE Electron Device Lett. *11*, 140–142. https://doi.org/10.1109/55.61775.

14. Yamaguchi, M., Lee, K., Araki, K., Kojima, N., Yamada, H., and Katsumata, Y. (2018). Analysis for efficiency potential of high-efficiency and next-generation solar cells. Prog. Photovolt. Res. Appl. *26*, 543–552. https://doi.org/10.1002/pip.2955.

15. Tobin, S.P., Vernon, S.M., Bajgar, C., Wojtczuk, S., Melloch, M.R., Keshavarzi, A., Stellwag, T.B., Venkatensan, S., Lundstrom, M., and Emery, K.A. (1990). Assessment of MOCVD- and MBE-growth GaAs for high-efficiency solar cell applications. IEEE Trans. Electron Devices *37*, 469–477. https://doi.org/10.1109/16.46385.

16. Guter, W., Schöne, J., Philipps, S.P., Steiner, M., Siefer, G., Wekkeli, A., Welser, E., Oliva, E., Bett, A.W., and Dimroth, F. (2009). Current-matched triple-junction solar cell reaching 41.1% conversion efficiency under concentrated sunlight. Appl. Phys. Lett. *94*, 223504. https://doi.org/10.1063/1.3148341.

17. Geisz, J.F., Kurtz, S., Wanlass, M.W., Ward, J.S., Duda, A., Friedman, D.J., Olson, J.M., McMahon, W.E., Moriarty, T.E., and Kiehl, J.T. (2007). High-efficiency GaInP⁄GaAs⁄InGaAs triple-junction solar cells grown inverted with a metamorphic bottom junction. Appl. Phys. Lett. *91*, 023502. https://doi.org/10.1063/1.2753729.

18. – Home - AZUR SPACE Solar Power GmbH https://www.azurspace.com/index.php/en/.

19. Space Solar Cells CESI. https://www.cesi.it/space-solar-cells/.

20. Spectrolab https://www.spectrolab.com/.

21. Li, J., Aierken, A., Liu, Y., Zhuang, Y., Yang, X., Mo, J.H., Fan, R.K., Chen, Q.Y., Zhang, S.Y., Huang, Y.M., et al. (2021). A Brief Review of High Efficiency III-V Solar Cells for Space Application. Front. Phys. *8*, 631925. https://doi.org/10.3389/fphy.2020.631925.

22. Dimroth, F., Tibbits, T.N.D., Niemeyer, M., Predan, F., Beutel, P., Karcher, C., Oliva, E., Siefer, G., Lackner, D., Fus-Kailuweit, P., et al. (2016). Four-Junction Wafer-Bonded Concentrator Solar Cells. IEEE J. Photovolt. *6*, 343–349. https://doi.org/10.1109/JPHOTOV.2015.2501729.

23. Geisz, J.F., France, R.M., Schulte, K.L., Steiner, M.A., Norman, A.G., Guthrey, H.L., Young, M.R., Song, T., and Moriarty, T. (2020). Six-junction III–V solar cells with 47.1% conversion efficiency under 143 Suns concentration. Nat. Energy *5*, 326–335. https://doi.org/10.1038/s41560-020-0598-5.

24. Rehman, A.U., Lee, S.H., and Lee, S.H. (2016). Silicon space solar cells: progression and radiation-resistance analysis. J. Korean Phys. Soc. *68*, 593–598. https://doi.org/10.3938/jkps.68.593.

25. Hamache, A., Sengouga, N., Meftah, A., and Henini, M. (2016). Modeling the effect of 1MeV electron irradiation on the performance of n+–p–p+ silicon space solar cells. Radiat. Phys. Chem. *123*, 103–108. https://doi.org/10.1016/j.radphyschem.2016.02.025.

26. Jianmin, H., Yiyong, W., Jingdong, X., Dezhuang, Y., and Zhongwei, Z. (2008). Degradation behaviors of electrical properties of GaInP/GaAs/Ge solar cells under <200keV proton irradiation. Sol. Energy Mater. Sol. Cells *92*, 1652–1656. https://doi.org/10.1016/j.solmat.2008.07.017.

27. Chacon, S.A., Khanal, M.N., Durant, B.K., Afshari, H., Byers, T.A., Parashar, M., Rout, B., Whiteside, V.R., Poplavskyy, D., and Sellers, I.R. (2024). Probing the Interfacial Properties of ACIGS Solar Cells with Targeted Proton Irradiation. Sol. RRL *8*, 2300756. https://doi.org/10.1002/solr.202300756.

28. Kasap, S., and Capper, P. (2007). Springer Handbook of Electronic and Photonic Materials (Springer Science & Business Media).

29. Guo, Z., Jena, A.K., Kim, G.M., and Miyasaka, T. (2022). The high open-circuit voltage of perovskite solar cells: a review. Energy Environ. Sci. *15*, 3171–3222. https://doi.org/10.1039/D2EE00663D.

30. Kim, J.Y., Lee, J.-W., Jung, H.S., Shin, H., and Park, N.-G. (2020). High-Efficiency Perovskite Solar Cells. Chem. Rev. *120*, 7867–7918. https://doi.org/10.1021/acs.chemrev.0c00107.

31. Li, D., Zhang, D., Lim, K.-S., Hu, Y., Rong, Y., Mei, A., Park, N.-G., and Han, H. (2021). A Review on Scaling Up Perovskite Solar Cells. Adv. Funct. Mater. *31*, 2008621. https://doi.org/10.1002/adfm.202008621.

32. Lang, F., Nickel, N.H., Bundesmann, J., Seidel, S., Denker, A., Albrecht, S., Brus, V.V., Rappich, J., Rech, B., Landi, G., et al. (2016). Radiation Hardness and Self-Healing of Perovskite Solar Cells. Adv. Mater. *28*, 8726–8731. https://doi.org/10.1002/adma.201603326.

33. Brus, V.V., Lang, F., Bundesmann, J., Seidel, S., Denker, A., Rech, B., Landi, G., Neitzert, H.C., Rappich, J., and Nickel, N.H. (2017). Defect Dynamics in Proton Irradiated CH3NH3PbI3 Perovskite Solar Cells. Adv. Electron. Mater. *3*, 1600438. https://doi.org/10.1002/aelm.201600438.

34. Lang, F., Jošt, M., Frohna, K., Köhnen, E., Al-Ashouri, A., Bowman, A.R., Bertram, T., Morales-Vilches, A.B., Koushik, D., Tennyson, E.M., et al. (2020). Proton Radiation Hardness of Perovskite Tandem Photovoltaics. Joule *4*, 1054–1069. https://doi.org/10.1016/j.joule.2020.03.006.

35. Kirmani, A.R., Byers, T.A., Ni, Z., VanSant, K., Saini, D.K., Scheidt, R., Zheng, X., Kum, T.B., Sellers, I.R., McMillon-Brown, L., et al. (2024). Unraveling radiation damage and healing mechanisms in halide perovskites using energy-tuned dual irradiation dosing. Nat. Commun. *15*, 696. https://doi.org/10.1038/s41467-024-44876-1.

36. Boldyreva, A.G., Akbulatov, A.F., Tsarev, S.A., Luchkin, S.Yu., Zhidkov, I.S., Kurmaev, E.Z., Stevenson, K.J., Petrov, V.G., and Troshin, P.A. (2019). γ-Ray-Induced Degradation

in the Triple-Cation Perovskite Solar Cells. J. Phys. Chem. Lett. *10*, 813–818. https://doi.org/10.1021/acs.jpclett.8b03222.

37. Yang, S., Xu, Z., Xue, S., Kandlakunta, P., Cao, L., and Huang, J. (2019). Organohalide Lead Perovskites: More Stable than Glass under Gamma-Ray Radiation. Adv. Mater. *31*, 1805547. https://doi.org/10.1002/adma.201805547.

38. Miyazawa, Y., Ikegami, M., Chen, H.-W., Ohshima, T., Imaizumi, M., Hirose, K., and Miyasaka, T. (2018). Tolerance of Perovskite Solar Cell to High-Energy Particle Irradiations in Space Environment. iScience *2*, 148–155. https://doi.org/10.1016/j.isci.2018.03.020.

39. Miyazawa, Y., Ikegami, M., Miyasaka, T., Ohshima, T., Imaizumi, M., and Hirose, K. (2015). Evaluation of radiation tolerance of perovskite solar cell for use in space. In 2015 IEEE 42nd Photovoltaic Specialist Conference (PVSC), pp. 1–4. https://doi.org/10.1109/PVSC.2015.7355859.

40. Paternò, G.M., Robbiano, V., Santarelli, L., Zampetti, A., Cazzaniga, C., Garcìa Sakai, V., and Cacialli, F. (2019). Perovskite solar cell resilience to fast neutrons. Sustain. Energy Fuels *3*, 2561–2566. https://doi.org/10.1039/C9SE00102F.

41. Kirmani, A.R., Ostrowski, D.P., VanSant, K.T., Byers, T.A., Bramante, R.C., Heinselman, K.N., Tong, J., Stevens, B., Nemeth, W., Zhu, K., et al. (2023). Metal oxide barrier layers for terrestrial and space perovskite photovoltaics. Nat. Energy *8*, 191–202. https://doi.org/10.1038/s41560-022-01189-1.

42. Ho-Baillie, A.W.Y., Sullivan, H.G.J., Bannerman, T.A., Talathi, Harsh.P., Bing, J., Tang, S., Xu, A., Bhattacharyya, D., Cairns, I.H., and McKenzie, David.R. (2022). Deployment Opportunities for Space Photovoltaics and the Prospects for Perovskite Solar Cells. Adv. Mater. Technol. *7*, 2101059. https://doi.org/10.1002/admt.202101059.

43. Starlink satellites: Facts, tracking and impact on astronomy | Space https://www.space.com/spacex-starlink-satellites.html.

44. Koetsier, J. (2020). Elon Musk’s 42,000 StarLink Satellites Could Just Save The World. John Koetsier. https://johnkoetsier.com/elon-musks-42000-starlink-satellites-could-just-save-the-world/.

45. Staff, A. (2020). Amazon receives FCC approval for Project Kuiper satellite constellation. https://www.aboutamazon.com/news/company-news/amazon-receives-fcc-approval-for-project-kuiper-satellite-constellation.

46. UK government secures satellite network OneWeb GOV.UK. https://www.gov.uk/government/news/uk-government-secures-satellite-network-oneweb.

47. Kaltenbrunner, M., Adam, G., Głowacki, E.D., Drack, M., Schwödiauer, R., Leonat, L., Apaydin, D.H., Groiss, H., Scharber, M.C., White, M.S., et al. (2015). Flexible high power-

per-weight perovskite solar cells with chromium oxide–metal contacts for improved stability in air. Nat. Mater. *14*, 1032–1039. https://doi.org/10.1038/nmat4388.

48. Kang, S., Jeong, J., Cho, S., Yoon, Y.J., Park, S., Lim, S., Kim, J.Y., and Ko, H. (2019). Ultrathin, lightweight and flexible perovskite solar cells with an excellent power-per-weight performance. J. Mater. Chem. A *7*, 1107–1114. https://doi.org/10.1039/C8TA10585E.

49. Song, W., Yu, K., Zhou, E., Xie, L., Hong, L., Ge, J., Zhang, J., Zhang, X., Peng, R., and Ge, Z. (2021). Crumple Durable Ultraflexible Organic Solar Cells with an Excellent Power-per-Weight Performance. Adv. Funct. Mater. *31*, 2102694. https://doi.org/10.1002/adfm.202102694.

50. Green, M.A., Dunlop, E.D., Yoshita, M., Kopidakis, N., Bothe, K., Siefer, G., Hinken, D., Rauer, M., Hohl-Ebinger, J., and Hao, X. (2024). Solar cell efficiency tables (Version 64). Prog. Photovolt. Res. Appl. *32*, 425–441. https://doi.org/10.1002/pip.3831.

51. Zhu, L., Zhang, M., Xu, J., Li, C., Yan, J., Zhou, G., Zhong, W., Hao, T., Song, J., Xue, X., et al. (2022). Single-junction organic solar cells with over 19% efficiency enabled by a refined double-fibril network morphology. Nat. Mater. *21*, 656–663. https://doi.org/10.1038/s41563-022-01244-y.

52. ECSS-E-ST-20-08C Rev.2 – Photovoltaic assemblies and components (20 April 2023) | European Cooperation for Space Standardization https://ecss.nl/standard/ecss-e-st-20-08c-rev-2-photovoltaic-assemblies-and-components-20-april-2023/.

53. Schneider, T.A., Vaughn, J.A., Wright, K.H., and Phillips, B.S. (2015). Space environment testing of photovoltaic array systems at NASA’s Marshall Space Flight Center. In 2015 IEEE 42nd Photovoltaic Specialist Conference (PVSC) (IEEE), pp. 1–6. https://doi.org/10.1109/PVSC.2015.7355861.

54. 24th Annual AIAA/USU Conference on Small Satellites: Connecting the Dots (2010). (AIAA).

55. Lu, Y., Shao, Q., Yue, H., and Yang, F. (2019). A Review of the Space Environment Effects on Spacecraft in Different Orbits. IEEE Access *7*, 93473–93488. https://doi.org/10.1109/ACCESS.2019.2927811.

56. Pisacane, V.L. (2016). The Space Environment and Its Effects on Space Systems, Second Edition (American Institute of Aeronautics and Astronautics, Inc.) https://doi.org/10.2514/4.103537.

57. Torkar, K., Nakamura, R., Tajmar, M., Scharlemann, C., Jeszenszky, H., Laky, G., Fremuth, G., Escoubet, C.P., and Svenes, K. (2016). Active Spacecraft Potential Control Investigation. Space Sci. Rev. *199*, 515–544. https://doi.org/10.1007/s11214-014-0049-3.

58. Jiggens, P., Heynderickx, D., Sandberg, I., Truscott, P., Raukunen, O., and Vainio, R. (2018). Updated Model of the Solar Energetic Proton Environment in Space. Preprint at

arXiv, https://doi.org/10.48550/arXiv.1801.05422
https://doi.org/10.48550/arXiv.1801.05422.

59. Bailey, S., and Raffaelle, R. (2012). Operation of Solar Cells in a Space Environment. In Practical Handbook of Photovoltaics (Elsevier), pp. 863–880. https://doi.org/10.1016/B978-0-12-385934-1.00027-1.

60. Tu, Y., Wu, J., Xu, G., Yang, X., Cai, R., Gong, Q., Zhu, R., and Huang, W. (2021). Perovskite Solar Cells for Space Applications: Progress and Challenges. Adv. Mater. *33*, 2006545. https://doi.org/10.1002/adma.202006545.

61. Yoon, G.W., Jo, B., Boonmongkolras, P., Han, G.S., and Jung, H.S. Perovskite Tandem Solar Cells for Low Earth Orbit Satellite Power Applications. Adv. Energy Mater. *n/a*, 2400204. https://doi.org/10.1002/aenm.202400204.

62. Köhler, A., and Bässler, H. Electronic Processes in Organic Semiconductors.

63. Sun, B. (2024). Energieverluste in organischen Solarzellen mit geringer VersetzungEnergy losses in low-offset organic solar cells: from fundamental understanding to characterization considerations: von grundlegendem Verständnis bis zu Charakterisierungsüberlegungen. 5947 KB, xxi, 190 pages. https://doi.org/10.25932/PUBLISHUP-62143.

64. Liu, D., Kan, B., Ke, X., Zheng, N., Xie, Z., Lu, D., and Liu, Y. (2018). Extended Conjugation Length of Nonfullerene Acceptors with Improved Planarity via Noncovalent Interactions for High-Performance Organic Solar Cells. Adv. Energy Mater. *8*, 1801618. https://doi.org/10.1002/aenm.201801618.

65. Yuan, J., Zhang, Y., Zhou, L., Zhang, G., Yip, H.-L., Lau, T.-K., Lu, X., Zhu, C., Peng, H., Johnson, P.A., et al. (2019). Single-Junction Organic Solar Cell with over 15% Efficiency Using Fused-Ring Acceptor with Electron-Deficient Core. Joule *3*, 1140–1151. https://doi.org/10.1016/j.joule.2019.01.004.

66. Guo, Q., Guo, Q., Geng, Y., Tang, A., Zhang, M., Du, M., Sun, X., and Zhou, E. (2021). Recent advances in PM6:Y6-based organic solar cells. Mater. Chem. Front. *5*, 3257–3280. https://doi.org/10.1039/D1QM00060H.

67. Hughes, M.P., Rosenthal, K.D., Ran, N.A., Seifrid, M., Bazan, G.C., and Nguyen, T.-Q. (2018). Determining the Dielectric Constants of Organic Photovoltaic Materials Using Impedance Spectroscopy. Adv. Funct. Mater. *28*, 1801542. https://doi.org/10.1002/adfm.201801542.

68. Torabi, S., Jahani, F., Van Severen, I., Kanimozhi, C., Patil, S., Havenith, R.W.A., Chiechi, R.C., Lutsen, L., Vanderzande, D.J.M., Cleij, T.J., et al. (2015). Strategy for Enhancing the Dielectric Constant of Organic Semiconductors Without Sacrificing Charge Carrier Mobility and Solubility. Adv. Funct. Mater. *25*, 150–157. https://doi.org/10.1002/adfm.201402244.

69. Zhang, L., Deng, D., Lu, K., and Wei, Z. (2024). Optimization of Charge Management and Energy Loss in All-Small-Molecule Organic Solar Cells. Adv. Mater. *36*, 2302915. https://doi.org/10.1002/adma.202302915.

70. Schopp, N. (2023). Understanding the Limitations of Organic Photovoltaics. https://doi.org/10.13140/RG.2.2.17015.50089.

71. Dahiya, H., Suthar, R., Khandelwal, K., Karak, S., and Sharma, G.D. (2022). Recent Advances in Organic and Inorganic Hole and Electron Transport Layers for Organic Solar Cells: Basic Concept and Device Performance. ACS Appl. Electron. Mater. *4*, 5119–5143. https://doi.org/10.1021/acsaelm.2c01076.

72. Bi, P., Zhang, S., Wang, J., Ren, J., and Hou, J. (2021). Progress in Organic Solar Cells: Materials, Physics and Device Engineering. Chin. J. Chem. *39*, 2607–2625. https://doi.org/10.1002/cjoc.202000666.

73. Blom, P.W.M., Mihailetchi, V.D., Koster, L.J.A., and Markov, D.E. (2007). Device Physics of Polymer:Fullerene Bulk Heterojunction Solar Cells. Adv. Mater. *19*, 1551–1566. https://doi.org/10.1002/adma.200601093.

74. Karagiannidis, P.G., Kalfagiannis, N., Georgiou, D., Laskarakis, A., Hastas, N.A., Pitsalidis, C., and Logothetidis, S. (2012). Effects of buffer layer properties and annealing process on bulk heterojunction morphology and organic solar cell performance. J. Mater. Chem. *22*, 14624. https://doi.org/10.1039/c2jm31277h.

75. Xu, H., Yuan, F., Zhou, D., Liao, X., Chen, L., and Chen, Y. (2020). Hole transport layers for organic solar cells: recent progress and prospects. J. Mater. Chem. A *8*, 11478–11492. https://doi.org/10.1039/D0TA03511D.

76. Kim, D.H., Wibowo, F.T.A., Lee, D., Krishna, N.V., Park, S., Cho, S., and Jang, S.-Y. (2023). Non-Fullerene-Based Inverted Organic Photovoltaic Device with Long-Term Stability. ENERGY Environ. Mater. *6*, e12381. https://doi.org/10.1002/eem2.12381.

77. Hosseini, S.M., Tokmoldin, N., Lee, Y.W., Zou, Y., Woo, H.Y., Neher, D., and Shoaee, S. (2020). Putting Order into PM6:Y6 Solar Cells to Reduce the Langevin Recombination in 400 nm Thick Junction. Sol. RRL *4*, 2000498. https://doi.org/10.1002/solr.202000498.

78. Brandon, D., and Kaplan, W.D. Microstructural Characterization of Materials.

79. AFM Principle - How Does an Atomic Force Microscope Work? https://afm.oxinst.com/outreach/how-does-an-afm-microscope-work.

80. Stevie, F.A., and Donley, C.L. (2020). Introduction to x-ray photoelectron spectroscopy. J. Vac. Sci. Technol. A *38*, 063204. https://doi.org/10.1116/6.0000412.

81. UV-Vis Spectroscopy: Principle, Strengths and Limitations and Applications | Technology Networks https://www.technologynetworks.com/analysis/articles/uv-vis-spectroscopy-principle-strengths-and-limitations-and-applications-349865.

82. Ukhanov, Iu.I. (1977). Optical properties of semiconductors. Mosc. Izd. Nauka.

83. Wee, A.T.S., Yin, X., and Tang, C.S. (2022). Introduction to spectroscopic ellipsometry of thin film materials: instrumentation, data analysis, and applications (Wiley-VCH).

84. Making van der Pauw Resistivity and Hall Voltage Measurements Using the 4200A-SCS Parameter Analyzer.

85. Proctor, C.M., Kuik, M., and Nguyen, T.-Q. (2013). Charge carrier recombination in organic solar cells. Prog. Polym. Sci. *38*, 1941–1960. https://doi.org/10.1016/j.progpolymsci.2013.08.008.

86. Schopp, N., Luong, H.M., Luginbuhl, B.R., Panoy, P., Choi, D., Promarak, V., Brus, V.V., and Nguyen, T.-Q. (2022). Understanding Interfacial Recombination Processes in Narrow-Band-Gap Organic Solar Cells. ACS Energy Lett. *7*, 1626–1634. https://doi.org/10.1021/acsenergylett.2c00502.

87. Fu, J., Yang, Q., Huang, P., Chung, S., Cho, K., Kan, Z., Liu, H., Lu, X., Lang, Y., Lai, H., et al. (2024). Rational molecular and device design enables organic solar cells approaching 20% efficiency. Nat. Commun. *15*, 1830. https://doi.org/10.1038/s41467-024-46022-3.

88. Zhang, Y., Deng, W., Petoukhoff, C.E., Xia, X., Lang, Y., Xia, H., Tang, H., Chandran, H.T., Mahadevan, S., Liu, K., et al. (2024). Achieving 19.4% organic solar cell via an in situ formation of p-i-n structure with built-in interpenetrating network. Joule *8*, 509–526. https://doi.org/10.1016/j.joule.2023.12.009.

89. Liu, H., Geng, Y., Xiao, Z., Ding, L., Du, J., Tang, A., and Zhou, E. (2024). The Development of Quinoxaline-Based Electron Acceptors for High Performance Organic Solar Cells. Adv. Mater. *36*, 2404660. https://doi.org/10.1002/adma.202404660.

90. Sze, S.M., Li, Y., and Ng, K.K. (2021). Physics of semiconductor devices Fourth edition. (Wiley).

91. Benduhn, J., Tvingstedt, K., Piersimoni, F., Ullbrich, S., Fan, Y., Tropiano, M., McGarry, K.A., Zeika, O., Riede, M.K., Douglas, C.J., et al. (2017). Intrinsic non-radiative voltage losses in fullerene-based organic solar cells. Nat. Energy *2*, 17053. https://doi.org/10.1038/nenergy.2017.53.

92. Shockley, W., and Read, W.T. (1952). Statistics of the Recombinations of Holes and Electrons. Phys. Rev. *87*, 835–842. https://doi.org/10.1103/PhysRev.87.835.

93. Vollbrecht, J., Brus, V.V., Ko, S., Lee, J., Karki, A., Cao, D.X., Cho, K., Bazan, G.C., and Nguyen, T. (2019). Quantifying the Nongeminate Recombination Dynamics in Nonfullerene Bulk Heterojunction Organic Solar Cells. Adv. Energy Mater. *9*, 1901438. https://doi.org/10.1002/aenm.201901438.

94. Vollbrecht, J., Tokmoldin, N., Sun, B., Saglamkaya, E., Perdigón-Toro, L., Hosseini, S.M., Son, J.H., Woo, H.Y., Shoaee, S., and Neher, D. (2023). On the relationship of the effective

mobility and photoconductance mobility in organic solar cells. Energy Adv. *2*, 1390–1398. https://doi.org/10.1039/D3YA00125C.

95. Brus, V.V., Proctor, C.M., Ran, N.A., and Nguyen, T.-Q. (2016). Capacitance Spectroscopy for Quantifying Recombination Losses in Nonfullerene Small-Molecule Bulk Heterojunction Solar Cells. Adv. Energy Mater. *6*, 1502250. https://doi.org/10.1002/aenm.201502250.

96. Brus, V.V., Schopp, N., Ko, S.-J., Vollbrecht, J., Lee, J., Karki, A., Bazan, G.C., and Nguyen, T.-Q. (2021). Temperature and Light Modulated Open-Circuit Voltage in Nonfullerene Organic Solar Cells with Different Effective Bandgaps. Adv. Energy Mater. *11*, 2003091. https://doi.org/10.1002/aenm.202003091.

97. Karki, A., Vollbrecht, J., Dixon, A.L., Schopp, N., Schrock, M., Reddy, G.N.M., and Nguyen, T. (2019). Understanding the High Performance of over 15% Efficiency in Single-Junction Bulk Heterojunction Organic Solar Cells. Adv. Mater. *31*, 1903868. https://doi.org/10.1002/adma.201903868.

98. Karki, A., Vollbrecht, J., Gillett, A.J., Xiao, S.S., Yang, Y., Peng, Z., Schopp, N., Dixon, A.L., Yoon, S., Schrock, M., et al. (2020). The role of bulk and interfacial morphology in charge generation, recombination, and extraction in non-fullerene acceptor organic solar cells. Energy Environ. Sci. *13*, 3679–3692. https://doi.org/10.1039/D0EE01896A.

99. Zeng, Y., Li, D., Wu, H., Chen, Z., Leng, S., Hao, T., Xiong, S., Xue, Q., Ma, Z., Zhu, H., et al. (2022). Enhanced Charge Transport and Broad Absorption Enabling Record 18.13% Efficiency of PM6:Y6 Based Ternary Organic Photovoltaics with a High Fill Factor Over 80%. Adv. Funct. Mater. *32*, 2110743. https://doi.org/10.1002/adfm.202110743.

100. Chen, J., Cao, J., Liu, L., Xie, L., Zhou, H., Zhang, J., Zhang, K., Xiao, M., and Huang, F. (2022). Layer-by-Layer Processed PM6:Y6-Based Stable Ternary Polymer Solar Cells with Improved Efficiency over 18% by Incorporating an Asymmetric Thieno[3,2- *b*]indole-Based Acceptor. Adv. Funct. Mater. *32*, 2200629. https://doi.org/10.1002/adfm.202200629.

101. Sievers, D.W., Shrotriya, V., and Yang, Y. (2006). Modeling optical effects and thickness dependent current in polymer bulk-heterojunction solar cells. J. Appl. Phys. *100*, 114509. https://doi.org/10.1063/1.2388854.

102. Pettersson, L.A.A., Roman, L.S., and Inganäs, O. (1999). Modeling photocurrent action spectra of photovoltaic devices based on organic thin films. J. Appl. Phys. *86*, 487–496. https://doi.org/10.1063/1.370757.

103. Schopp, N., Brus, V.V., Lee, J., Bazan, G.C., and Nguyen, T. (2021). A Simple Approach for Unraveling Optoelectronic Processes in Organic Solar Cells under Short-Circuit Conditions. Adv. Energy Mater. *11*, 2002760. https://doi.org/10.1002/aenm.202002760.

104. Yakubovsky, D.I., Arsenin, A.V., Stebunov, Y.V., Fedyanin, D.Yu., and Volkov, V.S. (2017). Optical constants and structural properties of thin gold films. Opt. Express *25*, 25574. https://doi.org/10.1364/OE.25.025574.

105. Zhang, X., Qiu, J., Li, X., Zhao, J., and Liu, L. (2020). Complex refractive indices measurements of polymers in visible and near-infrared bands. Appl. Opt. *59*, 2337. https://doi.org/10.1364/AO.383831.

106. Li, Y., Wang, J., Yan, C., Zhang, S., Cui, N., Liu, Y., Li, G., and Cheng, P. (2024). Optical and electrical losses in semitransparent organic photovoltaics. Joule *8*, 527–541. https://doi.org/10.1016/j.joule.2023.12.011.

107. Scheunemann, D., Wilken, S., Sandberg, O.J., Österbacka, R., and Schiek, M. (2019). Effect of Imbalanced Charge Transport on the Interplay of Surface and Bulk Recombination in Organic Solar Cells. Phys. Rev. Appl. *11*, 054090. https://doi.org/10.1103/PhysRevApplied.11.054090.

108. Kirchartz, T., Deledalle, F., Tuladhar, P.S., Durrant, J.R., and Nelson, J. (2013). On the Differences between Dark and Light Ideality Factor in Polymer:Fullerene Solar Cells. J. Phys. Chem. Lett. *4*, 2371–2376. https://doi.org/10.1021/jz4012146.

109. Wheeler, S., Deledalle, F., Tokmoldin, N., Kirchartz, T., Nelson, J., and Durrant, J.R. (2015). Influence of Surface Recombination on Charge-Carrier Kinetics in Organic Bulk Heterojunction Solar Cells with Nickel Oxide Interlayers. Phys. Rev. Appl. *4*, 024020. https://doi.org/10.1103/PhysRevApplied.4.024020.

110. Solak, S., Ricciardulli, A.G., Lenz, T., Crăciun, N.I., Blom, P.W.M., and Wetzelaer, G.A.H. (2017). Open-circuit voltage loss in annealed P3HT:perylene diimide bulk heterojunction solar cells. Appl. Phys. Lett. *110*, 163301. https://doi.org/10.1063/1.4980842.

111. Zhang, X., Yao, N., Wang, R., Li, Y., Zhang, D., Wu, G., Zhou, J., Li, X., Zhang, H., Zhang, J., et al. (2020). On the understanding of energy loss and device fill factor trade-offs in non-fullerene organic solar cells with varied energy levels. Nano Energy *75*, 105032. https://doi.org/10.1016/j.nanoen.2020.105032.

112. Mihailetchi, V.D., Blom, P.W.M., Hummelen, J.C., and Rispens, M.T. (2003). Cathode dependence of the open-circuit voltage of polymer:fullerene bulk heterojunction solar cells. J. Appl. Phys. *94*, 6849–6854. https://doi.org/10.1063/1.1620683.

113. Von Hauff, E. (2019). Impedance Spectroscopy for Emerging Photovoltaics. J. Phys. Chem. C *123*, 11329–11346. https://doi.org/10.1021/acs.jpcc.9b00892.

114. Schopp, N., Brus, V.V., Lee, J., Dixon, A., Karki, A., Liu, T., Peng, Z., Graham, K.R., Ade, H., Bazan, G.C., et al. (2021). Effect of Palladium-Tetrakis(Triphenylphosphine) Catalyst Traces on Charge Recombination and Extraction in Non-Fullerene-based Organic Solar Cells. Adv. Funct. Mater. *31*, 2009363. https://doi.org/10.1002/adfm.202009363.

115. Vollbrecht, J., Tokmoldin, N., Sun, B., Brus, V.V., Shoaee, S., and Neher, D. (2022). Determination of the charge carrier density in organic solar cells: A tutorial. J. Appl. Phys. *131*, 221101. https://doi.org/10.1063/5.0094955.

116. Kaikanov, M., Nauruzbayev, D., Abduvalov, A., and Baigarin, K. (2023). Investigation of intense pulsed ion beam generation by a magnetically insulated ion diode at a reduced impedance. Vacuum *217*, 112496. https://doi.org/10.1016/j.vacuum.2023.112496.

117. Ziegler SRIM & TRIM. http://www.srim.org/.

118. Lee, H.K.H., Stewart, K., Hughes, D., Barbé, J., Pockett, A., Kilbride, R.C., Heasman, K.C., Wei, Z., Watson, T.M., Carnie, M.J., et al. (2022). Proton Radiation Hardness of Organic Photovoltaics: An In-Depth Study. Sol. RRL *6*, 2101037. https://doi.org/10.1002/solr.202101037.

119. Street, R.A., Northrup, J.E., and Krusor, B.S. (2012). Radiation induced recombination centers in organic solar cells. Phys. Rev. B *85*, 205211. https://doi.org/10.1103/PhysRevB.85.205211.

120. Parkhomenko, H.P., Mostovyi, A.I., Akhtanova, G., Solovan, M.M., Kaikanov, M., Schopp, N., and Brus, V.V. (2023). Self-Healing of Proton-Irradiated Organic Photodiodes and Photovoltaics (Adv. Energy Mater. 37/2023). Adv. Energy Mater. *13*, 2370151. https://doi.org/10.1002/aenm.202370151.

121. Shen, Z., Jiang, Y., Yu, J., Zhu, Y., Bu, L., and Lu, G. (2021). Film-Depth-Dependent Light Reflection Spectroscopy for Photovoltaics and Transistors. Adv. Mater. Interfaces *8*, 2101476. https://doi.org/10.1002/admi.202101476.

122. Li, Y., Kamaraj, K., Silori, Y., Zhao, H., Arneson, C., Liu, B., Ogilvie, J., and Forrest, S.R. (2025). Radiation hardness of organic photovoltaics. Joule, 101800. https://doi.org/10.1016/j.joule.2024.12.001.

123. Michler, G.H. (2008). Electron Microscopy of Polymers (Springer Berlin / Heidelberg).

124. Burkhard, G.F., Hoke, E.T., and Group, M. Transfer Matrix Optical Modeling.

125. Hecht, K. (1932). Zum Mechanismus des lichtelektrischen Prim�rstromes in isolierenden Kristallen. Z. F�r Phys. *77*, 235–245. https://doi.org/10.1007/BF01338917.

126. Lang, F., Shargaieva, O., Brus, V.V., Rappich, J., and Nickel, N.H. (2018). Creation and annealing of metastable defect states in CH3NH3PbI3 at low temperatures. Appl. Phys. Lett. *112*, 081102. https://doi.org/10.1063/1.5019921.

127. Kim, D.Y., Subbiah, J., Sarasqueta, G., So, F., Ding, H., Irfan, and Gao, Y. (2009). The effect of molybdenum oxide interlayer on organic photovoltaic cells. Appl. Phys. Lett. *95*, 093304. https://doi.org/10.1063/1.3220064.

128. Manders, J.R., Tsang, S., Hartel, M.J., Lai, T., Chen, S., Amb, C.M., Reynolds, J.R., and So, F. (2013). Solution-Processed Nickel Oxide Hole Transport Layers in High Efficiency Polymer Photovoltaic Cells. Adv. Funct. Mater. *23*, 2993–3001. https://doi.org/10.1002/adfm.201202269.

129. Reese, M.O., White, M.S., Rumbles, G., Ginley, D.S., and Shaheen, S.E. (2008). Optimal negative electrodes for poly(3-hexylthiophene): [6,6]-phenyl C61-butyric acid methyl ester bulk heterojunction photovoltaic devices. Appl. Phys. Lett. *92*, 053307. https://doi.org/10.1063/1.2841067.

130. van Reenen, S., Kouijzer, S., Janssen, R.A.J., Wienk, M.M., and Kemerink, M. (2014). Origin of Work Function Modification by Ionic and Amine-Based Interface Layers. Adv. Mater. Interfaces *1*, 1400189. https://doi.org/10.1002/admi.201400189.

131. Yin, Z., Wei, J., and Zheng, Q. (2016). Interfacial Materials for Organic Solar Cells: Recent Advances and Perspectives. Adv. Sci. *3*, 1500362. https://doi.org/10.1002/advs.201500362.

132. Jørgensen, M., Norrman, K., and Krebs, F.C. (2008). Stability/degradation of polymer solar cells. Sol. Energy Mater. Sol. Cells *92*, 686–714. https://doi.org/10.1016/j.solmat.2008.01.005.

133. Yin, Z., and Zheng, Q. (2012). Controlled Synthesis and Energy Applications of One-Dimensional Conducting Polymer Nanostructures: An Overview. Adv. Energy Mater. *2*, 179–218. https://doi.org/10.1002/aenm.201100560.

134. Guo, L., Ji, Y.L., Xu, H., Simon, P., and Wu, Z. (2002). Regularly Shaped, Single-Crystalline ZnO Nanorods with Wurtzite Structure. J. Am. Chem. Soc. *124*, 14864–14865. https://doi.org/10.1021/ja027947g.

135. Gülnahar, M., Nasser, H., Salimi, A., and Turan, R. (2021). On the electrical and charge conduction properties of thermally evaporated MoOx on n- and p-type crystalline silicon. J. Mater. Sci. Mater. Electron. *32*, 1092–1104. https://doi.org/10.1007/s10854-020-04884-5.

136. Song, C., Huang, X., Zhan, T., Ding, L., Li, Y., Xue, X., Lin, X., Peng, H., Cai, P., Duan, C., et al. (2022). Annealing-Insensitive, Alcohol-Processed MoO_x Hole Transport Layer for Universally Enabling High-Performance Conventional and Inverted Organic Solar Cells. ACS Appl. Mater. Interfaces *14*, 40851–40861. https://doi.org/10.1021/acsami.2c09413.

137. Wei, J., Lei, Y., Jia, H., Cheng, J., Hou, H., and Zheng, Z. (2014). Controlled in situ fabrication of Ag_2O/AgO thin films by a dry chemical route at room temperature for hybrid solar cells. Dalton Trans *43*, 11333–11338. https://doi.org/10.1039/C4DT00827H.

138. Moon, Y.-K., Moon, D.-Y., Lee, S., and Park, J.-W. (2009). Effects of High-Dose Proton Irradiation on ZnO Thin-Film Transistors. J. Korean Phys. Soc. *54*, 1059–1063. https://doi.org/10.3938/jkps.54.1059.

139. Liu, N., Zhang, L., Liang, Y., Xue, B., and Wang, D. (2023). Effects of Carrier Transport Layers on Performance Degradation in Perovskite Solar Cells under Proton Irradiation. ACS Appl. Energy Mater. *6*, 6673–6680. https://doi.org/10.1021/acsaem.3c00727.

140. Baker, D.N., Erickson, P.J., Fennell, J.F., Foster, J.C., Jaynes, A.N., and Verronen, P.T. (2017). Space Weather Effects in the Earth’s Radiation Belts. Space Sci. Rev. *214*, 17. https://doi.org/10.1007/s11214-017-0452-7.

141. Yang, Y., Zhu, H., Wang, L., Jiang, Y., Wang, T., Liu, C., Li, B., Tang, W., Wu, Z., Yang, Z., et al. (2022). In-depth investigation of low-energy proton irradiation effect on the structural and photoresponse properties of ε-Ga2O3 thin films. Mater. Des. *221*, 110944. https://doi.org/10.1016/j.matdes.2022.110944.

142. Gohl, S., Bergmann, B., and Pospisil, S. (2018). Design Study of a New Miniaturized Radiation Monitor Based on Previous Experience with the Space Application of the Timepix Radiation Monitor (SATRAM). In 2018 IEEE Nuclear Science Symposium and Medical Imaging Conference Proceedings (NSS/MIC), pp. 1–7. https://doi.org/10.1109/NSSMIC.2018.8824453.

143. Troska, J., Vasey, F., and Weidberg, A. (2023). Radiation tolerant optoelectronics for high energy physics. Nucl. Instrum. Methods Phys. Res. Sect. Accel. Spectrometers Detect. Assoc. Equip. *1052*, 168208. https://doi.org/10.1016/j.nima.2023.168208.

144. Hands, A.D.P., Ryden, K.A., Meredith, N.P., Glauert, S.A., and Horne, R.B. (2018). Radiation Effects on Satellites During Extreme Space Weather Events. Space Weather *16*, 1216–1226. https://doi.org/10.1029/2018SW001913.

145. Hastings, D., and Garrett, H. (1996). Spacecraft-Environment Interactions (Cambridge University Press).

146. Solovan, M.M., Mostovyi, A.I., Parkhomenko, H.P., Kaikanov, M., Schopp, N., Asare, E.A., Kovaliuk, T., Veřtát, P., Ulyanytsky, K.S., Korbutyak, D.V., et al. (2023). A High-Detectivity, Fast-Response, and Radiation-Resistant TiN/CdZnTe Heterojunction Photodiode. Adv. Opt. Mater. *11*, 2202028. https://doi.org/10.1002/adom.202202028.

147. Sittimart, P., Ohmagari, S., Umezawa, H., Kato, H., Ishiji, K., and Yoshitake, T. (2023). Thermally Stable and Radiation-Proof Visible-Light Photodetectors Made from N-Doped Diamond. Adv. Opt. Mater. *11*, 2203006. https://doi.org/10.1002/adom.202203006.

148. Konusov, F., Pavlov, S., Lauk, A., Kabyshev, A., Novikov, V., Gadirov, R., Tarbokov, V., and Remnev, G. (2022). Effect of short-pulsed ion irradiation on the optical and electrical properties of titanium nitride films deposited by reactive magnetron sputtering. Nucl. Instrum. Methods Phys. Res. Sect. B Beam Interact. Mater. At. *526*, 51–59. https://doi.org/10.1016/j.nimb.2022.06.011.

149. Xue, J.-X., Zhang, G.-J., Guo, L.-P., Zhang, H.-B., Wang, X.-G., Zou, J., Peng, S.-M., and Long, X.-G. (2014). Improved radiation damage tolerance of titanium nitride ceramics by introduction of vacancy defects. J. Eur. Ceram. Soc. *34*, 633–639. https://doi.org/10.1016/j.jeurceramsoc.2013.10.012.

150. Qualification and Quality Requirements for Space Solar Panels ed. (2014). Standard: Qualification and Quality Requirements for Space Solar Cells (AIAA S-111A-2014). In

Standard: Qualification and Quality Requirements for Space Solar Cells (AIAA S-111A-2014) (American Institute of Aeronautics and Astronautics, Inc.). https://doi.org/10.2514/4.102806.001.

151. Liu, C.-C., Wang, W.-T., Houng, M.-P., Wang, Y.-H., and Chen, S.-M. (2002). Titanium nitride as spreading layers for AlGaInP visible LEDs. IEEE Photonics Technol. Lett. *14*, 1665–1667. https://doi.org/10.1109/LPT.2002.804669.

152. Fani, N., and Savaloni, H. (2012). *Investigation on the formation of titanium nitride thin films on 304 type stainless steel using plasma focus device. J. Theor. Appl. Phys. *6*, 30. https://doi.org/10.1186/2251-7235-6-30.

153. Komarov, F.F., Konstantinov, S.V., Strel'nitskij, V.E., and Pilko, V.V. (2016). Effect of Helium ion irradiation on the structure, the phase stability, and the microhardness of TiN, TiAlN, and TiAlYN nanostructured coatings. Tech. Phys. *61*, 696–702. https://doi.org/10.1134/S106378421605011X.

154. Yu, J., Phang, P., Samundsett, C., Basnet, R., Neupan, G.P., Yang, X., Macdonald, D.H., Wan, Y., Yan, D., and Ye, J. (2020). Titanium Nitride Electron-Conductive Contact for Silicon Solar Cells By Radio Frequency Sputtering from a TiN Target. ACS Appl. Mater. Interfaces *12*, 26177–26183. https://doi.org/10.1021/acsami.0c04439.

155. Roy, M., Sarkar, K., Som, J., Pfeifer, M.A., Craciun, V., Schall, J.D., Aravamudhan, S., Wise, F.W., and Kumar, D. (2023). Modulation of Structural, Electronic, and Optical Properties of Titanium Nitride Thin Films by Regulated In Situ Oxidation. ACS Appl. Mater. Interfaces *15*, 4733–4742. https://doi.org/10.1021/acsami.2c18926.

156. Grayeli Korpi, A., Ţălu, Ş., Bramowicz, M., Arman, A., Kulesza, S., Pszczolkowski, B., Jurečka, S., Mardani, M., Luna, C., Balashabadi, P., et al. (2019). Minkowski functional characterization and fractal analysis of surfaces of titanium nitride films. Mater. Res. Express *6*, 086463. https://doi.org/10.1088/2053-1591/ab26be.

157. Khezripour, Z., Mahani, F.F., and Mokhtari, A. (2018). Performance improvement of ultrathin organic solar cells utilizing light-trapping aluminum-titanium nitride nanosquare arrays. Opt. Mater. *84*, 651–657. https://doi.org/10.1016/j.optmat.2018.07.073.

158. Yang, X., Liu, W., De Bastiani, M., Allen, T., Kang, J., Xu, H., Aydin, E., Xu, L., Bi, Q., Dang, H., et al. (2019). Dual-Function Electron-Conductive, Hole-Blocking Titanium Nitride Contacts for Efficient Silicon Solar Cells. Joule *3*, 1314–1327. https://doi.org/10.1016/j.joule.2019.03.008.

159. Dong, Z., Zhao, C., Shen, J., and Huang, Y. (2020). Direct Evidence of the Dynamic Growth of Nanotwinned Copper Grain upon Electron Beam Irradiation. Cryst. Growth Des. *20*, 6493–6501. https://doi.org/10.1021/acs.cgd.0c00651.

160. Zhang, R., Ma, Q.-Y., Liu, H., Sun, T.-Y., Bi, J., Song, Y., Peng, S., Liang, L., Gao, J., Cao, H., et al. (2021). Crystal Orientation-Dependent Oxidation of Epitaxial TiN Films

with Tunable Plasmonics. ACS Photonics *8*, 847–856. https://doi.org/10.1021/acsphotonics.0c01827.

161. Jiang, N., Zhang, H.J., Bao, S.N., Shen, Y.G., and Zhou, Z.F. (2004). XPS study for reactively sputtered titanium nitride thin films deposited under different substrate bias. Phys. B Condens. Matter *352*, 118–126. https://doi.org/10.1016/j.physb.2004.07.001.

162. Patsalas, P., Kalfagiannis, N., and Kassavetis, S. (2015). Optical Properties and Plasmonic Performance of Titanium Nitride. Materials *8*, 3128–3154. https://doi.org/10.3390/ma8063128.